

WTIS HC \$10.00

THE TURBULENT BOUNDARY LAYER ON A POROUS PLATE: AN EXPERIMENTAL STUDY OF THE HEAT TRANSFER BEHAVIOR WITH ADVERSE PRESSURE GRADIENTS

By

B. F. Blackwell, W. M. Kays and R. J. Moffat

Report No. HMT-16

Prepared Under Grant NASA NgL-05-020-134

for

The National Aeronautics and Space Administration



Reproduced by
**NATIONAL TECHNICAL
INFORMATION SERVICE**
US Department of Commerce
Springfield, VA. 22151

**Thermosciences Division
Department of Mechanical Engineering
Stanford University
Stanford, California**

August 1972

(NASA-CR-130291) THE TURBULENT BOUNDARY
LAYER ON A POROUS PLATE: AN
EXPERIMENTAL STUDY OF THE HEAT TRANSFER
BEHAVIOR WITH ADVERSE PRESSURE (Stanford
Univ.) 158 p HC \$10.00

N73-15291

CSCL 20D

G3/12

Unclas
16857

1580

THE TURBULENT BOUNDARY LAYER ON A POROUS PLATE:
AN EXPERIMENTAL STUDY OF THE HEAT TRANSFER BEHAVIOR
WITH ADVERSE PRESSURE GRADIENTS

By

B. F. Blackwell, W. M. Kays and R. J. Moffat

Report No. HMT-16

Prepared Under Grant NASA NgL-05-020-134

for

The National Aeronautics and Space Administration

Thermosciences Division
Department of Mechanical Engineering
Stanford University
Stanford, California

August 1972

Details of illustrations in
this document may be better
studied on microfiche.

PRECEDING PAGE BLANK NOT FILMED

ACKNOWLEDGMENTS

This research was made possible by a grant from the National Aeronautics and Space Administration, NgL 05-020-134. The authors wish to express appreciation for the interest of Dr. Robert W. Graham of the NASA Lewis Laboratories. Additionally, Mr. Blackwell was supported by the United States Atomic Energy Commission.

The authors also wish to thank Mr. Robin Birch for his meticulous craftsmanship in the construction of the temperature probes and wind tunnel, Mr. Alcir Orlando for his assistance in the data taking, Mr. Mike Crawford who assisted with the numerical predictions, and last but not least Ms. Jan Elliott and Mrs. Ruth Korb for their excellent typing.

Preceding page blank

ABSTRACT

An experimental investigation of the heat transfer behavior of the near equilibrium transpired turbulent boundary layer with adverse pressure gradient has been carried out. Stanton numbers were measured by an energy balance on electrically heated plates that form the bottom wall of the wind tunnel. Mean temperature profiles were measured by a 0.003 inch diameter Chromel/constantan thermocouple probe.

Two adverse pressure gradients of the form $u_\infty \sim x^m$ ($m < 0$) were studied. Two types of transpiration boundary conditions were investigated: (1) constant $F = \dot{m}''/\rho_\infty u_\infty$ and (2) constant $B_h = F/St$. The concept of an equilibrium thermal boundary layer was introduced. It was found that Stanton number as a function of enthalpy thickness Reynolds number is essentially unaffected by adverse pressure gradient with no transpiration.

Shear stress, heat flux, and turbulent Prandtl number profiles were computed from mean temperature and velocity profiles. It was concluded that the turbulent Prandtl number is greater than unity in near the wall and decreases continuously to approximately 0.5 at the free stream. In the log-region, the turbulent Prandtl number was found to be a function primarily of the pressure gradient; transpiration has relatively little influence. Increasing the adverse pressure gradient decreases the turbulent Prandtl number in the log-region.

Prediction of selected experimental runs was accomplished by a finite difference computer program. The turbulent Prandtl number model for the inner region was

$$Pr_t = C_1 \frac{\phi}{1 - e^{-\phi}}, \quad \phi = \frac{C_2}{\frac{\epsilon_m}{\nu} Pr}$$

while the outer region model was

$$Pr_t = 0.5 + b_1 [1 - (y/\delta)^2]$$

Mean velocity field closure was accomplished by van Driest's mixing length model.

TABLE OF CONTENTS

	Page
Acknowledgments	iii
Abstract	iv
Table of Contents	v
List of Figures	vii
List of Tables	xi
Nomenclature	xii
CHAPTER 1. INTRODUCTION	1
CHAPTER 2. BOUNDARY CONDITIONS: SURFACE TEMPERATURE, FREE STREAM VELOCITY AND TRANSPIRATION RATE	3
2.1 Velocity Defect Similarity	4
2.2 Temperature (Enthalpy) Defect Similarity	4
2.3 Surface Temperature Variation	6
2.4 Free Stream Velocity Variation	6
2.5 Transpiration Rate for Equilibrium Flows	6
2.6 Actual u_∞ and F Variation	10
2.7 Identification of Boundary Conditions	11
CHAPTER 3. EXPERIMENTAL APPARATUS, INSTRUMENTATION AND QUALIFICA- TION TESTS	12
3.1 Main Air Flow	12
3.2 Test Section	13
3.3 Transpiration Air System	15
3.4 Pressure Measurements	16
3.5 Velocity Measurements	16
3.6 Skin Friction	17
3.7 Mean Temperature Profile Measurements	17
3.8 Stanton Number	18
3.9 Qualification of the Apparatus	19
3.9.1 Transpiration Energy Balances	20
3.9.2 Inlet Velocity and Temperature Uniformity	21
3.9.3 Boundary Layer Energy Balances	21
3.9.4 Zero Pressure Gradient, Zero Transpiration Flow	23

	Page
CHAPTER 4. PRESENTATION OF EXPERIMENTAL STANTON NUMBER DATA	35
4.1 Stanton Numbers for No Transpiration Flows	35
4.2 Constant F Flows, $m = -0.15$	36
4.3 Constant B_h Flows, $m = -0.15$, $m_F = -0.17$	36
4.4 Comparison of Adverse Pressure Gradient Stanton Numbers With Zero Pressure Gradient Data	37
4.5 Asymptotic Suction Layer for $u_\infty \sim x^m$ Flows	38
CHAPTER 5. MEAN TEMPERATURE PROFILE DATA	45
5.1 Mean Temperature Profiles in Wall Coordinates	45
5.2 Mean Temperature Profiles in Outer Region Coordinates	47
5.3 Enthalpy Defect Profile Shape Factors	48
5.4 Reynolds Number Ratio.	48
CHAPTER 6. HEAT FLUX AND TURBULENT PRANDTL NUMBER PROFILES	57
6.1 Previous Experimental Turbulent Prandtl Number Studies	57
6.2 Computation of Heat Flux Profiles	58
6.3 Turbulent Prandtl Number Profiles	62
CHAPTER 7. A TURBULENT PRANDTL NUMBER MODEL AND PREDICTION OF SELECTED RUNS	73
7.1 Turbulent Prandtl Number Model for Inner Region	73
7.2 Turbulent Prandtl Number Model for Outer Region	77
7.3 Comparison of Predicted Stanton Numbers With Experi- mental Data	78
7.4 Comparison of Predicted Temperature Profiles With Experimental Data	80
7.5 Some Comments on a Heat Transfer Mixing Length Model	80
CHAPTER 8. SUMMARY	89
CHAPTER 9. TABULATION OF EXPERIMENTAL DATA	92
9.1 Experimental Stanton Number Tabulation	93
9.2 Mean Temperature Profile Tabulation	100
REFERENCES	135
APPENDIX A. ANALYSIS OF TEMPERATURE DISTRIBUTION IN BOUNDARY LAYER TEMPERATURE PROBE	138

LIST OF FIGURES

Figure		Page
3-1	Schematic of test apparatus	26
3-2	Photograph of test section with traversing mechanism in position	27
3-3	Spacing of plate thermocouples	27
3-4	Longitudinal cross section of tunnel test section	28
3-5	Cross section view of typical compartment	28
3-6	Photograph of traversing mechanism and temperature probe	29
3-7	Transpiration energy balances for blowing mode	30
3-8	Transpiration energy balances for suction mode	31
3-9	Transverse velocity profiles, $z > 0$, $x = 10$ inches	32
3-10	Transverse velocity profiles, $z < 0$, $x = 10$ inches	32
3-11	Transverse temperature profiles, $z > 0$, $x = 10$ inches	33
3-12	Transverse temperature profiles, $z < 0$, $x = 10$ inches	33
3-13	Zero pressure gradient, zero transpiration Stanton number data	34
4-1	Influence of pressure gradient with zero transpiration on Stanton number	39
4-2	Stanton number data for $m = -0.15$ and constant F boundary conditions	40
4-3	Stanton number data for $m = -0.15$ and constant B_h boundary conditions	41
4-4	Summary of all Stanton number data for $m = -0.15$	42
4-5	Stanton number ratio for all $m = -0.15$ flows	43
4-6	Comparison of selected adverse pressure gradient runs with zero pressure gradient data of Moffat [2]	44
5-1	Influence of pressure gradient on non-dimensional temperature profiles, wall coordinates	50

Figure		Page
5-2	Influence of pressure gradient on non-dimensional temperature profiles, wall coordinates	50
5-3	Influence of transpiration on non-dimensional temperature profiles, wall coordinates	51
5-4	Defect enthalpy profiles, run 091871	51
5-5	Defect enthalpy profiles, run 120471	52
5-6	Defect enthalpy profiles, run 110871	52
5-7	Defect enthalpy profiles, run 111871	53
5-8	Defect enthalpy profiles, run 011772	53
5-9	Influence of pressure gradient on defect enthalpy shape factor	54
5-10	Influence of transpiration on defect enthalpy shape factor	54
5-11	Influence of pressure gradient on Reynolds number ratio, $F = 0$	55
5-12	Influence of transpiration on Reynolds number ratio, $B_h =$ constant	55
5-13	Influence of transpiration on Reynolds number ratio, $F =$ constant	56
6-1	Influence of pressure gradient on heat flux profiles, $F = 0$	65
6-2	Influence of pressure gradient on shear stress profiles, $F = 0$	65
6-3	Influence of transpiration on heat flux profiles, $m = -0.15$	66
6-4	Validity of Couette flow assumption for computing heat flux profiles	67
6-5	Influence of pressure gradient on turbulent Prandtl number profiles, $x = 70$ inches	67
6-6	Influence of blowing on turbulent Prandtl number profiles, $x = 70$ inches	68
6-7	Influence of blowing on turbulent Prandtl number profiles, $x = 70$ inches	68

Figure		Page
6-8	Influence of suction on turbulent Prandtl number profiles, x = 70 inches	69
6-9	Influence of suction on turbulent Prandtl number profiles, x = 70 inches	69
6-10	Variation of turbulent Prandtl number in log-region	70
6-11	Influence of pressure gradient on turbulent Prandtl number profiles, x = 70 inches	70
6-12	Influence of blowing on turbulent Prandtl number profiles, x = 70 inches	71
6-13	Influence of blowing on turbulent Prandtl number profiles, x = 70 inches	71
6-14	Influence of suction on turbulent Prandtl number profiles, x = 70 inches	72
6-15	Influence of suction on turbulent Prandtl number profiles, x = 70 inches	72
7-1	Comparison of different eddy heat transfer models	82
7-2	Variation of C_1 in the turbulent Prandtl number model . . .	83
7-3	Comparison of predicted Stanton numbers with experimental data, run 091871	84
7-4	Comparison of predicted Stanton numbers with experimental data, run 120471	84
7-5	Comparison of predicted Stanton numbers with experimental data, run 012472	85
7-6	Comparison of predicted Stanton numbers with experimental data, run 120271	85
7-7	Comparison of predicted temperature profile with experimental data, run 091871	86
7-8	Comparison of predicted temperature profile with experimental data, run 120471	86
7-9	Comparison of predicted temperature profile with experimental data, run 012472	87

Figure		Page
7-10	Comparison of predicted temperature profile with experimental data, run 120271	87
7-11	Influence of pressure gradient on heat transfer mixing length	88
A-1	Schematic of temperature probe	141
A-2	Comparison of temperature distribution in Chromel/constantan probe with iron/constantan probe	141

LIST OF TABLES

Table		Page
2-1	Nominal constants for free stream velocity variation	10
2-2	Nominal pressure gradient and transpiration rates studied . . .	11
4-1	Curve fit coefficients for non-transpired flows	36
9-1	Order of data tabulation	92

NOMENCLATURE

a, a_1	constants
A	van Driest length scale
A_h^+	non-dimensional heat transfer sublayer thickness, see Equation (7-18)
b, b_1	constants
B_f	$= F/(C_f/2)$, momentum blowing parameter
B_h	$= F/St$, heat transfer blowing parameter
C_1	see Equation (7-5)
C_2	see Equation (7-9)
$C_f/2$	$= \tau_o/\rho_\infty u_\infty^2$, skin friction coefficient
$(C_f/2)_{cp}$	constant property value of $C_f/2$
c_p	specific heat at constant pressure
D	see Equation (6-11)
E	$= u_\infty^2/2g_c J(T_o - T_\infty)$, Eckert number
f, f_1	functional relationship
F	$= \dot{m}''/\rho_\infty u_\infty$, blowing fraction
F_1	see Equation (2-22)
g_c	$= 32.174 \text{ ft-lbm}/(\text{lbf-sec}^2)$
G_f	$= \frac{1}{\Delta_c} \int_0^\infty \left(\frac{u_\infty - u_\tau}{u_\tau} \right)^2 dy$, Clauser shape factor
G_h	$= \Delta_4/\Delta_3$, defect enthalpy shape factor

H	= δ_1/θ , velocity shape factor
i	static enthalpy
i_0	static enthalpy at wall
i_∞	static enthalpy at free-stream
I	= $i + u^2/2 - (i_\infty + u_\infty^2/2)$, stagnation enthalpy referenced to free-stream value
I_0	= $i_0 - (i_\infty + u_\infty^2/2)$, value of I at wall
I^+	= $\left(1 - \frac{I}{I_0}\right) \sqrt{\frac{C_f/2}{\rho_\infty/\rho_0}} \frac{1}{St}$
I_d^+	= $I_\infty^+ - I^+$
J	= 778 ft-lbf/Btu
k	thermal conductivity
K	= $\frac{\nu}{u_\infty^2} \frac{du_\infty}{dx}$
ℓ	mixing length
ℓ_h^+	non-dimensional heat transfer mixing length, see Equation (7-17)
m	exponent in Equation (2-11)
m_F	exponent in Equation (2-13)
\dot{m}''	= $\rho_0 v_0$, mass injection at the wall
n	exponent in Equation (3-1)
P	static pressure
Pe_t	= $Pr \epsilon_m/\nu$, turbulent Peclet number

Pr	$= \nu/\alpha$, molecular Prandtl number
Pr_t	$= \epsilon_m/\epsilon_h$, turbulent Prandtl number
$(Pr_t)_\ell$	average value of Pr_t in log-region
\dot{q}''	heat flux
\dot{q}_0''	wall heat flux
Q^+	$= \dot{q}''/\dot{q}_0''$
Q_c^+, Q_1^+, Q_2^+	see Equation (6-8)
r	$= (Pr)^{1/3}$, recovery factor
Re_{Δ_2}	$= \frac{\rho_\infty u_\infty \Delta_2}{\nu_\infty}$, enthalpy thickness Reynolds number
Re_θ	$= \frac{\rho_\infty u_\infty \theta}{\nu_\infty}$, momentum thickness Reynolds number
St	$= \dot{q}_0''/\rho_\infty u_\infty I_0$, Stanton number
T	mean temperature
T_0	wall temperature
T_∞	free stream temperature
T'	fluctuating temperature
T^+	$= \bar{T} \sqrt{\frac{C_f/2}{\rho_\infty/\rho_0}} \frac{1}{St}$
T^*	$= \bar{T} \sqrt{\frac{St}{\rho_\infty/\rho_0}}$
\bar{T}	$= (T-T_0)/(T_\infty-T_0)$

u, v, w	components of mean velocity
u', v', w'	components of fluctuating velocity
u_∞	free-stream velocity
u_τ	$= \sqrt{\tau_0/\rho_0}$, shear velocity
u^+	$= u/u_\tau$
v_0	blowing velocity
x	streamwise coordinate
x_0, x_1	see Equations (2-21) and (2-22)
y	coordinate normal to the wall
y^+	$= y u_\tau/v_0$
y^*	$= \frac{y u_\infty}{v_0} \sqrt{St \rho_\infty/\rho_0}$
z	transverse coordinate

Greek

α	$= k/\rho c_p$, thermal diffusivity
$\alpha_1, \alpha_2, \alpha_3$	curve fit constants
β	$= \frac{\delta_1}{\tau_0} \frac{dp}{dx}$
γ	$= K \times 10^3 Re_\theta/(H-1)$
δ	momentum boundary layer thickness ($u/u_\infty = 0.99$)
δ_1	$= \int_0^\infty (1 - \frac{\rho u}{\rho_\infty u_\infty}) dy$, displacement thickness

Δ	thermal boundary layer thickness ($\bar{T} = 0.99$)
Δ_c	$= \int_0^{\infty} \frac{u_{\infty} - u}{u_{\tau}} dy$
Δ_2	$= \int_0^{\infty} \frac{\rho u I}{\rho_{\infty} u_{\infty} I_0} dy$, enthalpy thickness
Δ_3	see Equation (2-7)
Δ_4	see Equation (2-8)
ΔE	see Equation (3-5)
ΔSt	see Equation (3-6)
ϵ_m	eddy viscosity, see Equation (6-13)
ϵ_m^+	$= \epsilon_m / \nu$
ϵ_h	eddy diffusivity, see Equation (6-14)
ϵ_h^+	$= \epsilon_h / \nu$
κ	$= 0.41$, von Kármán constant
κ_h	heat transfer constant analogous to κ
λ	computational value of ℓ/δ in outer region
μ	dynamic viscosity
ν	kinematic viscosity
ρ	density
ρ_0	wall value of ρ

τ shear stress

τ_0 wall value of τ

τ^+ = τ/τ_0

ϕ see Equation (7-9)

θ = $\int_0^{\infty} \frac{\rho u}{\rho_{\infty} u_{\infty}} \left(1 - \frac{u}{u_{\infty}} \right) dy$, momentum thickness

θ' see Equation (7-5)

CHAPTER 1

INTRODUCTION

In recent years, the transpired* turbulent boundary layer has aroused considerable technical interest. It has been well established that blowing is an effective means of protecting a body from a hot fluid environment. Examples of this are found in turbine blades and rocket nozzles. Suction can be used to provide boundary layer control on high lift devices. Aside from the many important practical applications of the transpired turbulent boundary layer, any information that leads to a better understanding of the transpired turbulent boundary layer will be a significant scientific contribution.

Since 1967, the Heat and Mass Transfer Group at Stanford University has been actively engaged in an experimental and analytical program to study the transpired turbulent boundary layer. Simpson [1] reported on the hydrodynamic behavior of the constant pressure layers, and Moffat [2] and Whitten [3] reported on the heat transfer behavior of the same flows; Julien [4] and Loyd [5] studied the hydrodynamics of accelerating flows, and Thielbahr [6] and Kearney [7] studied the heat transfer behavior of the same flows. The above work has been summarized by Kays [8]. The present study is concerned with the heat transfer behavior of decelerating, or adverse pressure gradient, transpired turbulent boundary layers, and is a logical extension of the earlier work done by the Heat and Mass Transfer Group at Stanford. Coincident with this work, Andersen [9] studied the hydrodynamics of adverse pressure gradient flows.

Only one experimental study of the transpired turbulent boundary layer with adverse pressure gradients has been reported in the literature. McLean [10] investigated strong adverse pressure gradients with blowing, with primary emphasis on the onset of separation. McLean's [10] initial velocity was 155 ft/sec with a linear decrease in the streamwise direction.

* The term transpiration is used to indicate that the normal component of velocity at the wall is non-zero; blowing and suction indicate mass injection into and out of the main flow, respectively.

Velocity profiles were measured with a pitot probe and skin friction was determined from Stevenson's [11] law of the wall. Stanton numbers were measured but no temperature profiles were taken. Seban [27], Moretti [28], Perry [12], and Hatton [13] reported Stanton numbers for adverse pressure gradient flows but with no transpiration. None of the above heat transfer studies drew any conclusions about the effect of pressure gradient and/or transpiration on the turbulent Prandtl number.

The objectives of the present study are as follows:

1. Provide Stanton number and temperature profile data for near equilibrium flow conditions that would serve as a standard of comparison for future turbulent boundary layer prediction methods.
2. Ascertain the influence of the combined effects of adverse pressure gradient and transpiration on the Stanton number for the turbulent boundary layer.
3. Determine turbulent Prandtl number variation in the boundary layer (from mean profile measurements), and ascertain the influence of adverse pressure gradient and transpiration on the turbulent Prandtl number.
4. Develop a turbulent Prandtl number model that would allow one to predict heat transfer to the turbulent boundary layer under the influence of adverse pressure gradient and transpiration boundary conditions.

CHAPTER 2

BOUNDARY CONDITIONS: SURFACE TEMPERATURE, FREE STREAM VELOCITY AND TRANSPIRATION RATE

In designing a heat transfer experiment which is not directly related to a particular hardware application, the experimenter must choose the boundary conditions he would like to investigate. Boundary conditions in this sense refer to the streamwise variations of surface temperature, free stream velocity and transpiration rate. There exists an infinite number of possible choices for each of the above three boundary conditions, and the experimenter must choose carefully in order to gain the maximum amount of information from his experiment.

The outer 90% of the boundary layer responds slowly to changes in boundary conditions. Consequently the influence of a change in boundary conditions would be felt far downstream from where the change occurred. This slow response of the boundary layer would make interpretation of the data more difficult and might mask some of the more important results. On this basis, boundary conditions which produce rapid changes (over short distances) in Stanton number and mean temperature profiles were rejected, including: step changes in surface temperature, free stream velocity and transpiration rate as well as adverse pressure gradients strong enough to cause separation.

The thermal boundary layer is directly influenced by the mean velocity profile and the fluctuating velocity v' through the term $\overline{T'v'}$. Hence, it seems natural to consider the momentum boundary layer first in designing a meaningful heat transfer experiment. Since the outer 90% of an equilibrium momentum boundary layer has defect-similarity, it was decided to restrict this study to equilibrium (or at least near-equilibrium) flows. The problem of how to construct an equilibrium momentum boundary layer and an equilibrium thermal boundary layer will be discussed in subsequent sections.

2.1 Velocity Defect Similarity

Clauser [14] first introduced the concept of an equilibrium momentum boundary layer. He defined this as a layer in which the defect velocity is an unique function of y/δ , i.e.,

$$\frac{u_\infty - u}{u_\tau} = f_1(y/\delta) . \quad (2-1)$$

Since the momentum boundary layer thickness is ill-defined, Clauser [14] replaced δ by a new thickness parameter Δ_c defined by

$$\Delta_c = \delta \int_0^1 \frac{u_\infty - u}{u_\tau} d(y/\delta) . \quad (2-2)$$

Therefore, (2-1) can be equivalently written as

$$\frac{u_\infty - u}{u_\tau} = f_1(y/\Delta_c) . \quad (2-3)$$

A shape factor describing the defect velocity profile was defined as

$$G_f = \frac{\delta}{\Delta_c} \int_0^1 \left(\frac{u_\infty - u}{u_\tau} \right)^2 d(y/\delta) . \quad (2-4)$$

From (2-3) and (2-4) it follows that an equilibrium momentum boundary layer has a constant value of G_f . It should be noted that G_f is only approximately constant for an equilibrium flow, since the inner 5-10% of the momentum boundary layer does not have defect similarity.

2.2 Temperature (Enthalpy) Defect Similarity

Equation (2-1) can also be written as

$$u_\infty^+ - u^+ = f_1(y/\delta) . \quad (2-5)$$

By analogy with (2-5), let us propose a defect temperature law of the form

$$T_\infty^+ - T^+ = f_2(y/\Delta) , \quad (2-6)$$

where Δ is the thermal boundary layer thickness. The validity of this proposed defect temperature law must be verified experimentally, and this will be done in CHAPTER 5. In order for this defect temperature law to be valid for high velocity flows or flows with chemical reactions, a more general defect enthalpy law is proposed.

$$I_d^+ = I_\infty^+ - I^+ = f_2(y/\Delta) \quad (2-6a)$$

Following Clauser [14] one can define two thickness parameters that are related to the defect enthalpy profile by

$$\Delta_3 = \Delta \int_0^1 (I_\infty^+ - I^+) d(y/\Delta) \quad (2-7)$$

and

$$\Delta_4 = \Delta \int_0^1 (I_\infty^+ - I^+)^2 d(y/\Delta) \quad (2-8)$$

It can be shown that the relationship between T^+ and I^+ is

$$I^+ = \frac{1}{1 - E/2} \left(T^+ - \frac{E}{2} \frac{\rho_\infty}{\rho_0} \frac{(C_f/2)^{3/2}}{St} u^{+2} \right) \quad (2-9)$$

For the range of velocities considered in this study, T^+ and I^+ are essentially identical.

From (2-7), it is obvious that one can replace the ill-defined thermal boundary layer thickness with a more useful thickness parameter Δ_3 . In this study, all defect enthalpy profiles will be shown as a function of y/Δ_3 .

A defect enthalpy profile shape factor can be defined as

$$G_h = \frac{\Delta_4}{\Delta_3} \quad (2-10)$$

If outer layer similarity exists for the defect enthalpy, then G_h should be approximately constant. In this study, the equilibrium turbulent thermal boundary layer is defined as a boundary layer for which the defect enthalpy is a function of y/Δ_3 , in the outer part of the layer.

2.3 Surface Temperature Variation

The surface temperature was kept at a constant value (for a given run) within the limits of the experimental apparatus. The temperature difference across the boundary layer varied from one run to the next but was kept in the range 20-30°F in order to minimize the influence of temperature-dependent properties.

2.4 Free Stream Velocity Variation

When Clauser [14] established his equilibrium momentum boundary layer, a long trial and error procedure was necessary. Bradshaw [15] concluded, from his own experiments and the earlier data of Clauser [14], that an adverse equilibrium momentum boundary layer would be experimentally established if the free stream velocity varied in the manner

$$u_{\infty} \sim x^m, \quad m < 0. \quad (2-11)$$

Neither Clauser [14] nor Bradshaw [15] considered the effects of transpiration. In a companion study to the present work, done by Andersen [9], it was concluded that an equilibrium momentum boundary layer with transpiration could be experimentally established if the free stream velocity were given by (2-11), and if the transpiration fraction F is proportional to x^{m_F} , $m_F < 0$. It should be noted that m_F is a function of m , and this will be discussed in greater detail in the next section.

2.5 Transpiration Rate for Equilibrium Flows

For two-dimensional incompressible constant property flow, the momentum integral equation can be written in the form:

$$\frac{d}{dx} (\theta u_{\infty}^2) = \frac{\tau_0}{\rho} (1 + \beta + B_f), \quad (2-12)$$

where $B_f = \rho v_0 u_{\infty} / \tau_0$ is a momentum transfer blowing parameter. Andersen [9] demonstrated that if both β and B_f were constant, then G_f was also a constant and equilibrium flow was established. He also showed that if one makes three assumptions:

$$(a) \quad u_\infty = u_1 x^m ,$$

where u_1 and $m < 0$ are constants,

$$(b) \quad (C_f/2)_0 = a Re_\theta^{-b} ,$$

where a and b are constants and $(C_f/2)_0$ is the skin friction for the non-transpired flow corresponding to (a), and

$$(c) \quad \left(\frac{C_f}{C_{f_0}} \right)_{m, Re_\theta} = f(B_f) ,$$

then the transpiration fraction F must vary according to

$$F \sim x^{m_F}, \quad m_F = - (1 + m) \frac{b}{1 + b} \quad (2-13)$$

We will now go through a similar analysis for the heat transfer problem. The energy integral equation for two-dimensional flow with negligible density fluctuation can be written as

$$\frac{d}{dx} (\rho_\infty u_\infty I_0 \Delta_2) = \dot{q}_0'' (1 + B_h) , \quad (2-14)$$

where $B_h = \rho_0 v_0 I_0 / \dot{q}_0''$ is a heat transfer blowing parameter. Physically, B_h represents the ratio of the transpiration energy flux to the wall heat flux. In comparing (2-12) and (2-14), note the absence of an explicit pressure gradient term analogous to β for the heat transfer problem. This leads one to suspect that the Stanton number behavior will be quite different from the skin friction behavior for adverse pressure gradient flows.

The analysis of Andersen [9] for the momentum transfer problem leads one to suspect that if we are able to experimentally establish a flow for which B_h is a constant, then G_h might also be constant. With this idea in mind, we will now proceed to determine the variation in transpiration rate necessary to experimentally establish a constant B_h flow.

In the analysis that follows, it will be necessary to make the following assumptions:

$$(a) \quad u_{\infty} = u_1 x^m ,$$

where u_1 is constant,

$$(b) \quad St_0 = a_1 Re_{\Delta_2}^{-b_1} ,$$

where a_1 and b_1 are constants and St_0 is the Stanton number for the free stream velocity variation given by (a) but for no transpiration, and

$$(c) \quad \left(\frac{St}{St_0} \right)_{m, Re_{\Delta_2}} = f_1(B_h) .$$

Assumption (c) implies that for a given pressure gradient, i.e., given $m < 0$, the ratio of St for the transpired flow to St for the non-transpired flow at the same enthalpy thickness Reynolds number Re_{Δ_2} , is a function of the heat transfer blowing parameter B_h only. This assumption was verified experimentally by Whitten [3] for the special case of $m = 0$ and will be verified for $m < 0$ in CHAPTER 4.

If we further assume constant properties and constant wall temperature, (2-14) can be written as

$$\frac{d Re_{\Delta_2}}{dx} = \frac{u_{\infty}}{\nu} St(1 + B_h) . \quad (2-15)$$

Applying assumptions (a)-(c), (2-15) becomes

$$\frac{d Re_{\Delta_2}}{dx} = a_1 \frac{u_1}{\nu} f_1(B_h) (1 + B_h) x^m Re_{\Delta_2}^{-b_1} . \quad (2-16)$$

The solution to (2-16), subject to the initial condition $Re_{\Delta_2} = 0$ at $x = 0$, is

$$Re_{\Delta_2} = \left[a_1 \frac{u_1}{\nu} f_1(B_h) (1 + B_h) \frac{b_1 + 1}{m + 1} \right] x^{\left(\frac{1+m}{1+b_1} \right)} . \quad (2-17)$$

From the definition of B_h and assumption (b), one can write

$$F = B_h f_1 (B_h) a_1 Re_{\Delta_2}^{-b_1} . \quad (2-18)$$

Substituting for Re_{Δ_2} in (2-18), one finds that the transpiration rate variation necessary to maintain a constant B_h flow is given by

$$F \sim x^{m_F} , \quad m_F = - b_1 \left(\frac{1+m}{1+b_1} \right) . \quad (2-19)$$

On comparing (2-13) and (2-19), one concludes that the variation in the transpiration fraction F necessary to produce a constant B_f flow will also produce a constant B_h flow provided that b and b_1 are the same. Physically, b and b_1 are the slopes of a log-log plot of $(C_f/2)_0$ vs. Re_θ and $(St)_0$ vs. Re_{Δ_2} , respectively. From the data of Andersen [9] and the data to be reported in CHAPTER 4, $b = b_1 = 0.25$. Zero pressure gradient ($m = 0$) is a special case of (2-19), and this case was studied experimentally by Simpson [1] and Whitten [3].

In conclusion, the boundary conditions that will yield a constant B_h flow will be taken to be

$$u_\infty \sim x^m , \quad F \sim x^{m_F} , \quad m_F = - b \left(\frac{1+m}{1+b} \right) . \quad (2-20)$$

Establishing these boundary conditions should produce an equilibrium thermal boundary layer.

Before turning to the details of the boundary conditions established in this study, it should be pointed out that in developing these relationships, it has been assumed that the boundary layer, the pressure gradient, and the transpiration rate all have a common origin at $x = 0$. In this study, the origin of the momentum boundary layer was slightly upstream of the thermal boundary layer. Also, $x = 0$ corresponds to an infinite free-stream velocity and transpiration rate, both of which are physically impossible. Consequently, the actual conditions did not exactly match the desired ones near the beginning of the test section. The influence of the entrance effects should not drastically alter the

test results far downstream. This point will be discussed in greater detail in CHAPTER 5.

2.6 Actual u_∞ and F Variations

Three different nominal free stream velocity variations were established in this study. They each may be approximately represented by an equation of the form:

$$u_\infty = u_1 \left(\frac{x - x_0}{x_1 - x_0} \right)^m \quad (2-21)$$

The nominal constants in (2-21) for the three different pressure gradients of this study are tabulated in Table 2-1.

m	u_1 (ft/sec)	x_0 (in)	x_1 (in)
0.00	31.1	-	-
-0.15	29.2	-3	4
-0.20	29.2	-2	4

Table 2-1: Nominal constants for free stream velocity variation

The transpiration boundary conditions considered in this study can be expressed in the form

$$F = F_1 \left(\frac{x - x_0}{x_1 - x_0} \right)^{m_F} \quad (2-22)$$

In addition to the $B_h = \text{constant}$ flows, a series of $F = \text{constant}$ flows were also established. The combinations of pressure gradient and transpiration rate considered are tabulated in Table 2-2.

m	F_1	m_F
0.00	0.000	-
-0.15	0.000	-
	± 0.001	0.00 and -0.17
	± 0.002	
	± 0.004	
-0.20	0.000	-

Table 2-2: Nominal pressure gradient and transpiration rates studied

The zero pressure gradient ($m = 0$), no transpiration case was part of a series of qualification tests. Most of this study was concerned with the pressure gradient $m = -0.15$ for a wide range of transpiration rates.

2.7 Identification of the Boundary Conditions

From the previous section, it is obvious that the three parameters (m, F_1, m_F) nominally describe the pressure gradient and transpiration boundary conditions. Therefore, each run will be identified by these three parameters. For example, the run designation $(-0.15, -0.004, -0.17)$ will indicate $u_\infty \sim x^{-0.15}$, $F_1 = -0.004$, and $F \sim x^{-0.17}$. For the runs with F constant, the third parameter m_F is not necessary. The run designation $(-0.20, 0.000)$ indicates $u_\infty \sim x^{-0.20}$ and $F_1 = 0.000$ everywhere. For the constant B_h runs, a three-parameter designation is necessary, while only two are necessary for the constant F runs.

CHAPTER 3

EXPERIMENTAL APPARATUS, INSTRUMENTATION, AND QUALIFICATION TESTS

The basic apparatus used in this study was an open-end wind tunnel. The apparatus was first described by Moffat [2], and a description of subsequent modifications can be found in References [1] and [3]-[7]. A schematic diagram of the wind tunnel is shown in Figure 3-1.

The wind tunnel was originally designed for zero pressure gradient studies of the transpired turbulent boundary layer. Subsequent studies were concerned with accelerating flows. This heat transfer study and a parallel hydrodynamics study by Andersen [9] were concerned with adverse pressure gradient effects on the transpired turbulent boundary layer. Consequently, the only major modification of the basic apparatus was to design a new upper surface for the test channel used to create the pressure gradient. The adverse pressure gradient is created by a series of adjustable slots on the top wall which removes the boundary layer that forms along this upper surface.

Since the apparatus has been adequately described in the above references, only a brief description will be given below, along with a detailed description of any major modifications made for this study.

3.1 Main Air Flow

Referring to Figure 3-1, the main air flow enters the filter box, with the filter material being 0.7 micron retention felt-type material. The main air blower is of the centrifugal type and has a 2000 scfm capacity at 30 inches of water. The flow-turning header was designed to provide a uniform velocity at the heat exchanger. Honeycomb is placed both upstream and downstream of the main flow heat exchanger. This heat exchanger is supplied with cooling water from the Stanford University water system. During peak water-usage periods, considerable fluctuations were noted in the incoming water supply. Since this heat exchanger has a very high effectiveness, the fluctuating cooling water temperature caused a

fluctuating main air temperature. In order to damp these fluctuations, the cooling water is first passed through two large tanks in series, each with a capacity of approximately 5000 gal. The nominal cooling water flow rate was 40 gal/min.

After leaving the heat exchanger, the main flow air passes through 1-1/2 inch thick honeycomb with 3/16 inch cell size. Following the honeycomb and located in a constant area section 23 x 23 inches are six 32 x 32 mesh stainless steel screens. The function of this set of screens is to remove any non-uniformities in dynamic pressure. During the preliminary stages of this study, it was found that the last screen which the air passes through had a slight crease in it. This slight crease considerably affected the uniformity of the potential core in the test section and the screen had to be replaced.

Following the screen pack, the flow enters a 4:1 contraction (over 26 inches) nozzle. The nozzle provides an almost two-dimensional contraction from the 23 x 23 inch inlet to the 6 x 20 inch outlet. The nozzle is symmetric about both a vertical plane and a horizontal plane, with the contraction taking place primarily in the vertical plane. In the preliminary stages of this study, it was concluded that a separation occurred at the inlet of the nozzle. Consequently, the basic shape of the nozzle was modified to incorporate an initial contracting angle of approximately 5° downstream of the last screen.

At the exit of the nozzle, a 3/16 inch wide slot was cut across the bottom and side walls of the nozzle. Since the static pressure in the tunnel is slightly above atmospheric, this suction slot removes the boundary layer that develops in the nozzle. To insure a fully turbulent profile at the first test plate, a 1/32 inch high by 1/4 inch wide boundary layer trip is located 6 inches upstream of first test plate. There were no trips on the side or top walls.

3.2 Test Section

The test section consists of a 6 x 20 inch rectangular cross section duct 8 feet in length. The side walls are 1/2 inch plexiglass, the top is 5/16 inch aluminum tool plate, and the bottom wall (the actual test surface) is porous sintered bronze.

One of the side walls contains static pressure taps, which are used in conjunction with Kiel probes for total pressure. Free stream velocity variations can be deduced from these pressures. The side wall static pressure taps are 0.040 inch diameter with a sharp edge and are spaced two inches apart in the streamwise direction. The distance above the bottom wall test surface is 1 inch. Every 12 inches in the streamwise direction four additional pressure taps are provided at 2, 3, 4, and 5 inches above the test surface, on both side walls. The function of these vertical columns of pressure taps was to check the static pressure uniformity in the vertical and transverse directions. The side-to-side static pressure variation was found to be less than 0.002 inches of water. The pressure variation in the vertical direction was less than 0.001 inches of water, which is also the accuracy of the pressure measuring system. The static pressure taps are evident in Figure 3.2.

The bottom wall of the test section consists of 24 individual porous test plates, and they are mounted in four separate aluminum base castings. Each plate is thermally isolated from the base casting and the neighboring plates. The physical characteristics of the plates are as follows:

Material - sintered porous bronze

Dimensions - 18.0 x 3.975 x 0.25 inches

Particles - spherical, varying in diameter in the range 0.002-0.007 inches

Porosity - Approximately 40%, uniform within $\pm 6\%$ in center 6-inch section

Roughness - maximum of 200 microinches (RMS) measured with a stylus of 0.0005 inch radius

Thermal conductivity - 6.5 Btu/hr-ft-F, minimum

Surface emittance - 0.37 average.

Plate temperatures are monitored by five Iron/constantan thermocouples, each located 0.040 inches below the surface. The spacing of the plate thermocouples is shown in Figure 3.3. Each plate is electrically heated by nichrome wires which are located in grooves on the underside of the plate. Separate AC power supplies, both stabilized, are available for plates 1-12 and 13-24. In addition, the power supplied to each plate

is individually controlled by a rheostat. This allows one to vary the power to each plate individually to maintain a uniform surface temperature.

The upper wall of the test section is used to control the pressure gradient. It consists of a series of 24, 5/16 inch thick by 3.5 inches wide aluminum plates. These plates are arranged on top of the side walls such that there is a 1/2 inch space (in the flow direction) between adjacent plates. Each of the 23 resulting 1/2 inch wide slots is partially covered by two 1/2 inch thick aluminum bars. One of the above two bars is permanently fixed to the 3.5 inch plate, while the other bar is allowed to move relative to the fixed bar. The result is to form a slot whose width can be varied between 0 and 0.4 inches. A side view of the tunnel with the slot arrangement is shown in Figure 3-4. A feeler gauge allows the slot widths to be set to within 0.001 inches. Wing nuts are used to keep the movable bar in place once the slot width has been set and can be seen in Figure 3-2.

The test section is extended 14 inches past the last heated plate. A movable gate which slides up and down vertically is across this extension piece. This gate valve and a throttle valve at the main stream air blower are used to control the main stream air flow rate. The function of this extension is to insure that influence of the sliding gate valve is not appreciably felt at the last test station.

3.3 Transpiration Air System

The transpiration air system is quite similar to the main air system. The main difference is that after leaving the transpiration blower, the air goes to a header and then to 24 individually calibrated rotameters. Actually, the air supplied to a given plate can be routed to one of two rotameters, depending on the magnitude of the flow rate. By using the two rotameters in parallel, flow rates in the range of 0.5 to 18 scfm can be measured. Each of these 48 rotameters was individually calibrated by Kearney [7]. A typical transpiration compartment and plate assembly is shown in Figure 3-5.

3.4 Pressure Measurements

All pressure measurements were made with a STATHAM type PM-97 unbonded strain gauge differential pressure transducer for pressures in the range 0-1.4 inches of H_2O . The Wheatstone bridge was excited by a stable Hewlett-Packard model 6213A DC power supply. The output voltage from the pressure transducer was read by a Vidar 5206 D-DAS data acquisition system employing a digital PDP 8/L computer. The integration time was in the range of 6-10 seconds for each pressure measurement.

The pressure transducer was calibrated with a Meriam model 34FB2 micromanometer, and was found to be linear within ± 0.001 inches of H_2O .

3.5 Velocity Measurements

The free stream velocity was determined by a Kiel probe, side wall static pressure taps, the pressure transducer, and Bernoulli's equation. The technique by which the slots were adjusted to obtain a given free stream velocity variation is described by Andersen [9]. The mean velocity profiles used in this thesis were taken from the parallel hydrodynamics study by Andersen [9], and were measured using a linearized constant temperature hot-wire anemometer. In general, the y-locations at which the velocity was measured differed from the y-locations at which the temperature was measured. Consequently, it was necessary to interpolate in the velocity profile to obtain data at the corresponding temperature y-locations. The interpolation scheme used was an average of two three-point Lagrangian interpolations, centered about the data point in question.

The data of Andersen [9] was taken under isothermal conditions. The corresponding data of this study was taken with a boundary layer temperature difference of 20-30°F. Consequently, some care must be exercised in using isothermal hydrodynamics data with the slightly variable density data of this study. Typically, the density ratio ρ_∞/ρ_0 was of the order 1.04. Thielbahr [6] investigated, both experimentally and numerically by a computer solution of the boundary layer equations, the question of which one of the following quantities would most nearly be preserved: a) u/u_∞ , b) $\rho u/\rho_\infty u_\infty$, or c) $\rho u^2/\rho_\infty u_\infty^2$. He found that, under similar free-stream conditions, the minimum error in the computation of integral parameters

by mixing isothermal and non-isothermal data was achieved by assuming the preservation of u/u_∞ . The same procedure was followed in this study.

3.6 Skin Friction

The skin friction reported in this study is taken directly from the parallel study of Andersen [9]. Kays [16] reports that the effect of variable properties on skin friction can be approximately correlated by

$$\frac{C_f}{(C_f)_{cp}} = \left(\frac{T_o}{T_\infty} \right)^n, \quad (3-1)$$

where the exponent $n = -0.5$ is valid for this study. This indicates that the variable property skin friction should be approximately 2% lower than the corresponding constant property skin friction. Since the data of Andersen [9] are not accurate to within 2%, it was concluded that this correction was not justified.

3.7 Mean Temperature Profile Measurements

Considerable time was spent in developing a boundary layer temperature probe that would have acceptable conduction losses when used near the wall. The final probe design is shown in Figure 3-6. The sensing element of the probe is a Chromel/constantan thermocouple of 0.003 inch diameter wire. The thermocouple junction is formed by butt welding the two thermoelectric elements together. After welding, the wire was rolled between two pieces of flat steel in order to remove any kinks. The sensing element was supported between two 22 gauge stainless steel hypodermic needles with the teflon-coated wire being inside the hypodermic needle. This teflon coating was burned off the part of the thermocouple that was exposed to the air stream. Consequently, contact between the bare wire and the hypodermic needle occurred only at the end of the hypodermic needle. Since the two hypodermic needles were electrically insulated from each other, this contact did not introduce any error. The shape of the hypodermic needles was such as to give some spring to the probe assembly when in contact with the wall. The span between the probe prongs was approximately 0.5 inches, with the junction in the middle of the span.

APPENDIX A presents an analysis of the expected temperature distribution in the probe and the approximate temperature error.

After the probe was assembled, an optical comparator was used to insure that both prongs would touch the wall at approximately the same time. This was accomplished to within 0.0015 inches. From the experimental temperature profiles, a difference in y-location of 0.0015 inches, in very near the wall, might cause the two ends of the probe to be at temperatures that differ by 0.3°F for the strongest blowing run to 1.5°F for the strongest suction run. Consequently, it should be expected that the probe performance in near the wall would be the worst for the suction runs. Therefore, it was decided that the first data point greater than $y^+ = 3 - 9$ (depending on the transpiration rate and pressure gradient) would be forced to match the laminar sublayer equation. This was accomplished by shifting all of the y-locations (for a given profile) by a fixed amount. Typically, this shift was ± 0.0015 inches.

The boundary layer temperature probe was mounted in a micrometer-traversing mechanism that was adjustable to the nearest 0.001 inch.

The temperature probe should measure a temperature somewhere between the local static and the stagnation temperature. In this study, it was assumed that the static temperature is related to the indicated probe temperature by the relationship

$$T = T_{\text{probe}} - r \frac{u^2}{2g_c J c_p} , \quad (3-2)$$

where r , the recovery factor, was taken to be $(Pr)^{1/3}$. The maximum value of the quantity $u^2/2g_c J c_p$ for this study was about 0.08°F. Hence, the actual value of the recovery factor was not significant for the velocities of this study.

3.8 Stanton Number

The Stanton number reported in this study is defined through the relationship

$$St = \frac{\dot{q}_0''}{\rho_\infty u_\infty I_0} , \quad (3-3)$$

where \dot{q}_0'' is the wall heat flux and I_0 is the stagnation enthalpy at the wall referenced to the free stream stagnation enthalpy. The static enthalpy was calculated from the static temperature by

$$i = c_p T ,$$

where the specific heat c_p was assumed to be independent of temperature but did depend on the water vapor present in the air. The relative humidity was determined with a sling psychrometer and the mass fraction of water vapor was computed using the data of Keenan [17].

The wall heat flux \dot{q}_0'' was determined by performing an energy balance on the center six-inch section of each test plate. This energy balance can be written symbolically as

$$\text{Power} = \text{Convection} + \text{Transpiration} + \text{Losses} , \quad (3-4)$$

where

Power - electrical power used to heat the plates

Convection - wall heat flux \dot{q}_0''

Transpiration - energy flux due to mass injection

Losses - heat transfer to the surroundings by radiation from the top and bottom of the plate and conduction from the plate to its supports.

The mathematical model for the loss terms is the same as that used by Kearney [7] and will not be discussed here. The thermocouples in the plates and a thermocouple in the underbody of the transpiration compartment were used to measure the temperature of the transpiration air. The electrical power was measured by a Singer model DW precision watt meter.

3.9 Qualification of the Apparatus

A series of tests was performed to qualify the basic characteristics of the apparatus. These tests consisted of (1) transpiration energy balances, (2) transverse uniformity of the mean temperature and velocity

profiles, (3) boundary layer energy balances, and (4) repeatability of earlier zero pressure gradient, zero transpiration studies of Moffat [2], Whitten [3], Theilbahr [6], and Kearney [7].

3.9.1 Transpiration Energy Balances

If there is no main stream flow in the wind tunnel, the Convection term in the energy balance Equation (3-4) is identically zero.* Consequently, the left and right hand sides of (3-4) can be evaluated independently. Any discrepancy between the left and right hand sides of (3-4) will be an energy imbalance. Let us define an energy imbalance term as

$$\Delta E = \text{Power} - (\text{Transpiration} + \text{Losses}) \quad . \quad (3-5)$$

Since we are more concerned with the effects of this energy imbalance on the Stanton number under actual operating conditions, let us define

$$\Delta St = \frac{\Delta E}{\rho_{\infty} u_{\infty} I_0} \quad . \quad (3-6)$$

Since the term in the denominator of (3-6) may depend on the particular run as well as the x-location of a given run, the denominator was given the nominal value of

$$\rho_{\infty} u_{\infty} I_0 = (0.075 \text{ lbm/ft}^3)(25 \text{ ft/sec})(64.8 \text{ Btu/lbm}) \quad . \quad (3-7)$$

The results of the blowing and suction energy balance tests are shown in Figures 3-7 and 3-8, respectively. The range of blowing and suction considered in these tests span the nominal range of blowing and suction considered in the runs with main air flow. The majority of the plates show an energy imbalance within 0.0001 Stanton number units. This is consistent with the earlier findings of Kearney [7].

* In the suction mode, the energy balance control volume must be extended to $+\infty$ in the y-direction in order for this to be true.

3.9.2 Inlet Velocity and Temperature Uniformity

Velocity and temperature profiles were taken at nine transverse locations corresponding to an x-location of 10 inches; $Z = -8, -6, \dots, 6, 8$, inches. The results are shown in Figures 3-9 through 3-12. Both velocity and temperature profiles are very uniform, especially over the central portion of the test section. As was expected, the velocity profiles at $z = \pm 8$ inches show the greatest deviation, due to the side wall boundary layer. The same problem does not exist with the temperature profile. For additional comments on the velocity uniformity, see Andersen [9].

3.9.3 Boundary Layer Energy Balances

The Stanton number was determined experimentally without making use of any of the temperature or velocity profile data. However, any heat transfer at the wall must be distributed within the thermal boundary layer. Consequently, the measured temperature profiles must be consistent with the measured heat flux at the wall. This consistency can be examined with the aid of the energy integral equation. Anticipating that any real flow such as the ones studied here has some amount of three-dimensionality, let us develop the energy integral equation for a flow in which the convective motion is three-dimensional but the shear stress and heat flux have only one component. The continuity and energy equations can be written as

$$\frac{\partial}{\partial x} (\rho u) + \frac{\partial}{\partial y} (\rho v) + \frac{\partial}{\partial z} (\rho w) = 0 \quad , \quad (3-8)$$

$$\frac{\partial}{\partial x} (\rho u I) + \frac{\partial}{\partial y} (\rho v I) + \frac{\partial}{\partial z} (\rho w I) = - \frac{\partial \dot{q}''}{\partial y} + \frac{\partial}{\partial y} (\tau u) \quad . \quad (3-9)$$

Integrating (3-9) with respect to y between the wall and infinity, one obtains

$$St + F = \frac{1}{\rho_{\infty} u_{\infty} I_0} \frac{d}{dx} (\rho_{\infty} u_{\infty} I_0 \Delta_2) + 3-D \quad , \quad (3-10)$$

where the three-dimensional term is given by

$$3-D = \frac{1}{\rho_{\infty} u_{\infty} I_0} \frac{d}{dz} \int_0^{\infty} \rho w I dy \quad (3-11)$$

Insight can be gained into the 3-D term by restricting the analysis to flow in a convergent or divergent channel where the streamlines all originate from a single point. Following Schlichting [18], we have

$$\left. \frac{w}{u} = \frac{z}{x+a}, \quad \frac{\partial w}{\partial z} \right)_{z=0} = \frac{u}{x+a} \quad (3-12)$$

Substituting (3-12) into (3-11), we obtain

$$3-D = \frac{1}{\rho_{\infty} u_{\infty} I_0} \frac{d}{dz} \left(\frac{z}{x+z} \rho_{\infty} u_{\infty} I_0 \Delta_2 \right) \quad (3-13)$$

Since the primary temperature and velocity profiles were taken along the center line ($z = 0$) of the wind tunnel, it seems reasonable to restrict (3-13) to $z = 0$. Consequently,

$$3-D)_{z=0} = \frac{\Delta_2}{x+a} \quad (3-14)$$

Diverging streamlines correspond to $x+a > 0$, while converging streamlines correspond to $x+a < 0$.

If plate energy balances were not available, one could compute the Stanton number from the temperature profiles and the energy integral equation. However, it would be necessary to evaluate the 3-D term. Consequently, we will use the energy integral equation to tell us something about the magnitude of the 3-D effects.

Let us define a two-dimensional Stanton number through the relationship

$$(St)_{2-D} = \frac{1}{\rho_{\infty} u_{\infty} I_0} \frac{d}{dx} (\rho_{\infty} u_{\infty} I_0 \Delta_2) - F \quad (3-15)$$

The two-dimensional Stanton number and the actual plate Stanton number are then related by

$$St = (St)_{2-D} + 3-D \quad . \quad (3-16)$$

From (3-16), and the physical situation, we conclude that

$$\begin{aligned} St > (St)_{2-D}, & \text{ diverging streamlines ,} \\ St < (St)_{2-D}, & \text{ converging streamlines .} \end{aligned} \quad (3-17)$$

For all the data presented in this study, the term $(St)_{2-D}$ was calculated. The results are presented in the data tabulation, CHAPTER 9. In general, the flow exhibited a slight amount of streamline divergence. The exception was the high blowing runs which had streamline divergence at the beginning of the test section but streamline convergence at the end of the test section. In computing the derivative in (3-13), a least-squares curve fit of the form

$$\rho_{\infty} u_{\infty} \Delta_2 = \alpha_1 (x + \alpha_2)^{\alpha_3} \quad (3-18)$$

was generated and the derivative evaluated analytically. The I_0 term was omitted under the assumption of constant wall temperature.

3.9.4 Zero Pressure Gradient, Zero Transpiration Flow

The zero pressure gradient, zero transpiration turbulent boundary layer has been studied by many investigators. Therefore, this flow provides a good test of the wind tunnel and data-reduction system.

All of the Stanton number data for this study will be presented in the form of Stanton number vs. enthalpy thickness Reynolds number. Stanton numbers were measured for each of the 24 test plates, but the data from plates 1, 2, and 24 will not be presented because of entrance and exit effects and conduction losses. Boundary layer measurements of enthalpy thickness Reynolds numbers are available only for the x-locations where temperature and velocity profiles were measured (8 or 9 stations). Kearney [7] obtained Re_{Δ_2} for the centerline of each plate by solving (3-10) for Δ_2 and neglecting the 3-D term.

$$\rho_{\infty} u_{\infty} I_0 \Delta_2 = (\rho_{\infty} u_{\infty} I_0 \Delta_2) \Big|_{x_0} + \int_{x_0}^x \rho_{\infty} u_{\infty} I_0 (St + F) dx \quad (3-19)$$

This approach has the disadvantage that the Re_{Δ_2} computed from (3-19) can differ considerably from Re_{Δ_2} obtained from profile measurements because of streamline convergence or divergence. Since this is a cumulative effect, the error will increase with x . It was felt that a better approach would be to least-squares curve-fit the profile enthalpy thickness Reynolds number in the form

$$Re_{\Delta_2} = \alpha_1 (x + \alpha_3)^{\alpha_2} \quad (3-20)$$

and then evaluate the curve fit at the plate centerline x -locations. Equation (3-20) was found to be a very good representation for all of the data presented in this study. All of the values of Re_{Δ_2} that are tabulated in CHAPTER 9 under the heading of Stanton number results were obtained from (3-20). The actual values of Re_{Δ_2} computed from the profile measurements are tabulated in the temperature profile results section of CHAPTER 9.

Figure 3-13 shows a comparison of the zero pressure gradient, zero transpiration data of this study with the earlier data of Kearney [7]. The comparison is very good, with the worst deviation occurring at the higher Reynolds numbers. This discrepancy can be explained by the different manner in which Re_{Δ_2} was computed. Kearney [7] indicated that a slight streamline divergence was present in his flat plate data. This effect indicates that his Re_{Δ_2} computed from (3-19) would be larger than the corresponding profile measurements. If Kearney's data are shifted to the left in Figure 3-13 to account for this streamline divergence, the agreement would be even better.

Using the step function solution presented by Reynolds [20], it can be shown that the effects of an unheated starting length for the zero pressure gradient turbulent boundary layer can be approximately accounted for by the relationship

$$St = (St)_{eq} \left(Pr^{0.4} \frac{Re_{\Delta_2}}{Re_{\theta}} \right)^{5/36}, \quad \frac{Re_{\Delta_2}}{Re_{\theta}} < 1, \quad (3-21)$$

where $(St)_{eq}$ denotes the value of Stanton number that would have existed if both boundary layers had a common origin. The closed symbols in Figure 3-13 have been moved upward according to (3-21). The solid line in Figure 3-13 was taken from Moffat [19]. The agreement is quite good.

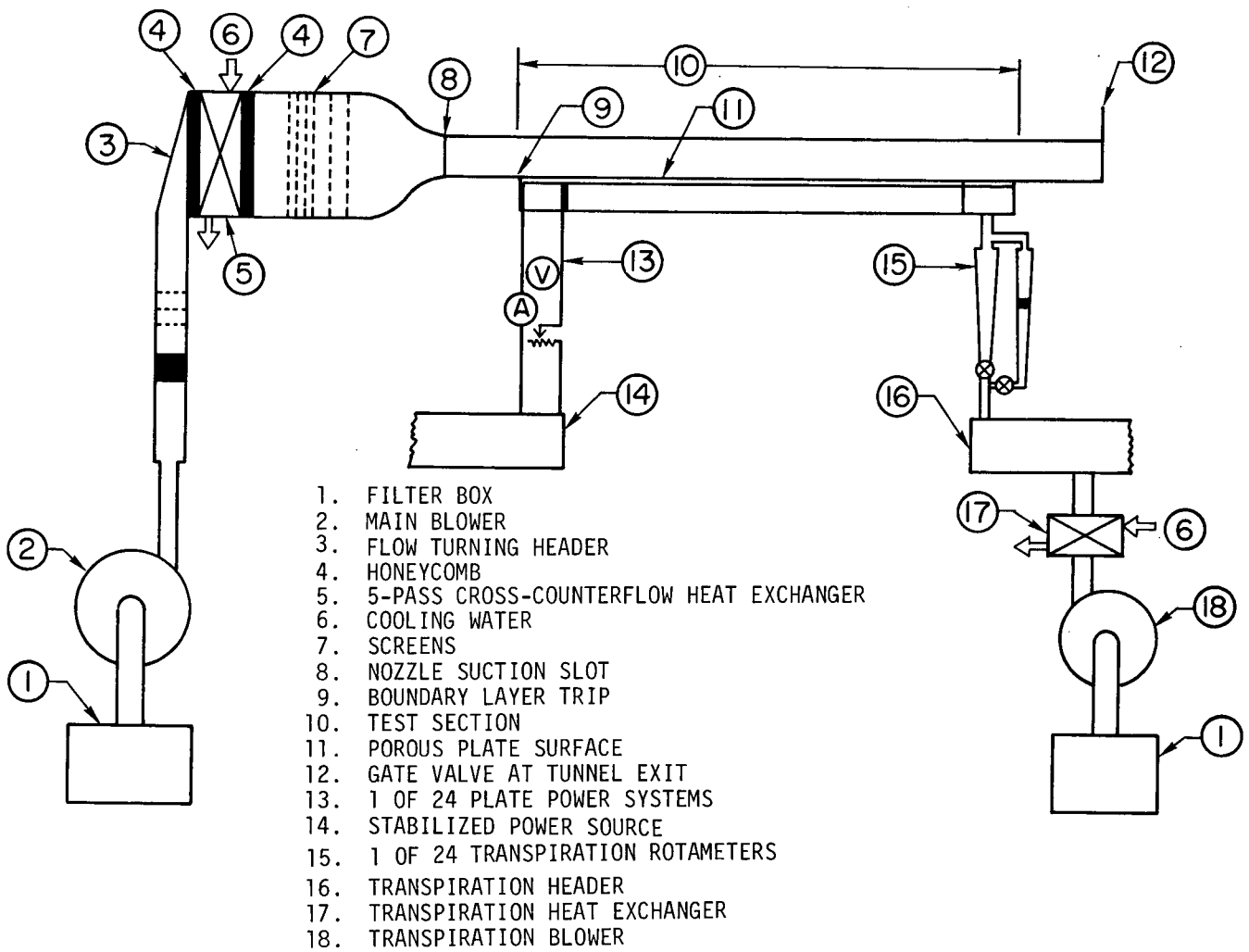


Figure 3-1 Schematic of test apparatus

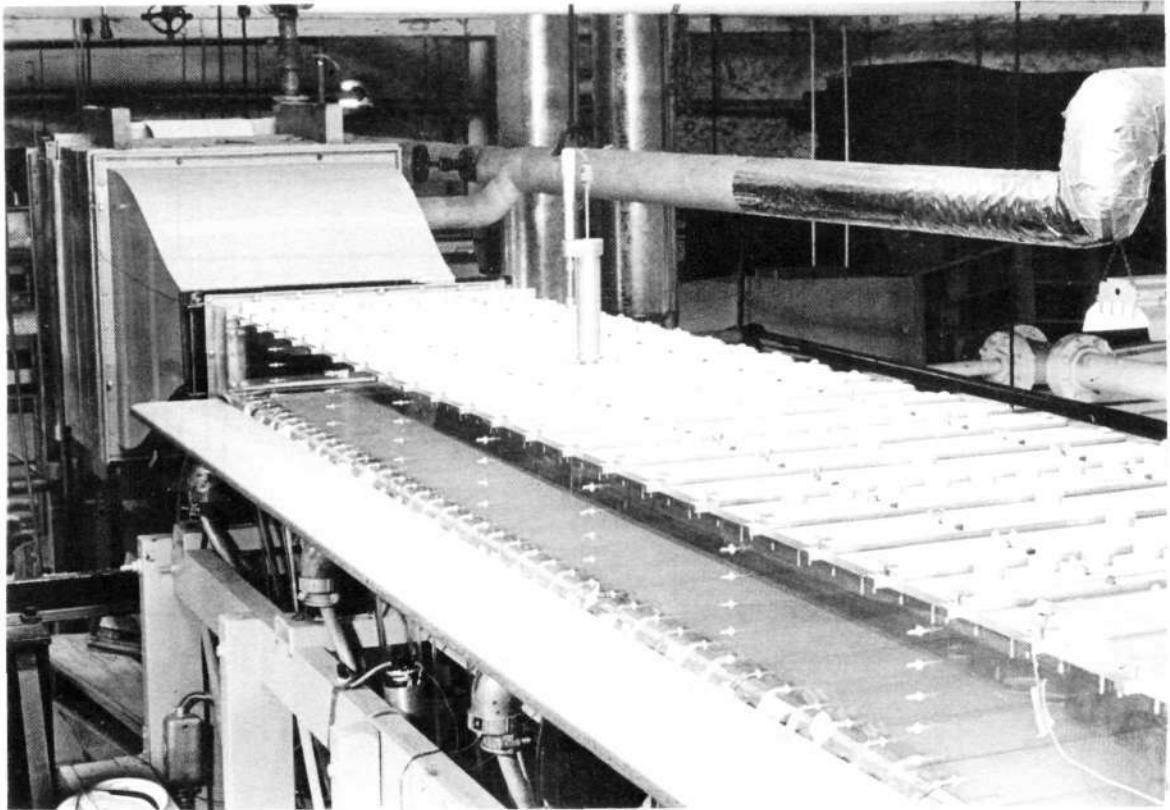


Figure 3-2 Photograph of test section with traversing mechanism in position

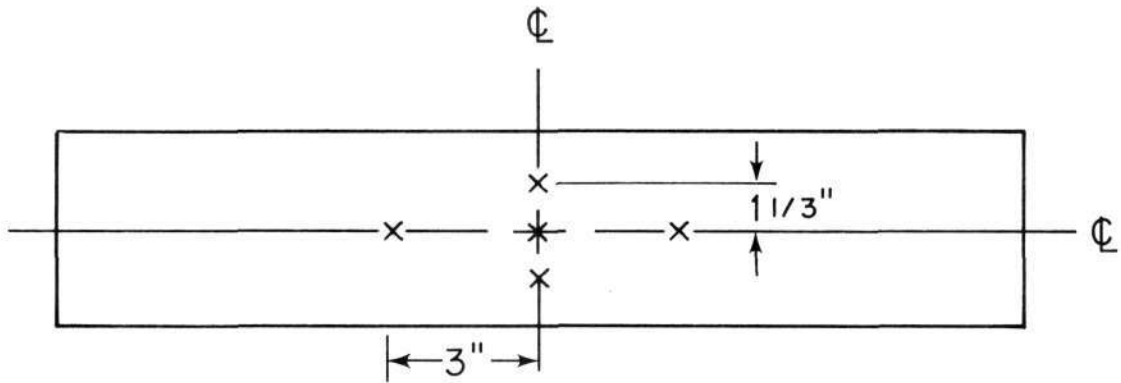


Figure 3-3 Spacing of plate thermocouples

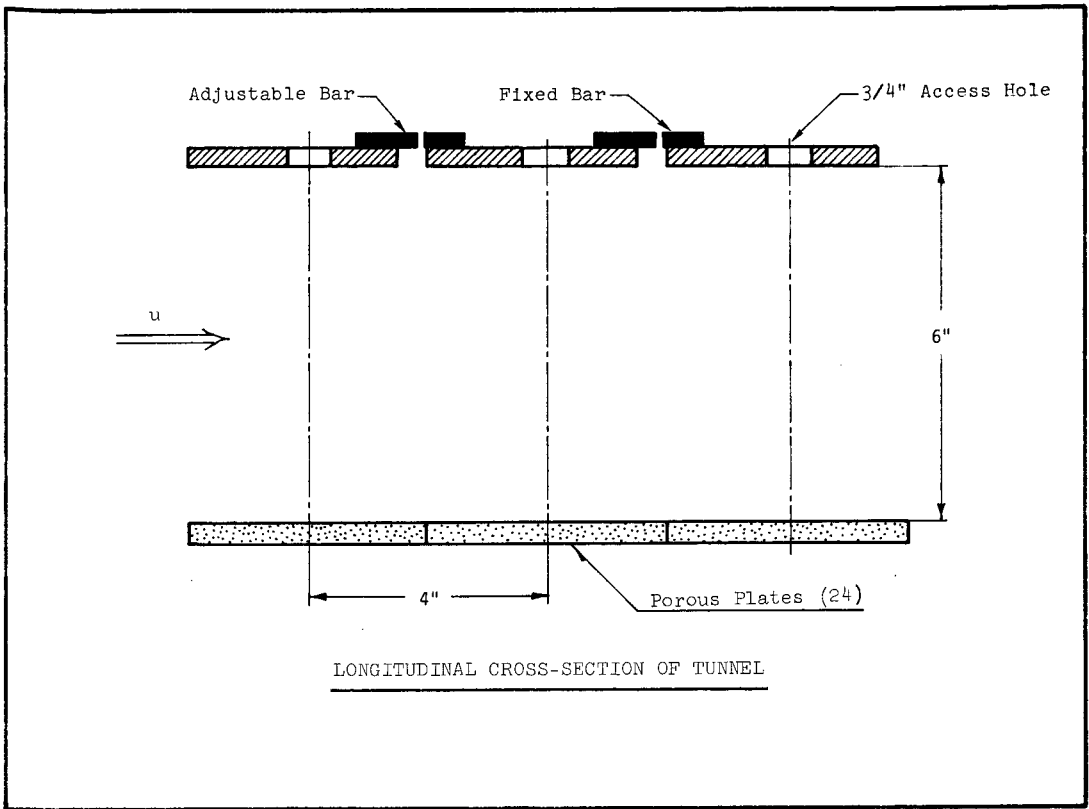


Figure 3-4 Longitudinal cross section of tunnel test section

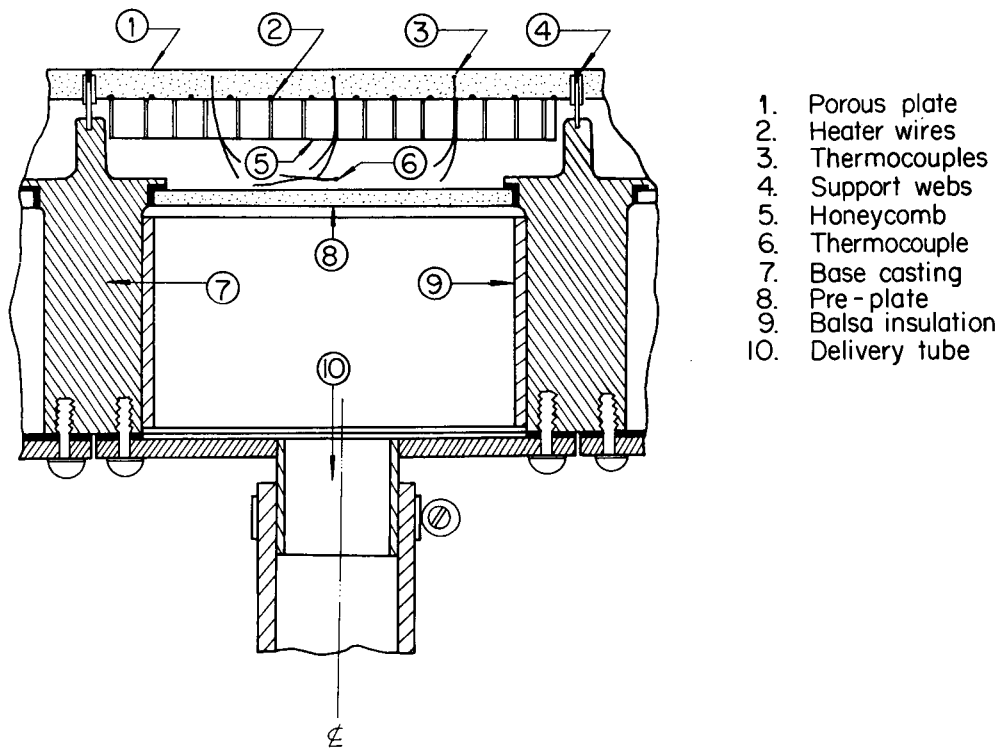


Figure 3-5 Cross section view of typical compartment

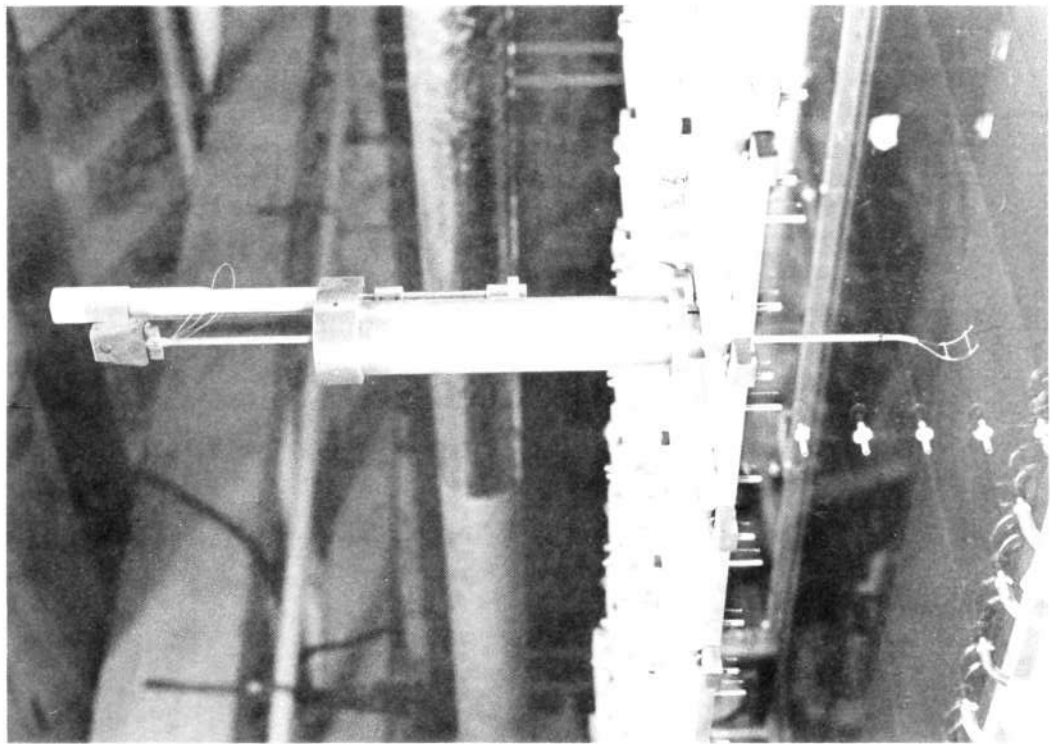
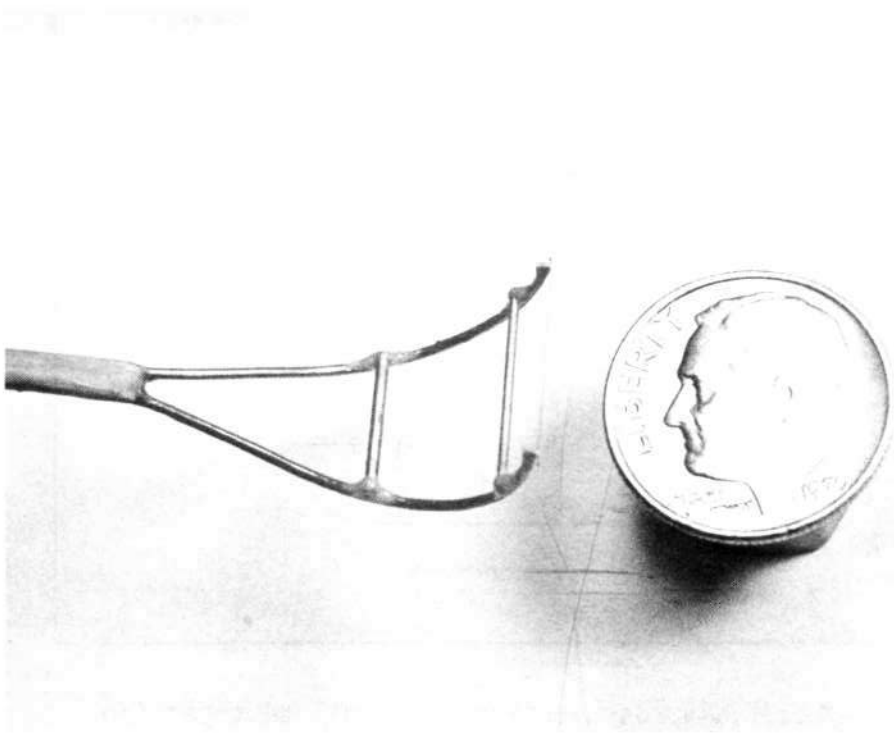


Figure 3-6 Photograph of traversing mechanism and temperature probe

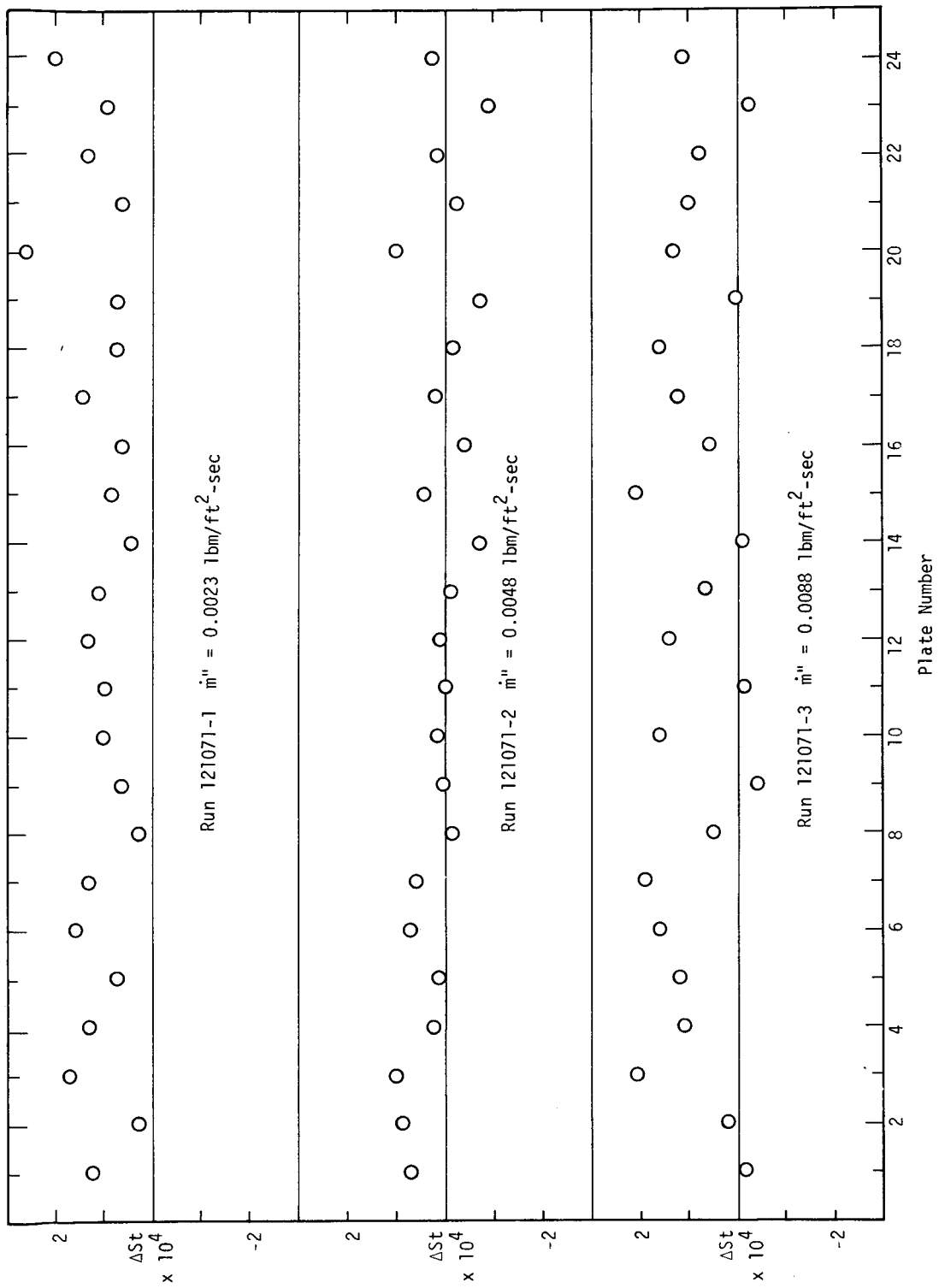


Figure 3-7 Transpiration energy balances for blowing mode

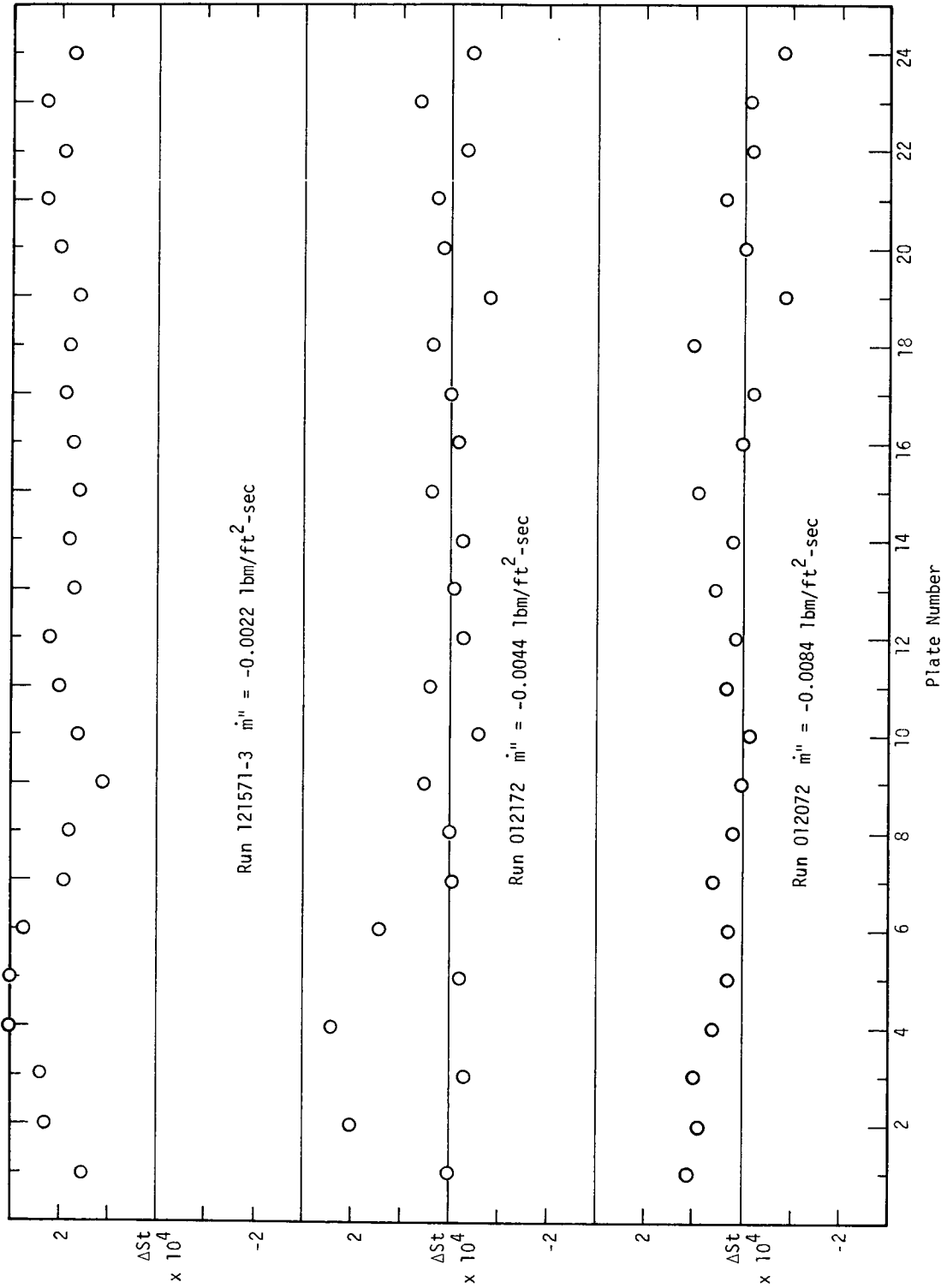


Figure 3-8 Transpiration energy balances for suction mode

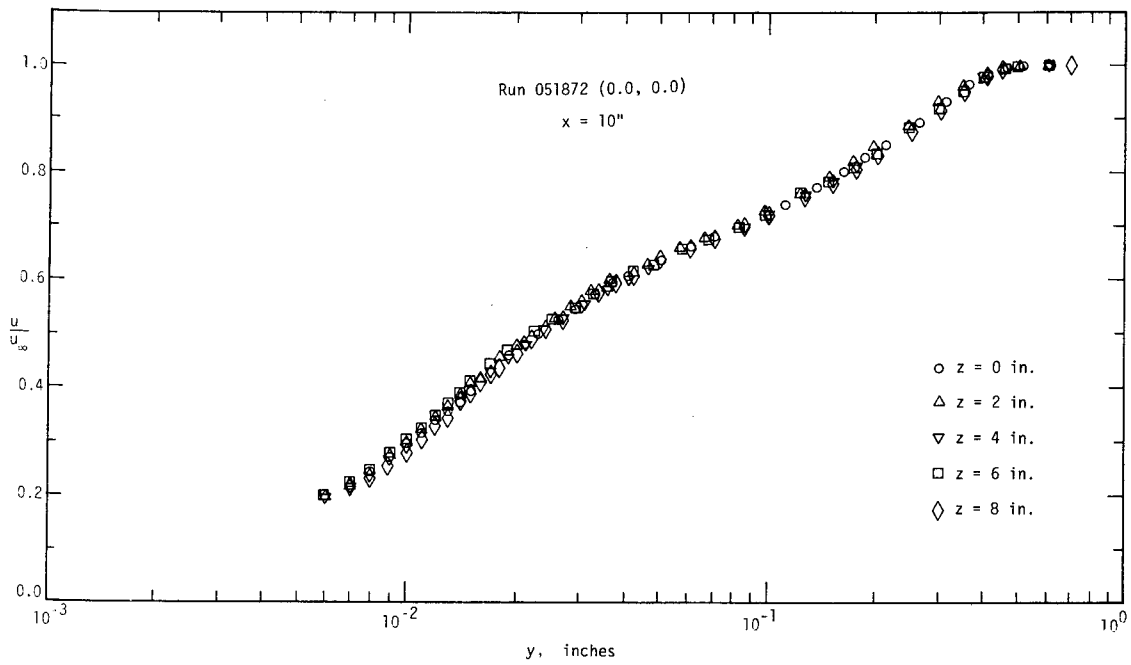


Figure 3-9 Transverse velocity profiles, $z > 0$, $x = 10$ inches

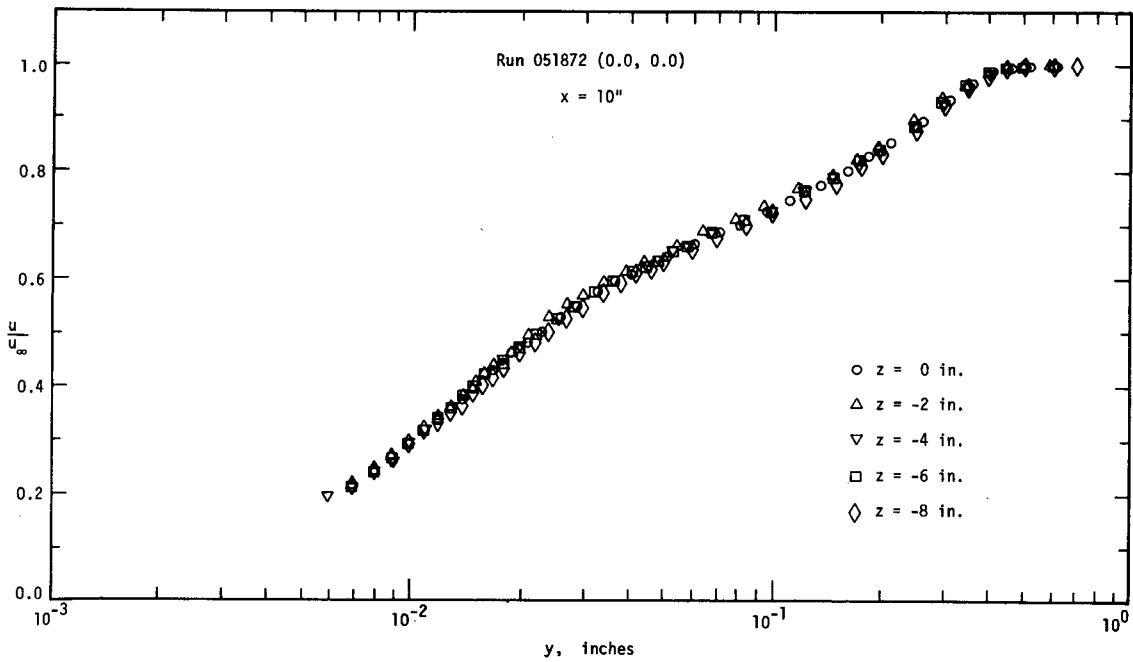


Figure 3-10 Transverse velocity profiles, $z < 0$, $x = 10$ inches

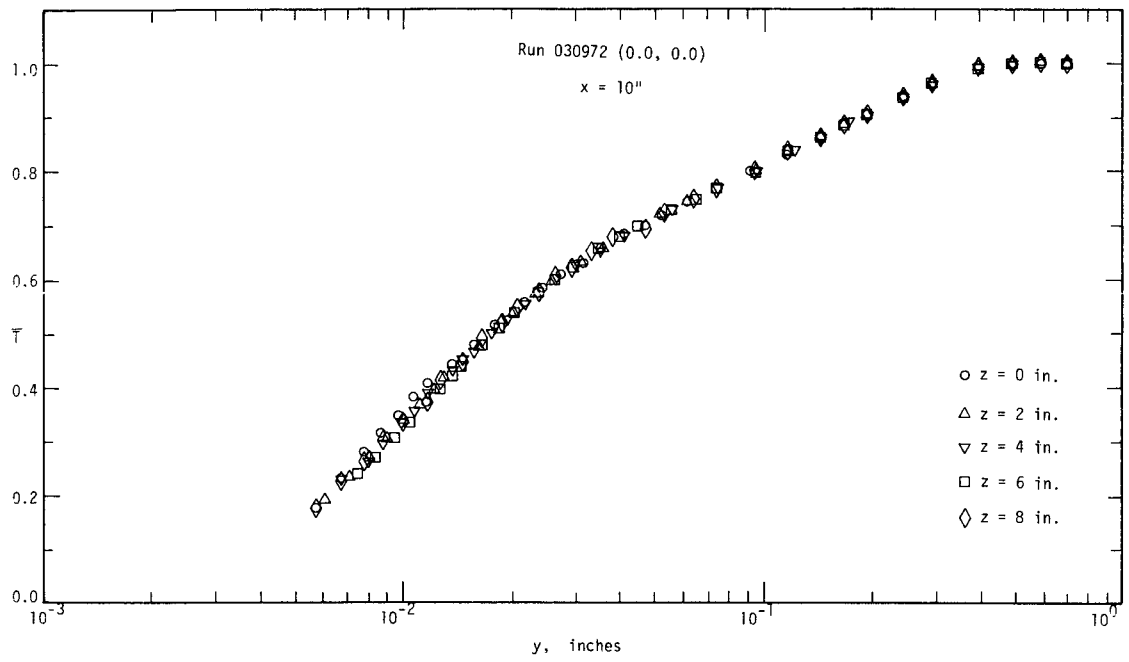


Figure 3-11 Transverse temperature profiles, $z > 0$, $x = 10$ inches

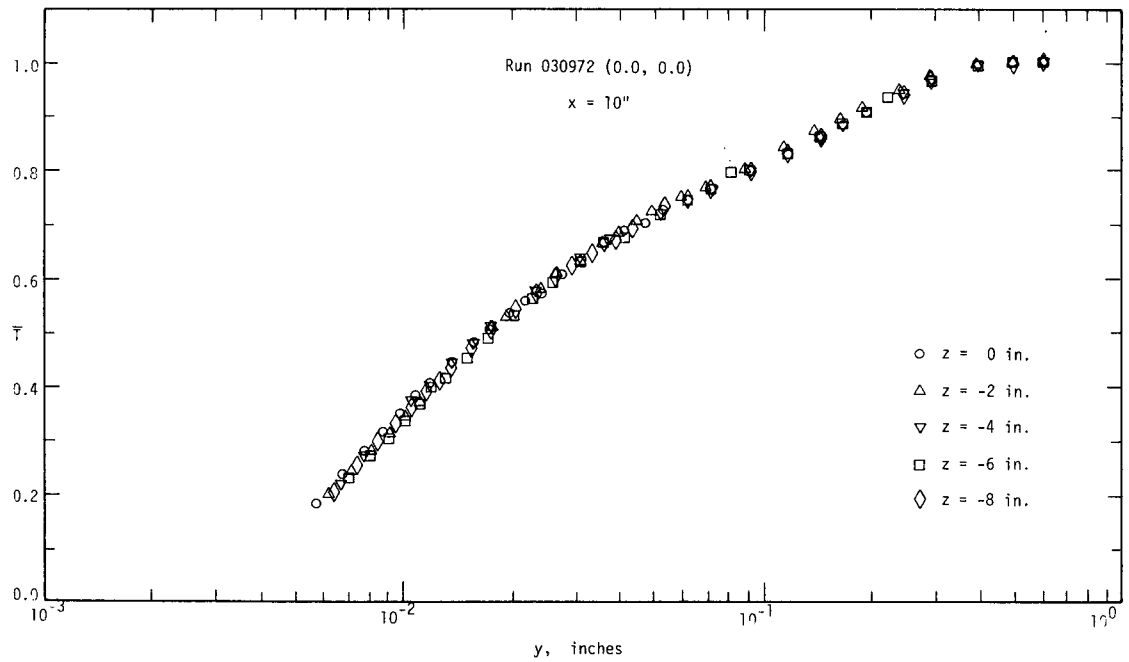


Figure 3-12 Transverse temperature profiles, $z < 0$, $x = 10$ inches

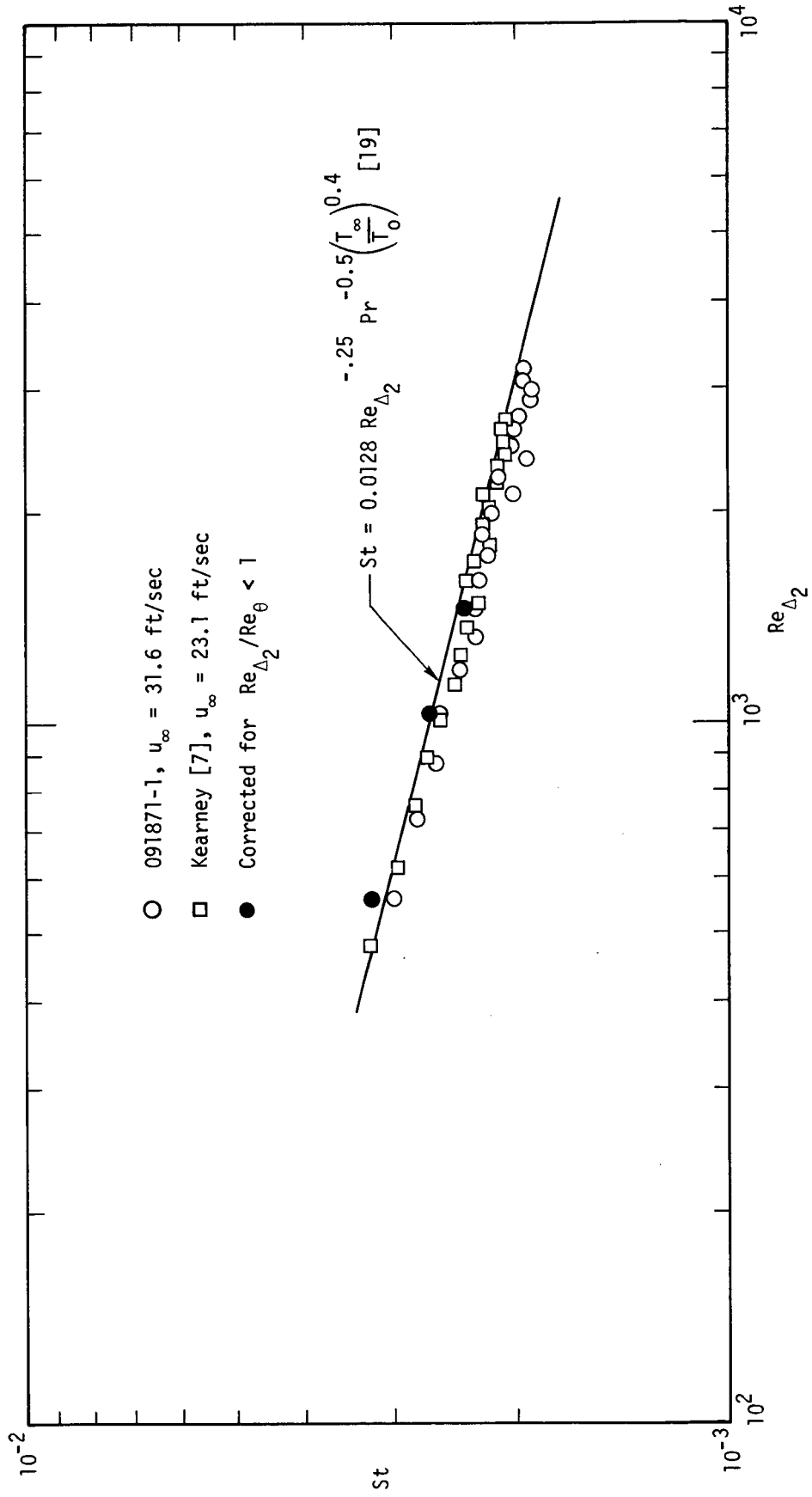


Figure 3-13 Zero pressure gradient, zero transpiration Stanton number data

CHAPTER 4

PRESENTATION OF EXPERIMENTAL STANTON NUMBER DATA

In this study, a total of 15 different combinations of pressure gradient and transpiration boundary conditions were investigated experimentally. The various boundary conditions will be divided into three categories: (1) no transpiration, (2) constant F with $m = -0.15$, and (3) constant $B_h \triangleq F/St$ with $m = -0.15$. Strictly speaking, the zero transpiration runs have constant $B_h = 0$ but they will still be treated as a separate case. The assumptions made in Section 2.5 as to how one would generate a constant B_h flow will also be verified.

For a given set of boundary conditions, the Stanton number data were taken twice; once before the temperature profiles were taken and once after. This provides a check on the repeatability of the data. In this chapter, only the first run will be presented. By checking the Stanton number data tabulation in CHAPTER 9, one can verify that the repeatability of the data was quite good. Using the methods of Kline [33] and the computer program of Kearney [7], the Stanton number uncertainty was estimated to be within 0.0001 Stanton number units.

4.1 Stanton Numbers for No Transpiration Flows

Figure 4-1 shows the influence of pressure gradient on the Stanton number for no transpiration. Within the uncertainty of the data, the two adverse pressure gradient flows have the same $St = f(Re_{\Delta_2})$ relationship as the zero pressure gradient. In contrast, the skin friction data of Andersen [9] for the same three flows shows that increasing adverse pressure gradient causes a decrease in skin friction for a given value of momentum thickness Reynolds number. This indicates that the Reynolds analogy between heat and momentum transfer is definitely not valid for adverse pressure gradient flows.

If the Stanton number data is plotted as a function of x , the streamwise distance, increasing adverse pressure gradient causes an increase in Stanton number for a given value of x . The enthalpy

thickness Reynolds number decreases with increasing adverse pressure gradient, for a given value of x . For skin friction, adverse pressure gradient yields the opposite trend.

Even though the data in Figure 4-1 indicates no influence of adverse pressure gradient (within the uncertainty of the data), it is felt that a slight increase in Stanton number actually does occur. This was concluded by least-square curve-fitting St vs Re_{Δ_2} in the form

$$St = a Re_{\Delta_2}^b \quad (4-1)$$

and evaluating the curve fit. The curve fit coefficients are tabulated in Table 4-1.

m	a	b
0.0	0.0144	-0.25
-0.15	0.0147	-0.25
-0.20	0.0161	-0.26

Table 4-1: Curve fit coefficients for non-transpired flows

4.2 Constant F Flows, $m = -0.15$

The Stanton number data for all of the constant F boundary conditions with $m = -0.15$ is shown in Figure 4-2. As was expected, blowing decreases the Stanton number while suction increases the Stanton number.

4.3 Constant B_h Flows, $m = -0.15$, $m_F = -0.17$

The Stanton number data for the constant B_h boundary conditions is shown in Figure 4-3. The constant B_h flows show the same trends with blowing and suction as the constant F flows. Note that the St vs Re_{Δ_2} curves for the constant B_h flows are approximately parallel.

As stated previously, two sets of Stanton data were taken for each set of boundary conditions. A "best interpretation" of these two runs was obtained by least-square curve-fitting the two runs together by an equation of the form

$$St = a(x + b)^c \quad (4-2)$$

and evaluating the resulting curve-fit at the x-locations corresponding to the plate centerline. The results for the $m = -0.15$ data are shown in Figure 4-4. The constant F runs (solid curve) have the nominal value of F on the left of each curve; the constant B_h runs have the nominal value of B_h on the right of each curve. The data tabulated under the heading STNA in CHAPTER 9 was obtained from (4-2).

In Section 2.5, it was assumed that the ratio of Stanton number to the non-transpired Stanton number, for a given pressure gradient and enthalpy thickness Reynolds number, is a unique function of the transpiration parameter $B_h = F/St$. This assumption was expressed in the form

$$\left(\frac{St}{St_0} \right)_{m, Re_{\Delta 2}} = f_1(B_h) \quad (4-3)$$

All of the Stanton number data was plotted in the form of (4-3) and is shown in Figure 4-5. This figure not only verifies (4-3) for the constant B_h flows, but it also shows that if m varies slowly (as was the case for the $F = \text{constant}$ runs) the Stanton number ratio is a unique function of B_h , for a given pressure gradient. This fact might prove useful in an integral method for predicting heat transfer.

4.4 Comparison of Adverse Pressure Gradient Stanton Numbers With Zero Pressure Gradient Data

Since most people are more familiar with Stanton number data for zero pressure gradient, it will be useful to compare the adverse pressure gradient data of this study with the earlier zero pressure gradient data of Moffat [2]. Figure 4-6 compares selected constant F runs of this study with the corresponding data of Moffat. The zero pressure gradient, no transpiration data is shown in order to have a reference. (The $(-0.15, 0.000)$ flow could also have been shown but the data in Figure 4-1 indicates that it is extremely close to the $(0.00, 0.000)$ flow). The data sets are arranged in the order of increasing F . For small values of $|F|$

(blowing and suction), the mild adverse pressure gradient of this study does not appreciably alter the $St = f(Re_{\Delta_2})$ relationship, when compared to the zero pressure gradient data. For the larger values of $|F|$, the effect of adverse pressure gradient is to decrease St for a given Re_{Δ_2} . The run where the pressure gradient has the most effect was the strongest blowing rate. Part of this difference is possibly due to the uncertainty in the data. It was estimated that the uncertainty was ± 0.0001 Stanton number units. In this case, the uncertainty band for each of the two runs is almost overlapping.

4.5 Asymptotic Suction Layer for $u_\infty \sim x^m$ Flows

The constant property, constant wall temperature energy integral equation can be written as

$$\frac{d\Delta_2}{dx} = St + F - m \frac{\Delta_2}{x-x_0}, \quad m < 0 \quad (4-5)$$

The term $\Delta_2/(x-x_0)$ should approach zero for large values of x because Δ_2 is approaching a constant value. Therefore, we conclude that for the type of adverse pressure gradients of this study, an asymptotic suction layer exists where $St = -F$. However, it should be emphasized that even though both zero and adverse pressure gradient have the same asymptotic suction limit for a given constant F , Stanton number as a function of streamwise distance x will be quite different for the two pressure gradients.

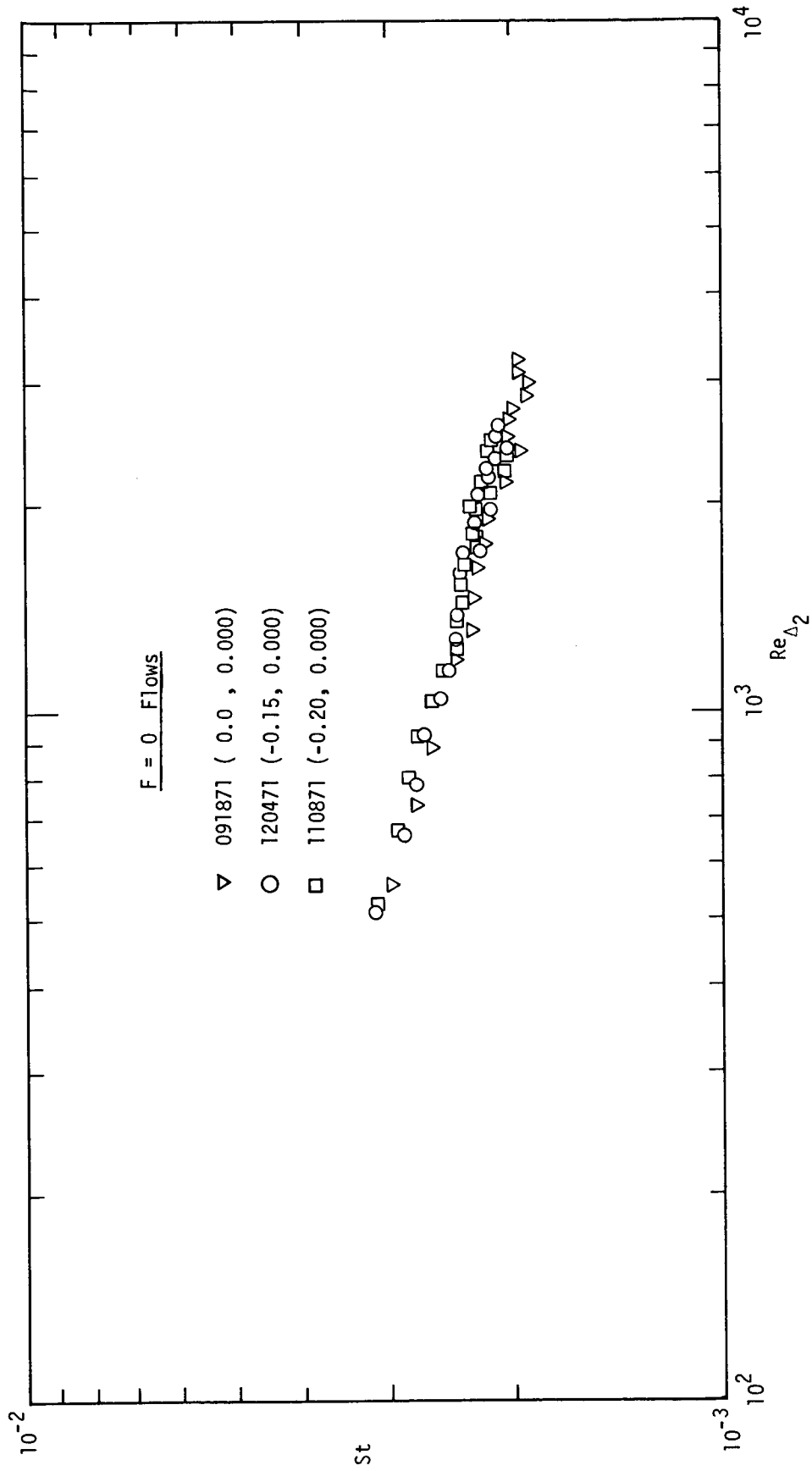


Figure 4-1 Influence of pressure gradient with zero transpiration on Stanton number

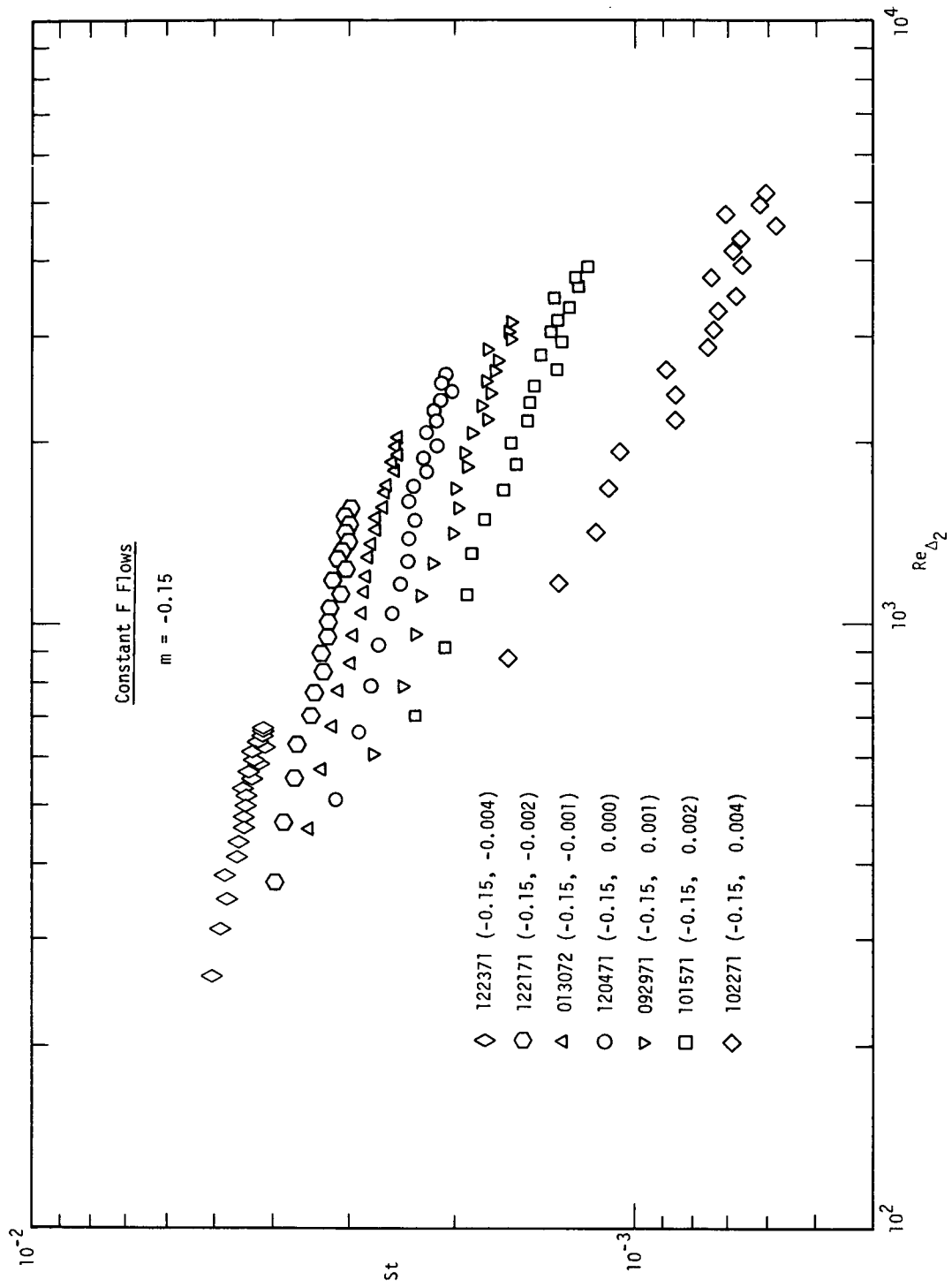


Figure 4-2 Stanton number data for $m = -0.15$ and constant F boundary conditions

5

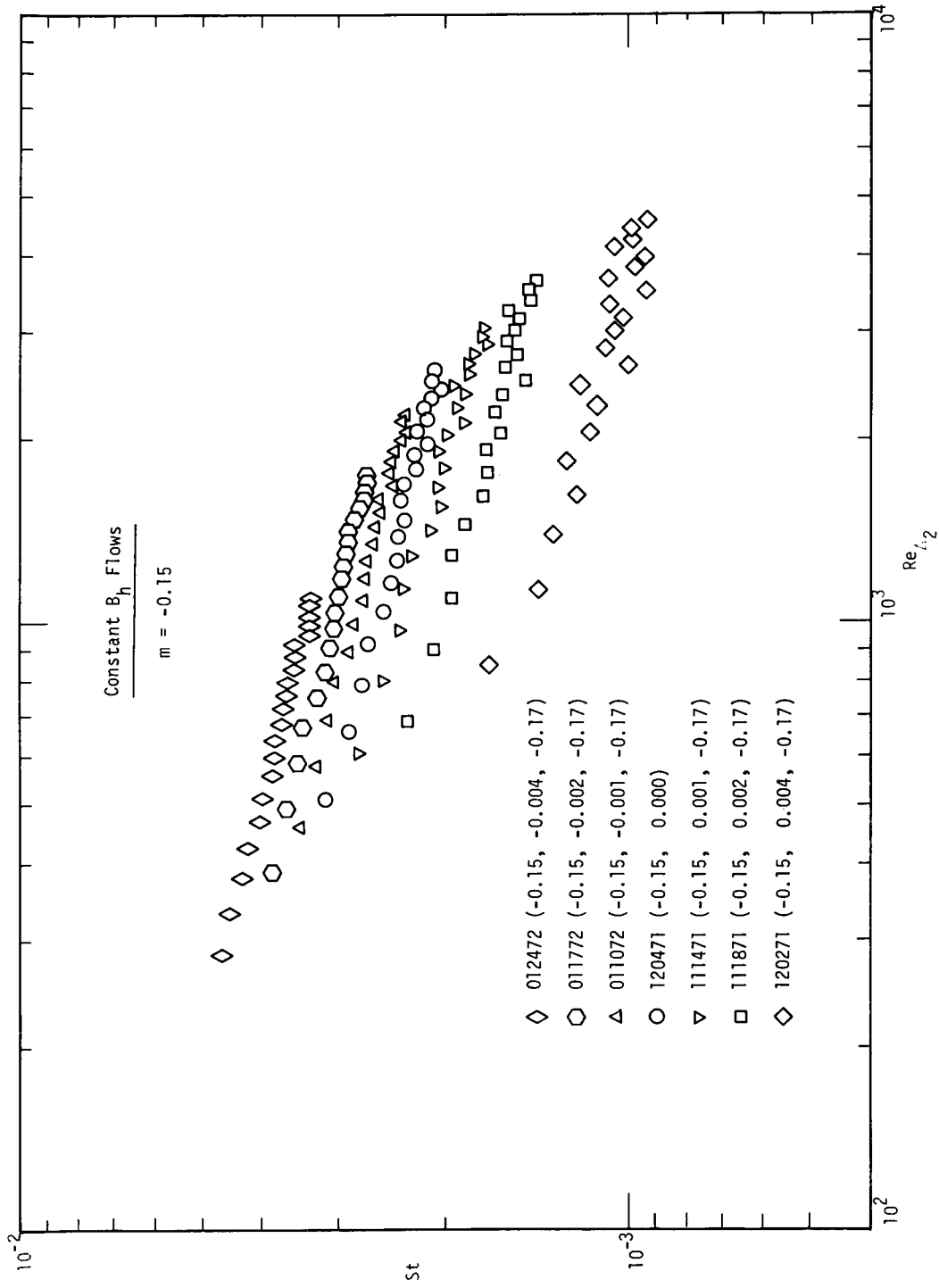


Figure 4-3 Stanton number data for $m = -0.15$ and constant B_h boundary conditions

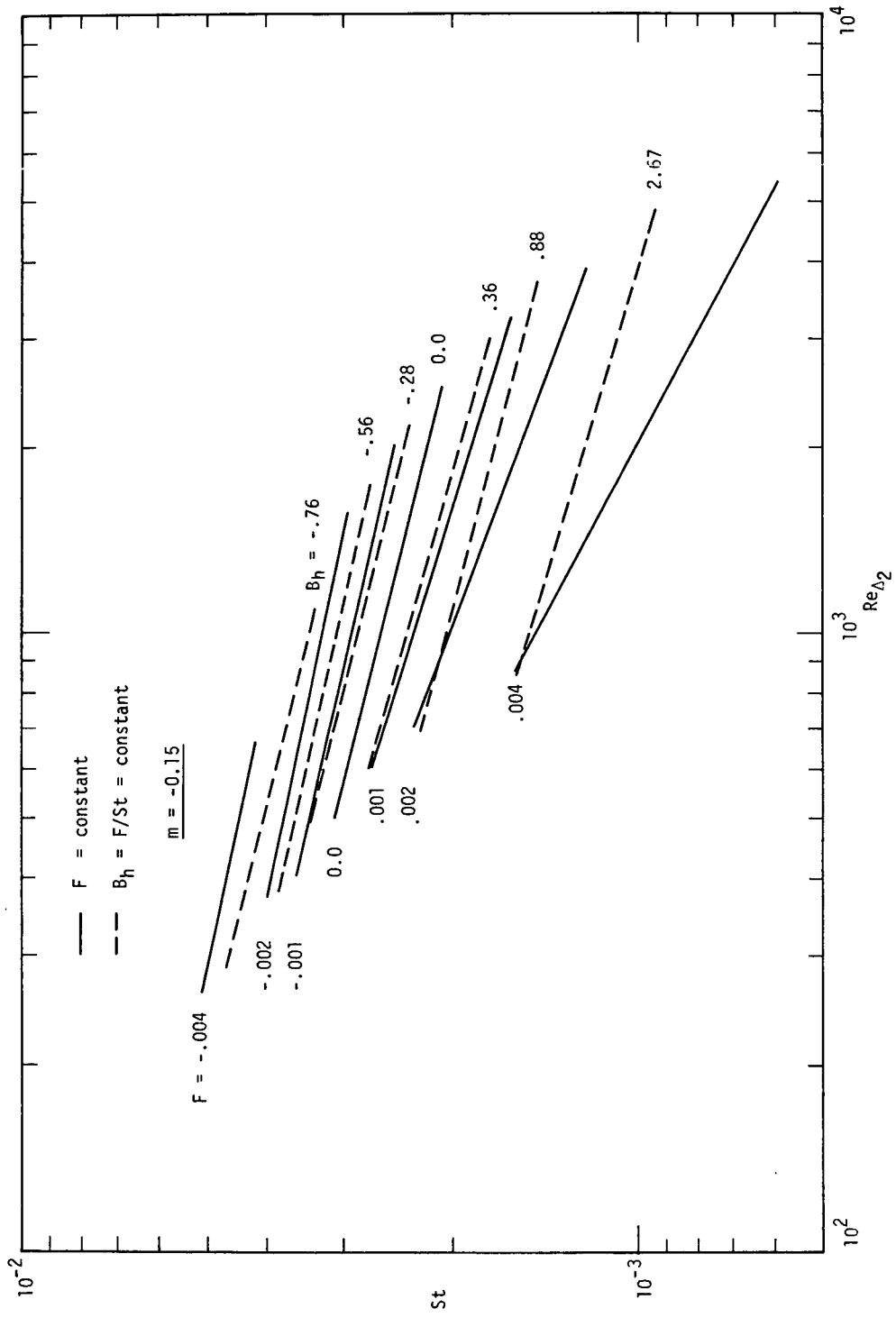


Figure 4-4 Summary of all Stanton number data for $m = -0.15$

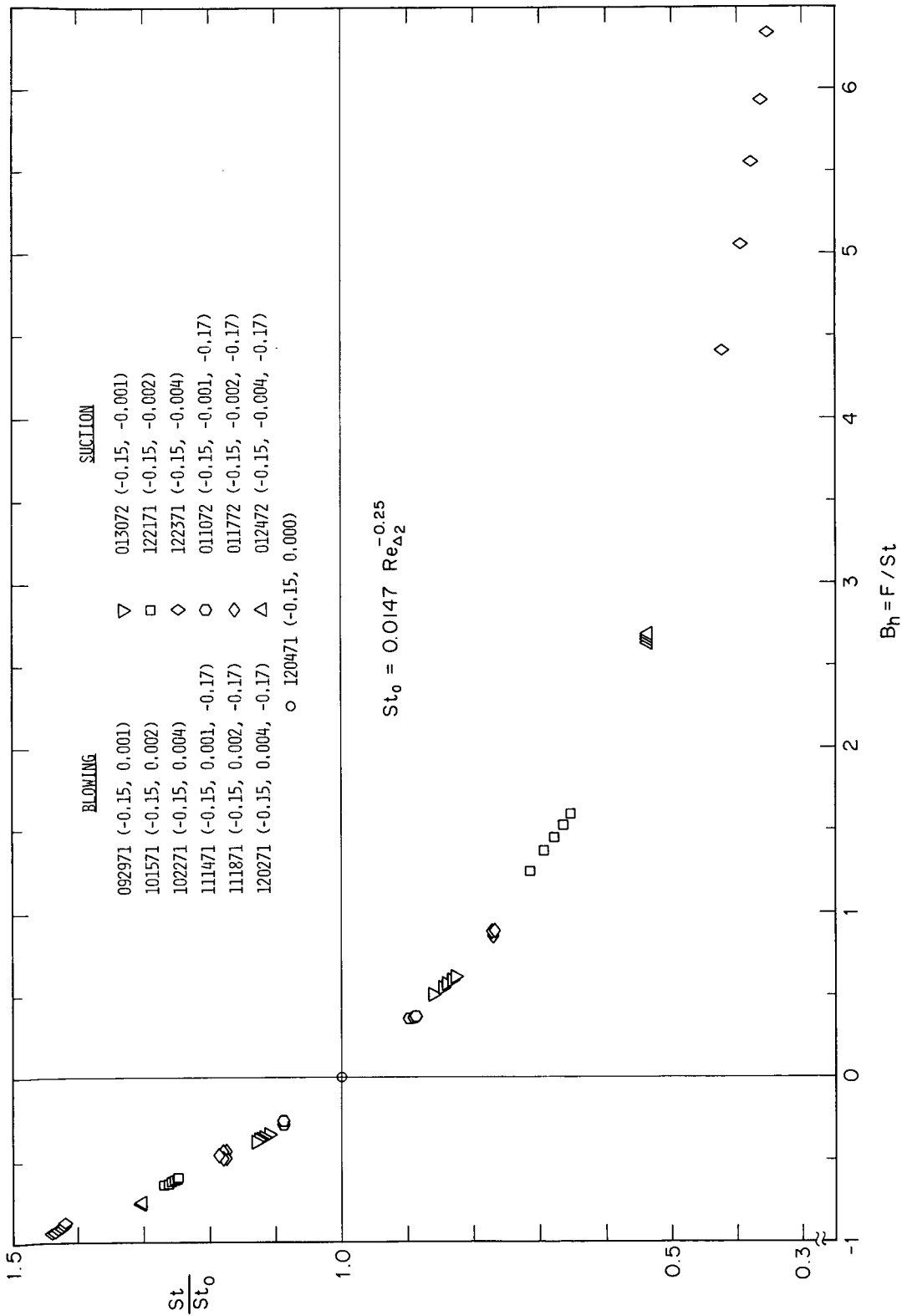


Figure 4-5 Stanton number ratio for all $m = -0.15$ flows

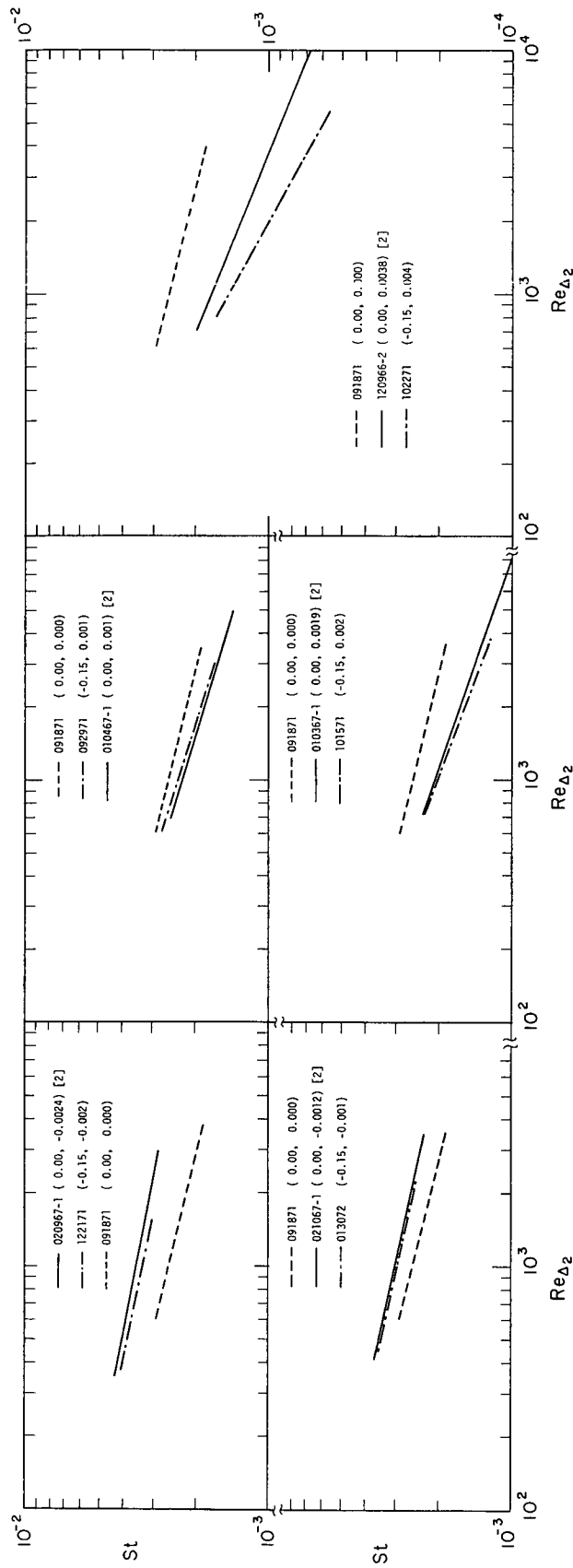


Figure 4-6 Comparison of selected adverse pressure gradient runs with zero pressure gradient data of Moffat [2]

CHAPTER 5

MEAN TEMPERATURE PROFILE DATA

For each of the 15 different runs listed in Table 2-2, mean temperature profiles were measured using the boundary layer temperature probe described in Section 3.7. A total of 132 temperature profiles are reported in this study with each profile consisting of 30-45 data points. With this large a number of temperature profiles, only those profiles that bring out a significant point will be presented. All of the temperature profiles of this study are tabulated in CHAPTER 9. The estimated uncertainty in the profile temperature was 0.2°F .

5.1 Mean Temperature Profiles in Wall Coordinates

It has been well established that a "law of the wall" exists for the velocity boundary layer for adverse pressure gradients and no transpiration. However, the same is not true of the thermal boundary layer. This fact is shown by the data in Figure 5-1. Although all of the temperature profiles in Figure 5-1 exhibit a logarithmic region, the slope of this region decreases with increasing adverse pressure gradient. This fact was also reported by Perry [12]. Due to the fact that the skin friction is markedly decreased by adverse pressure gradients while the Stanton number is essentially unaffected, it is apparent that a "temperature law of the wall" should not exist. The data in Figure 5-1 also indicates that any type of "Reynolds analogy" between skin friction and Stanton number for adverse pressure gradient flows is definitely not valid.

From the definition of T^+ and y^+ , both depend on $\sqrt{C_f/2}$. It is not obvious that skin friction should appear in the temperature and distance scales, at least very near the wall. For momentum transfer, it is well accepted that u^+ is a function of y^+ , for no transpiration and close to the wall. The wall variables u^+ and y^+ can be written as (for constant property flow)

$$u^+ = \frac{u}{u_\infty} \frac{1}{\sqrt{C_f/2}}, \quad y^+ = \frac{y u_\infty}{\nu} \sqrt{C_f/2} \quad (5-1)$$

For heat transfer, $(T-T_0)/(T_\infty-T_0)$ is analogous to u/u_∞ and St is analogous to $C_f/2$. Using (5-1) as a guide and the above analogies, let us define new temperature and distance variables as

$$T^* = \bar{T} \cdot \frac{1}{\sqrt{St}}, \quad y^* = \frac{y u_\infty}{\nu} \sqrt{St} \quad (5-2)$$

In order to account for variable density flow, we should define T^* and y^* as

$$T^* = \bar{T} \frac{1}{\sqrt{St \rho_\infty/\rho_0}} \quad (5-3)$$

and

$$y^* = \frac{y u_\infty}{\nu} \sqrt{\frac{\rho_\infty}{\rho_0} St} \quad (5-4)$$

Figure 5-2 presents T^* vs y^* for the three no transpiration runs of this study. On comparing the data in Figure 5-2 with the (T^+, y^+) data of Figure 5-1 for the same runs, it appears that (T^*, y^*) collapse the inner part ($y^* < 20$) of the boundary layer much better than (T^+, y^+) , and does a fair job at collapsing the logarithmic region.

The (T^*, y^*) variables are also suggested by the laminar sublayer equation for temperature. For low velocity, constant property flow, this sublayer equation is

$$T^+ = Pr y^+ \quad (5-5)$$

From definitions, (5-5) can be written as

$$\bar{T} \frac{\sqrt{C_f/2}}{St} = Pr \frac{y u_\infty}{\nu} \sqrt{C_f/2} \quad (5-6)$$

Since $\sqrt{C_f/2}$ appears on both sides of (5-6), it can be cancelled out. Hence, (5-6) becomes

$$\bar{T} \frac{1}{\sqrt{St}} = Pr \frac{y u_\infty}{\nu} \sqrt{St} \quad (5-7)$$

or,

$$T^* = Pr y^* \quad (5-8)$$

We conclude that the form of the laminar sublayer equation is the same for both (T^+, y^+) and (T^*, y^*) .

Figure 5-3 shows the influence of transpiration on the mean temperature profiles for $m = -0.15$. From this figure, it can be concluded that blowing produces a large wake while suction suppresses the wake. These same conclusions were also drawn by Whitten [3] in his constant free stream velocity study.

5.2 Mean Temperature Profiles in Outer Region Coordinates

The coordinates chosen to present the temperature profiles in the outer part of the boundary layer are $-I_d^+$ vs y/Δ_3 , where I_d^+ and Δ_3 are defined by Equations (2-6a) and (2-7), respectively. Figure 5-4 presents the defect enthalpy profile for the zero pressure gradient, no transpiration run. Only the profiles at the $x = 34, 58,$ and 82 inch locations are presented; profiles at other x locations are tabulated in CHAPTER 9. For $x < 34$ inches, the flow is not in equilibrium because the momentum boundary layer originates upstream of the thermal boundary layer. In this figure, $y/\Delta = 0.1$ corresponds approximately to $y/\Delta_3 = 0.03$. Hence, the outer 90% of the thermal boundary layer is similar in terms of defect coordinates; it is apparent that the inner 10% of the thermal boundary layer is not similar in defect coordinates.

Figures 5-5 thru 5-8 show defect enthalpy profiles for other selected runs. Again, the outer 90% of the thermal boundary layer is similar in defect coordinates. However, the defect profile shape changes considerably from one run to the next.

5.3 Enthalpy Defect Profile Shape Factors

In Section 2.2, a defect enthalpy profile shape factor G_h was introduced and is formally defined by Equation (2-10). This shape factor G_h is directly analogous to the defect velocity shape factor introduced by Clauser [14]. Figure 5-9 shows the influence of pressure gradient with no transpiration on G_h . All three of the runs shown in Figure 5-9 approach a constant value of G_h for large values of x , and hence are equilibrium thermal layers. The primary reason that G_h varies for small values of x is that the momentum boundary layer originates upstream of the thermal boundary layer. The equilibrium flat plate value of G_h is approximately 5.75. The effect of increasing adverse pressure gradient is to decrease G_h . Andersen [9] reports the opposite effect of adverse pressure gradient on the defect velocity shape factor G_f .

Figure 5-10 shows the influence of transpiration on G_h for all of the $m = -0.15$ flows. Blowing increases G_h while suction decreases G_h . All of the constant B_h flows approach a constant value of G_h for large values of x . All of the constant F flows approach a constant value of G_h with the exception of the most extreme blowing run ($F = 0.004$). This indicates that if the transpiration rate m'' changes sufficiently slowly with x , then the outer part of the thermal boundary layer is able to respond sufficiently fast to maintain an equilibrium state.

5.4 Reynolds Number Ratio

As was pointed out earlier, the momentum boundary layer originates upstream of the thermal boundary layer. The effect of this different virtual origin is that the defect enthalpy shape factor G_h is different from what it would have been if the origin of both boundary layers had

been coincident. Another effect is that the enthalpy thickness Reynolds number is smaller than it would have been if the two origins were coincident. This latter effect is shown in Figure 5-11, where the enthalpy thickness Reynolds number has been normalized by the momentum thickness Reynolds number. This starting length effect is the most pronounced for the zero pressure gradient run because the asymptotic value of $Re_{\Delta_2}/Re_{\theta}$ is the largest of all the flows reported in this study. Using the zero pressure gradient case for a standard of comparison, one concludes that increasing adverse pressure gradient causes a decrease in the asymptotic Reynolds number ratio. This is due to the fact that increasing adverse pressure gradient causes a decrease in Re_{Δ_2} but an increase in Re_{θ} , for a given value of x . Figures 5-12 and 5-13 show the same data for the constant B_h and constant F flows respectively. Blowing decreases this Reynolds number ratio while suction increases it.

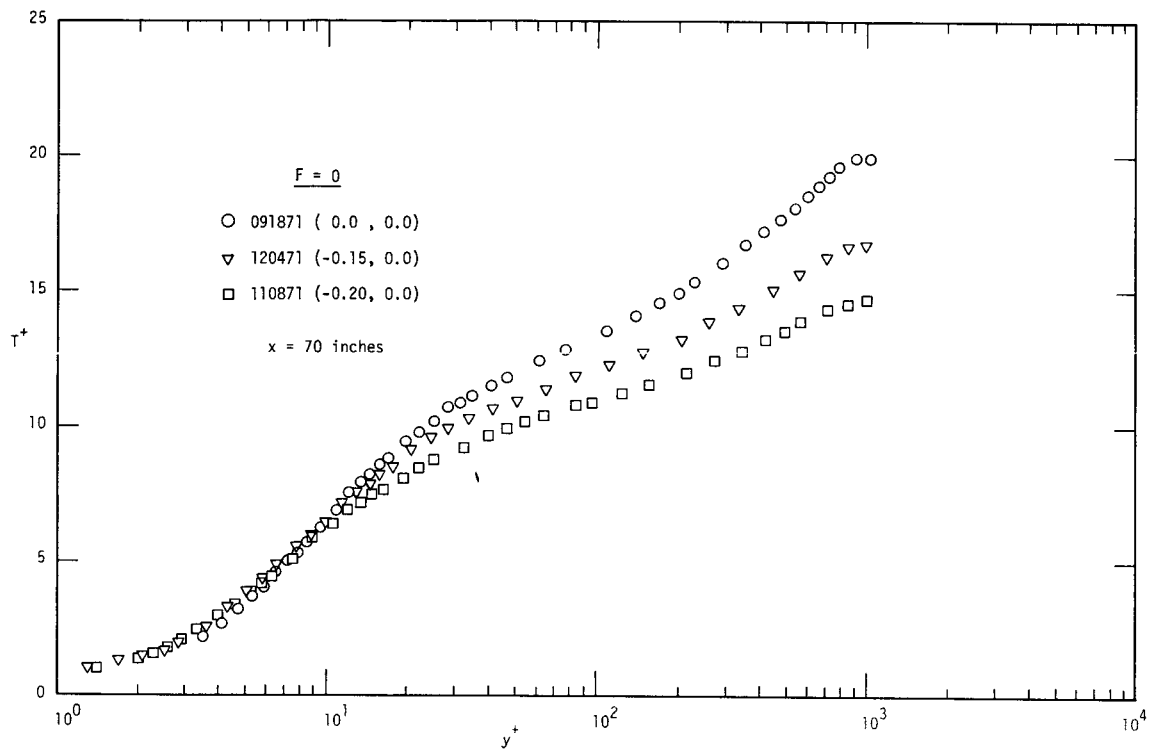


Figure 5-1 Influence of pressure gradient on non-dimensional temperature profiles, wall coordinates

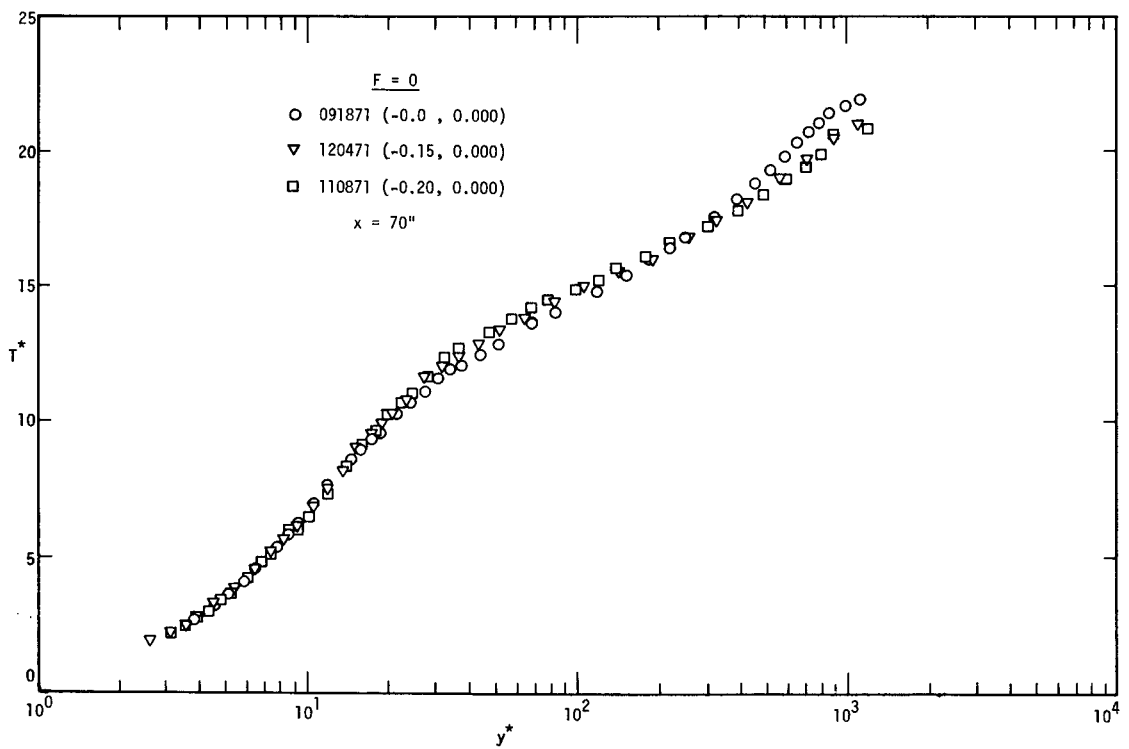


Figure 5-2 Influence of pressure gradient on non-dimensional temperature profiles, wall coordinates

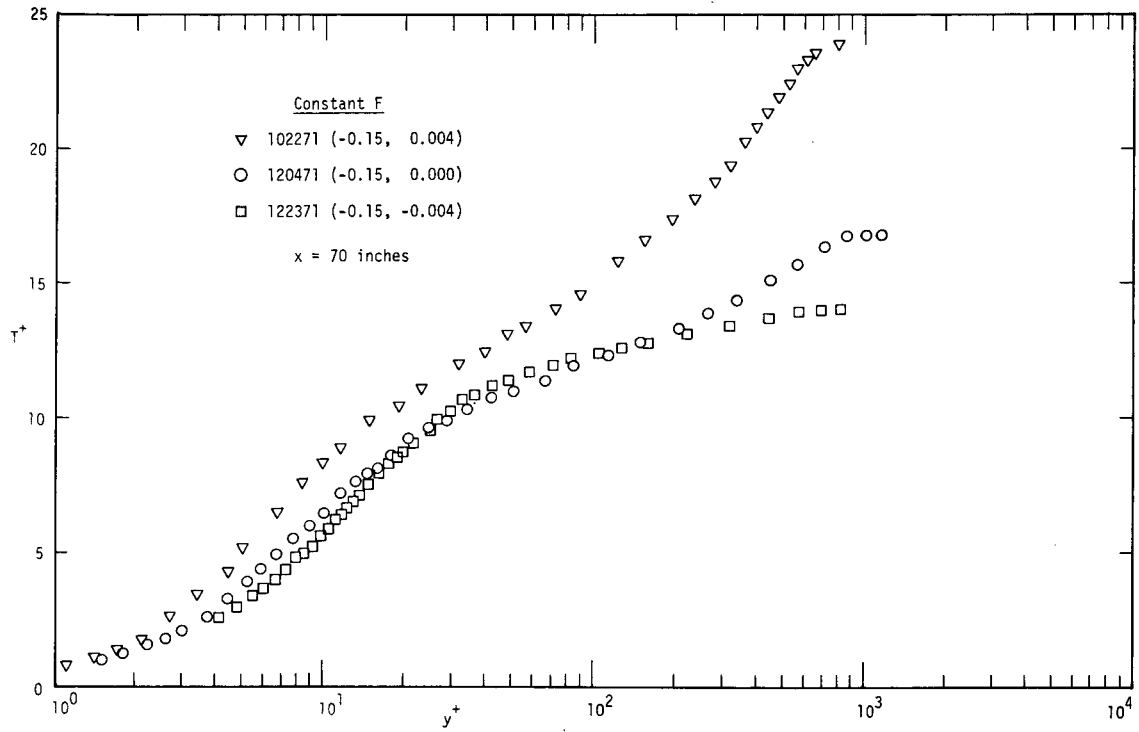


Figure 5-3 Influence of transpiration on non-dimensional temperature profiles, wall coordinates

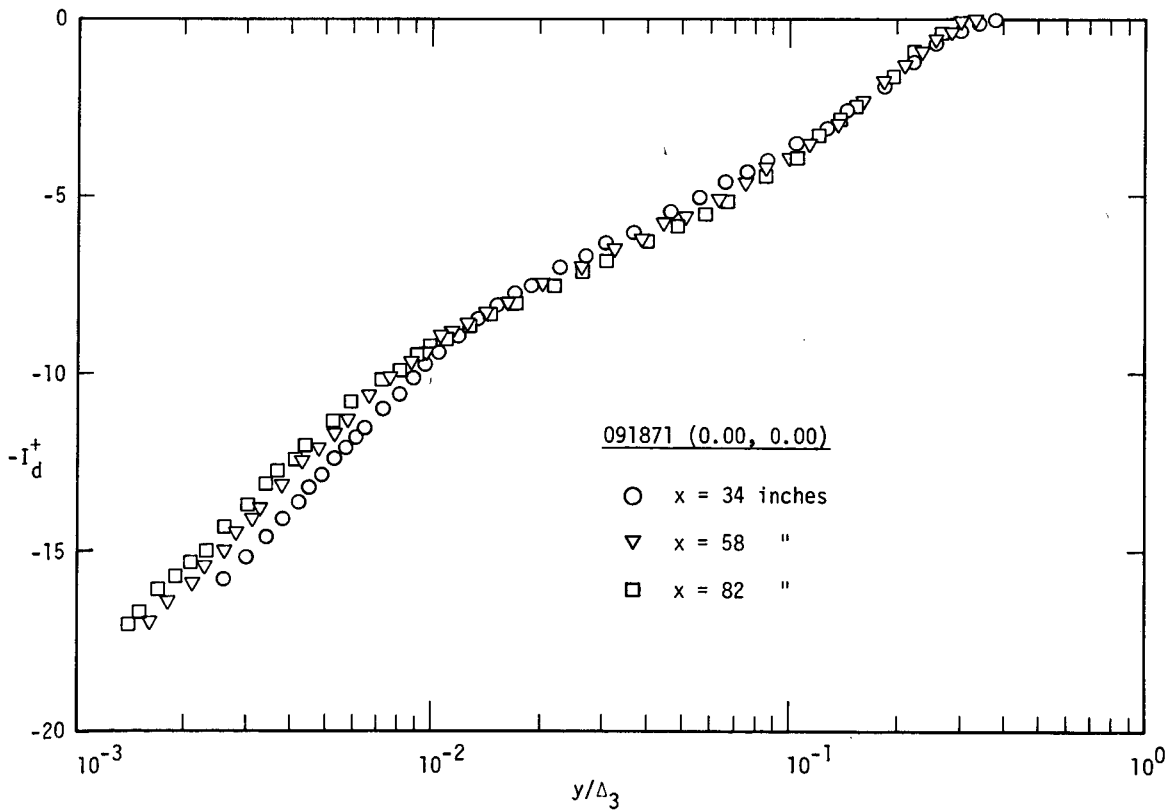


Figure 5-4 Defect enthalpy profiles, run 091871

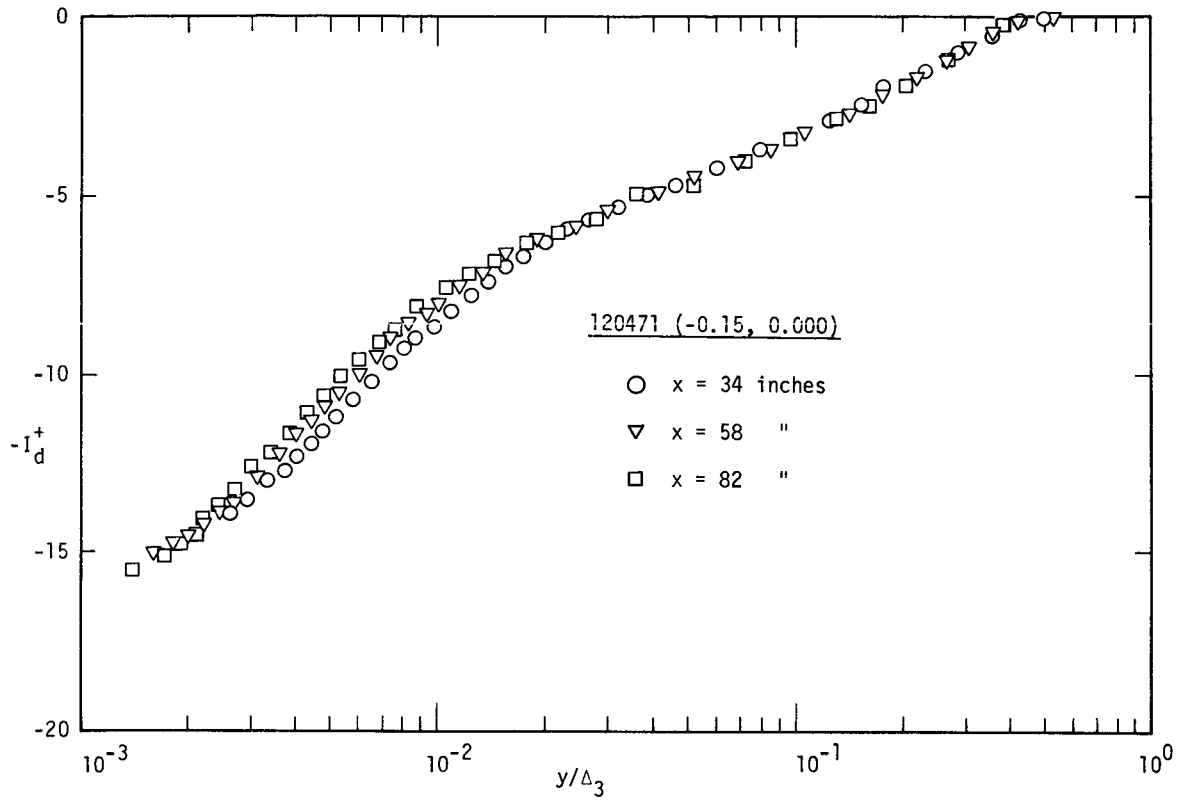


Figure 5-5 Defect enthalpy profiles, run 120471

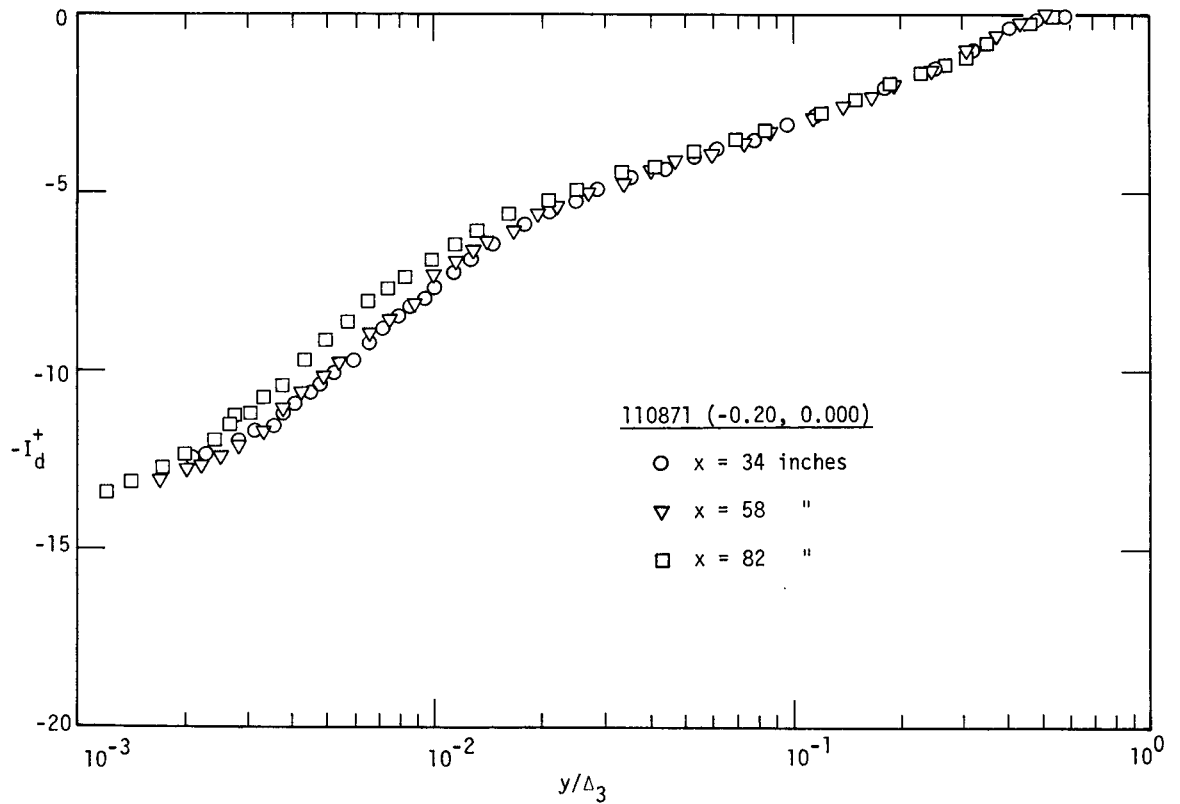


Figure 5-6 Defect enthalpy profiles, run 110871

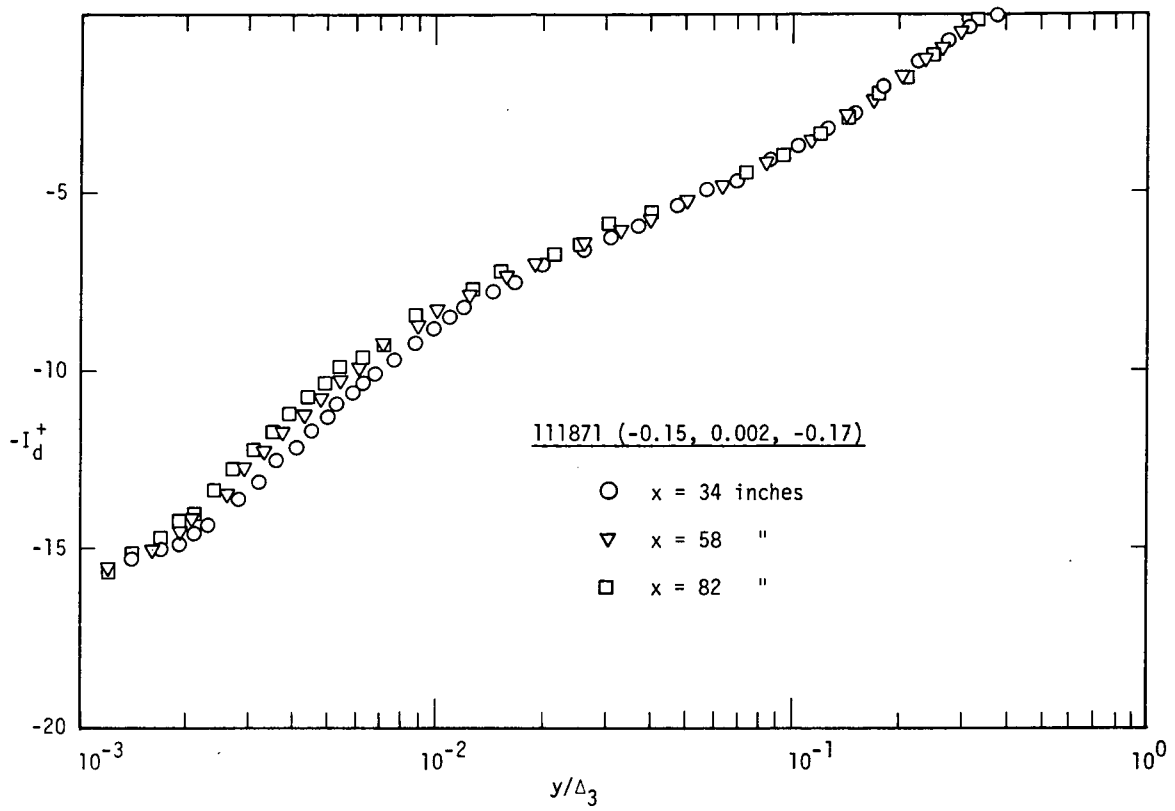


Figure 5-7 Defect enthalpy profiles, run 111871

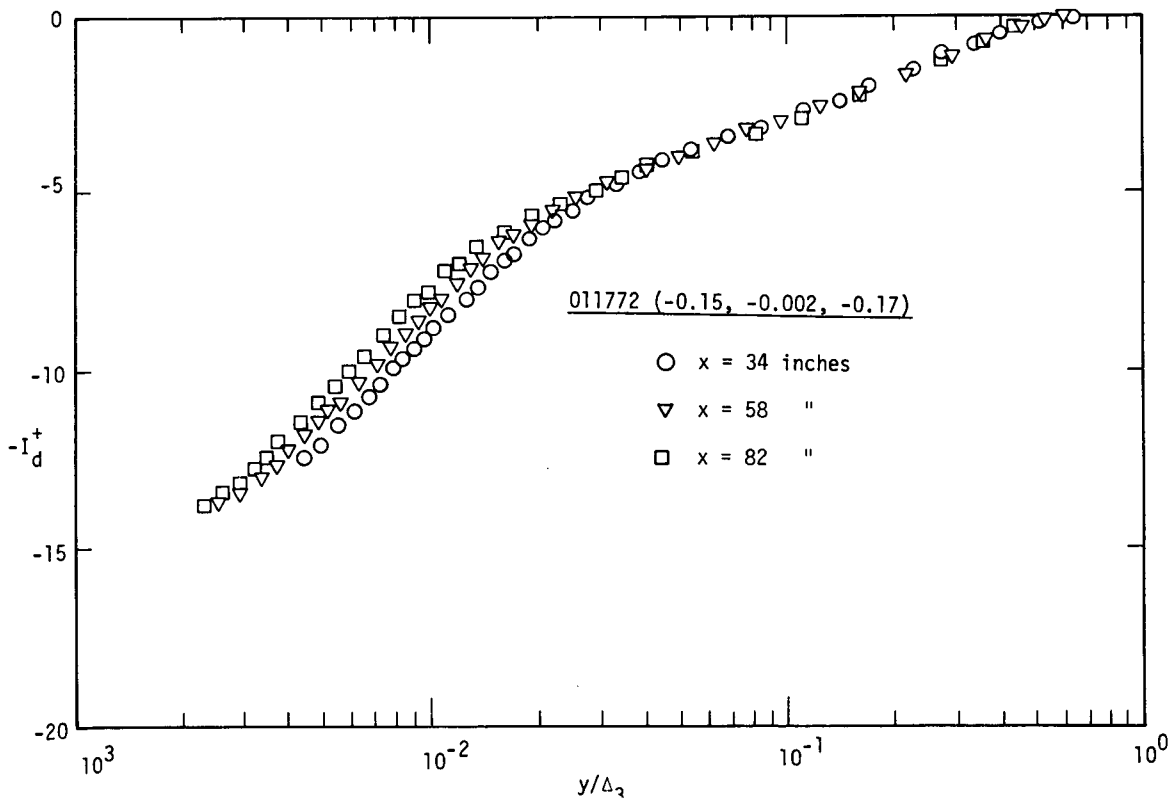


Figure 5-8 Defect enthalpy profiles, run 011772

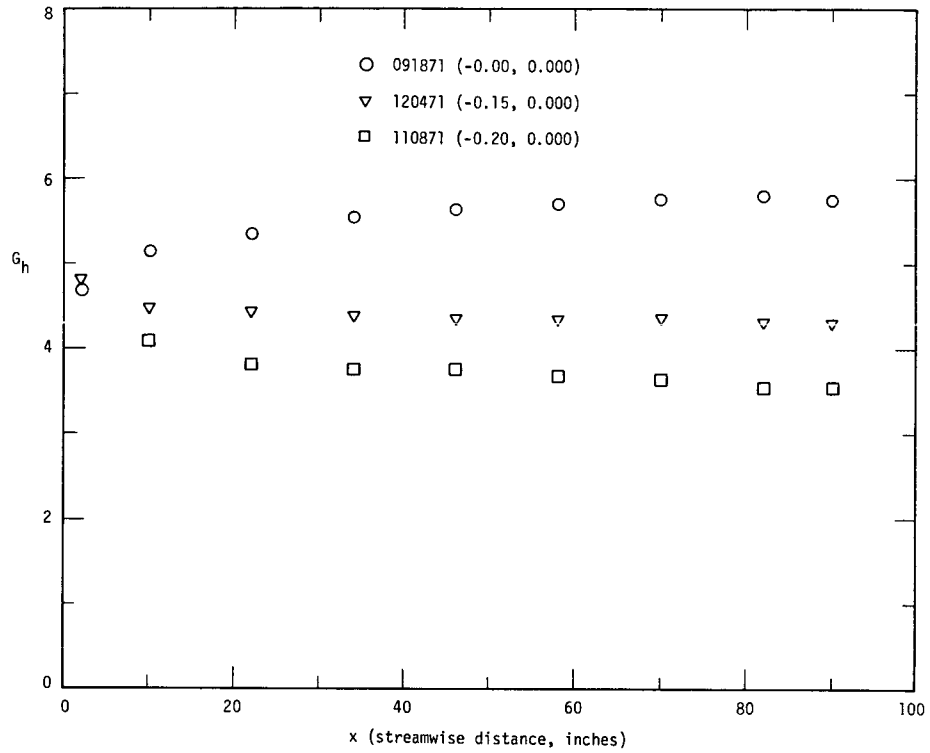


Figure 5-9 Influence of pressure gradient on defect enthalpy shape factor

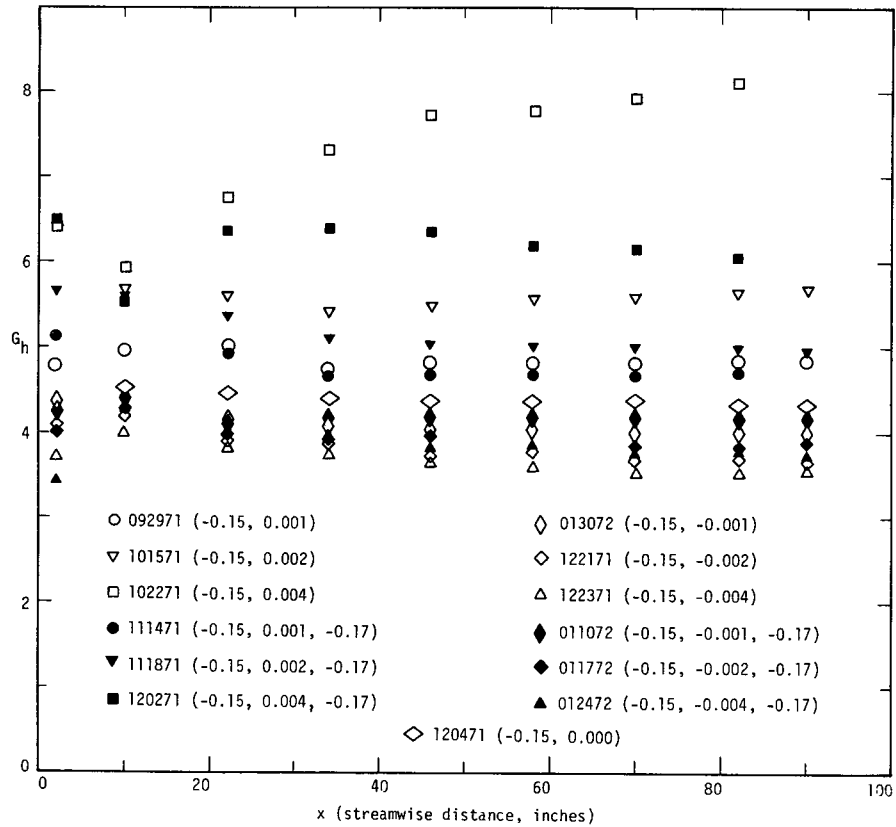


Figure 5-10 Influence of transpiration on defect enthalpy shape factor

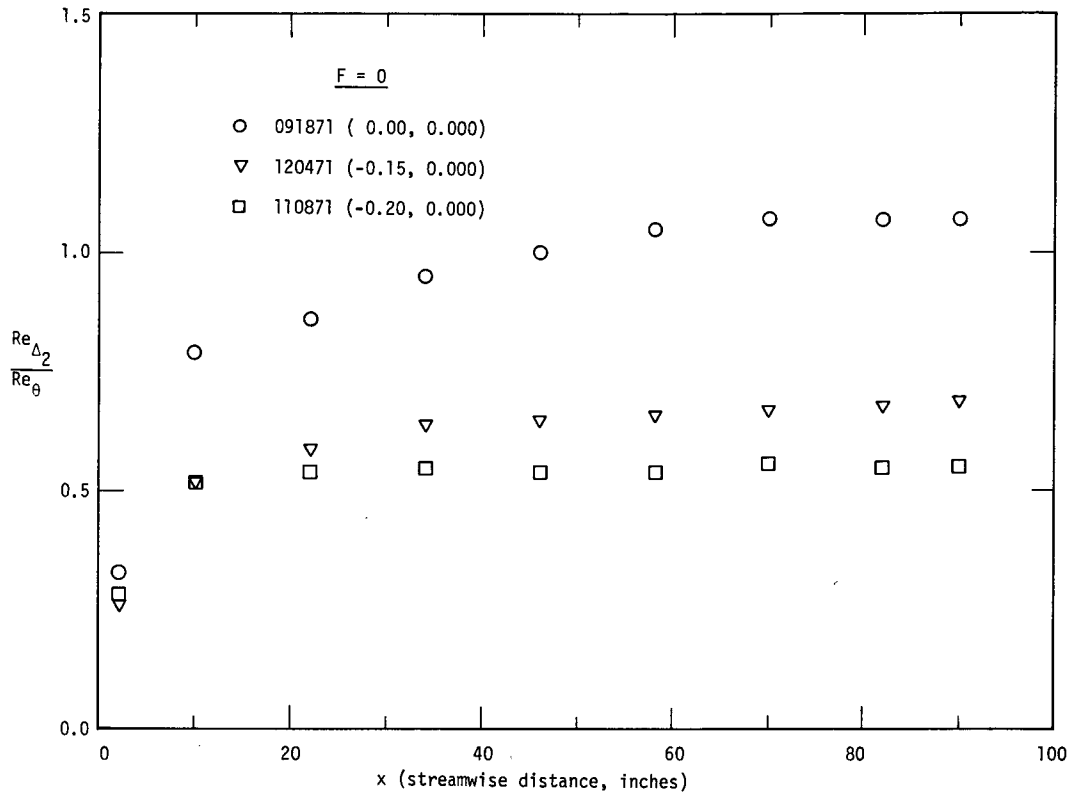


Figure 5-11 Influence of pressure gradient on Reynolds number ratio, $F = 0$

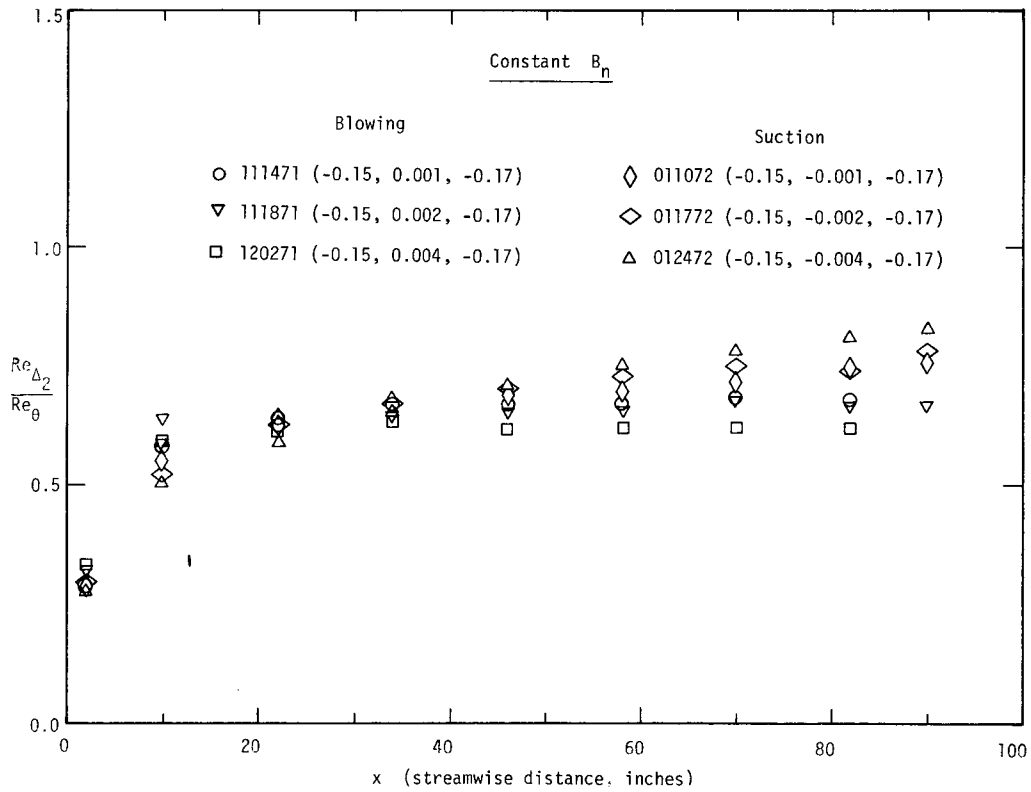


Figure 5-12 Influence of transpiration on Reynolds number ratio, $B_h = \text{constant}$

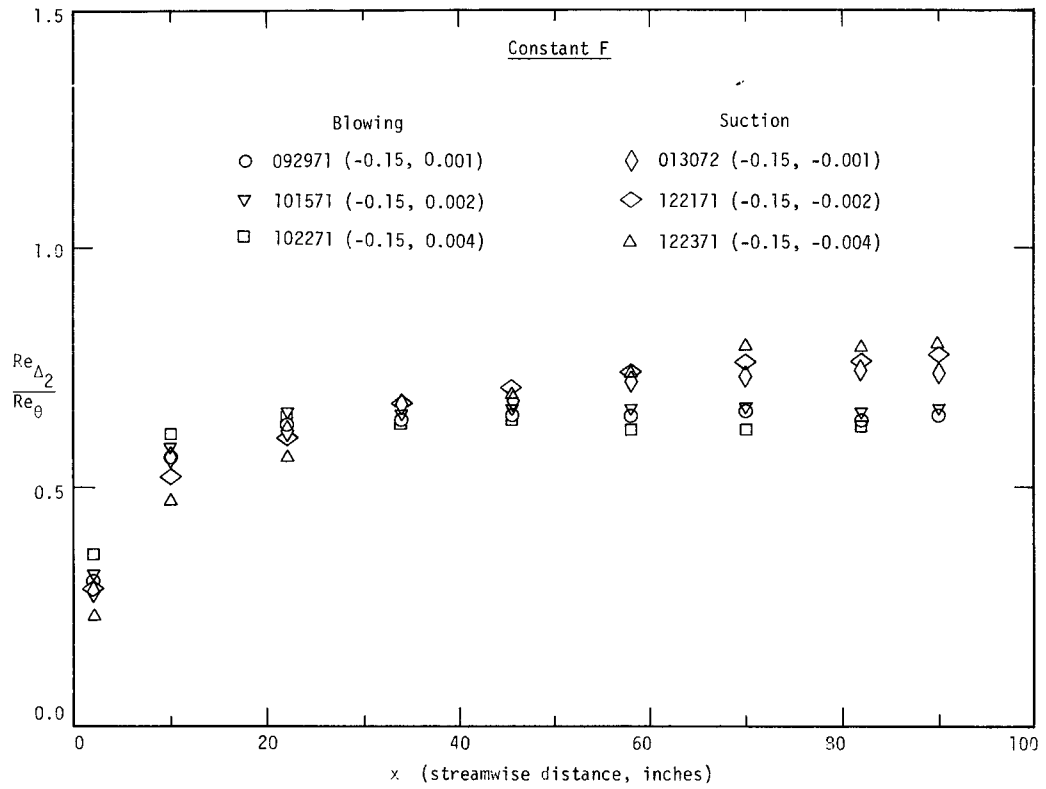


Figure 5-13 Influence of transpiration on Reynolds number ratio, $F = \text{constant}$

CHAPTER 6

HEAT FLUX AND TURBULENT PRANDTL NUMBER PROFILES

In recent years considerable heat transfer research has been directed toward experimentally obtaining the turbulent Prandtl number variation in a boundary layer. This is an extremely difficult problem since one must know not only the mean temperature and velocity profiles but also the heat flux and shear stress profiles. This chapter will outline the previous experimental turbulent Prandtl number studies, the method used to compute the heat flux profiles from mean temperature and velocity profiles will be outlined, and the computed turbulent Prandtl number results will be presented.

6.1 Previous Experimental Turbulent Prandtl Number Studies

Most previous experimental studies of the turbulent Prandtl number were concerned with fully developed pipe and channel flow. One reason for this is that the heat flux and shear stress profiles are known from theoretical considerations for those flow conditions. Blom [31] reviewed the status of experimental turbulent Prandtl number studies up through 1968 and, of the numerous references presented, only the data of Johnson [32] was concerned with the external turbulent boundary layer. Both Blom [31] and Johnson [32] experimentally studied the constant free stream velocity turbulent boundary layer, and measured $\overline{T'v'}$ downstream of an unheated starting length by means of a hot wire. The data of Johnson [32] exhibited considerable scatter with no definite trend. The data of Blom [31] indicated that Pr_t increased with y^+ close to the wall, reached a maximum of 0.8 - 1.2 in the range $y^+ = 50 - 80$, and then decreased with increasing y^+ . This maximum was not indicated by the data of Simpson [26] who studied the transpired turbulent boundary layer with constant free stream velocity. Simpson [26] concluded that for air, Pr_t was greater than unity close to the wall, and decreased to approximately 0.5 at the free stream. Kearney [7] presented turbulent Prandtl numbers for the accelerating transpired turbulent boundary layer, and found that acceleration increases Pr_t in the log-region. While

his data exhibited more scatter than the data of Simpson [26], both data sets had the same general trend: Pr_t greater than unity near the wall, and decreasing with increasing y^+ . A more recent study by Meier [30] for supersonic flow of air over a flat plate and for a supersonic nozzle is consistent with the trend of Simpson's [26] data. At this point in time, the bulk of the experimental data indicates that for the equilibrium external turbulent boundary layer in air, the turbulent Prandtl number is greater than unity close to the wall and decreases with increasing y . The data of this study will be additional evidence to support this belief.

6.2 Computation of Heat Flux Profiles

The two-dimensional continuity and energy equations of the boundary layer can be written as

$$\frac{\partial}{\partial x} (\rho u) + \frac{\partial}{\partial y} (\rho v) = 0 \quad (6-1)$$

$$\frac{\partial}{\partial x} (\rho u I) + \frac{\partial}{\partial y} (\rho v I) = - \frac{\partial \dot{q}''}{\partial y} + \frac{\partial}{\partial y} (\tau u) \quad (6-2)$$

Integrating (6-1) and (6-2) from the wall to any arbitrary y -location in the boundary layer, one obtains

$$Q^+ = 1 + \frac{\tau u}{\dot{q}_0''} + \frac{F}{St} \left(1 - \frac{I}{I_0} \right) + \frac{I}{\dot{q}_0''} \int_0^y \frac{\partial}{\partial x} (\rho u) dy - \frac{1}{\dot{q}_0''} \int_0^y \frac{\partial}{\partial x} (\rho u I) dy \quad (6-3)$$

If we let $y \rightarrow \infty$, then we obtain the energy integral equation (3-10) with $3-D = 0$. The first three terms of (6-3) represent the Couette-flow approximation to the local heat flux. The term $\tau u / \dot{q}_0''$ represents the ratio of the local viscous dissipation to the wall heat flux and is quite small for the low velocities of this study. However, this term was retained in all of the computations of this study.

The two integral terms in (6-3) are not important very near the wall, but they become dominant in the outer region of the boundary layer. In fact, Q^+ goes to zero at the outer edge of the boundary layer and the Couette-flow terms should balance these two integral terms. In practice, the Q^+ computed from (6-3) will not be identically zero at the free stream due to three dimensionality of the flow and the inability to evaluate the two integral terms very precisely. Since the streamwise derivative terms will be difficult to evaluate precisely, let us attempt to write the equations in a form where their significance becomes smaller. For example, derivatives of terms like $\partial(\rho u / \rho_\infty u_\infty) / \partial x$ and $\partial(\rho u I / \rho_\infty u_\infty I_0) / \partial x$ should be small in the outer part of the boundary layer because of approximate similarity. With the above ideas in mind, the two integral terms in (6-3) can be written as

$$\int_0^y \frac{\partial}{\partial x} (\rho u) dy = \frac{d}{dx} (\rho_\infty u_\infty) \int_0^y \frac{\rho u}{\rho_\infty u_\infty} dy + \rho_\infty u_\infty \int_0^y \frac{\partial}{\partial x} \left(\frac{\rho u}{\rho_\infty u_\infty} \right) dy \quad (6-4)$$

and

$$\int_0^y \frac{\partial}{\partial x} (\rho u I) dy = \frac{d}{dx} (\rho_\infty u_\infty I_0) \int_0^y \frac{\rho u I}{\rho_\infty u_\infty I_0} dy + \rho_\infty u_\infty I_0 \int_0^y \frac{\partial}{\partial x} \left(\frac{\rho u I}{\rho_\infty u_\infty I_0} \right) dy \quad (6-5)$$

Note that the x-derivatives must be evaluated at a constant y . They can be converted to derivatives at constant $\eta = y/\Delta$ by the chain rule

$$\left. \frac{\partial}{\partial x} \right)_y = \left. \frac{\partial}{\partial x} \right)_\eta - \frac{\eta}{\Delta} \frac{d\Delta}{dx} \left. \frac{\partial}{\partial \eta} \right)_x \quad (6-6)$$

Applying (6-4) - (6-6) to (6-3), one obtains

$$Q^+ = Q_c^+ + Q_1^+ + Q_2^+ \quad (6-7)$$

where

$$Q_c^+ = 1 + \frac{\tau u}{\dot{q}''} + \frac{F}{St} \left(1 - \frac{I}{I_0} \right) \quad (6-8a)$$

$$Q_1 \frac{St}{\Delta} \frac{I_0}{I} = \frac{d}{dx} [\ln(\rho_\infty u_\infty \Delta)] \int_0^\eta \frac{\rho u}{\rho_\infty u_\infty} d\eta + \int_0^\eta \frac{\partial}{\partial x} \left(\frac{\rho u}{\rho_\infty u_\infty} \right) d\eta \quad (6-8b)$$

$$-Q_2 \frac{St}{\Delta} = \frac{d}{dx} [\ln(\rho_\infty u_\infty \Delta)] \int_0^\eta \frac{\rho u I}{\rho_\infty u_\infty I_0} d\eta + \int_0^\eta \frac{\partial}{\partial x} \left(\frac{\rho u I}{\rho_\infty u_\infty I_0} \right) d\eta \quad (6-8c)$$

Note that the streamwise derivatives in (6-8) are now evaluated at constant η . These derivatives were evaluated by the three-point centered derivative formula

$$\left. \frac{\partial f}{\partial x} \right)_n = \frac{f_{n+1} - (1 - R^2)f_n - R^2 f_{n-1}}{x_{n+1} - x_n + R^2(x_n - x_{n-1})}, \quad R = \frac{x_{n+1} - x_n}{x_{n-1} - x_n} \quad (6-9)$$

The derivatives of $\rho_\infty u_\infty \Delta$ were evaluated by first determining a least squares curve fit of the form

$$\rho_\infty u_\infty \Delta = a(x-b)^c \quad (6-10)$$

and evaluating the derivative analytically.

When the temperature and velocity profiles were measured, it was impossible to ensure that the profile points for adjacent profiles were at the same values of η . Consequently, it was necessary to interpolate

in the upstream and downstream temperature and velocity profiles when evaluating the streamwise derivatives.

Computational experiments showed that $Q^+(\infty)$ evaluated from (6-8) was consistently closer to zero than that obtained from (6-3). However, the results from (6-8) were not identically zero. It was assumed that this discrepancy was solely due to the inability to evaluate the two integral terms accurately. In order to force the computed Q^+ profiles to satisfy the free stream boundary condition, a factor D was introduced, defined by

$$Q^+ = Q_c^+ + D(Q_1^+ + Q_2^+) \quad (6-11)$$

Evaluating (6-11) at the free stream, we obtain

$$D = - \frac{Q_c^+(\infty)}{Q_1^+(\infty) + Q_2^+(\infty)} \quad (6-12)$$

In the inner part of the boundary layer, both Q_1^+ and Q_2^+ are very small. Consequently, the D factor affects the Q^+ profiles only in the outer region. In general, it was found that $|D| < 0.1$ with many of the profiles having $|D| < 0.05$.

Figure (6-1) shows the influence of pressure gradient with no transpiration on the computed heat flux profiles. In the inner part of the boundary layer, the local value of Q^+ is essentially independent of pressure gradient. In contrast, the corresponding shear stress profiles* for the same three runs are shown in Figure (6-2). The shear stress profiles are strongly dependent on the pressure gradient. One would expect the above behavior, at least in the inner region, as a result of inspecting the Couette-flow expressions for Q^+ and τ^+ .

Figure (6-3) shows the influence of blowing and suction on the heat flux profiles. For blowing, the maximum heat flux occurs well away from

*The shear stress profiles were interpolated from the parallel study of Andersen [9].

the wall whereas the maximum heat flux for suction occurs at the wall (assuming no viscous dissipation). The uncertainty in computing Q^+ is zero at the wall and increases further away from the wall. Since Q^+ goes to zero at the free stream, the relative uncertainty goes to infinity. The Couette flow assumption for Q^+ was accurate to within 2% for $y^+ < 70$, as shown by the data in Figure (6-4).

6.3 Turbulent Prandtl Number Profiles

The eddy viscosity and eddy diffusivity are defined through the relationships

$$\tau = \rho(\epsilon_m + \nu) \frac{\partial u}{\partial y} \quad (6-13)$$

$$\dot{q}'' = -\rho c_p(\epsilon_h + \alpha) \frac{\partial T}{\partial y} \quad (6-14)$$

In terms of wall variables, (6-13) and (6-14) can be written as

$$\tau^+ = \frac{\mu}{\mu_0}(\epsilon_m^+ + 1) \frac{\partial u^+}{\partial y^+} \quad (6-15)$$

and

$$Q^+ = \frac{\mu}{\mu_0} \frac{\epsilon_h^+ + 1/Pr}{1 - E/2} \frac{\partial T^+}{\partial y^+} \quad (6-16)$$

Solving (6-15) and (6-16) for ϵ_m^+ and ϵ_h^+ respectively, one obtains

$$\epsilon_m^+ = \frac{\frac{\mu_0}{\mu} \tau^+}{\partial u^+ / \partial y^+} - 1 \quad (6-17)$$

and

$$\epsilon_h^+ = \frac{\mu_0}{\mu} \frac{(1 - E/2)Q^+}{\partial T^+/\partial y^+} - \frac{1}{Pr} \quad (6-18)$$

The turbulent Prandtl number is defined as

$$Pr_t = \frac{\epsilon_m^+}{\epsilon_h^+} \quad (6-19)$$

The critical experimental data necessary to calculate Pr_t are τ^+ , Q^+ , $\partial u^+/\partial y^+$, and $\partial T^+/\partial y^+$. The computation of both τ^+ and Q^+ was discussed in Section 6.1. As is well known, it is extremely difficult to differentiate experimental data such as velocity and temperature profiles, with any degree of certainty. After considerable numerical experimentation, the above derivatives were evaluated by curve-fitting a least-squares parabola through seven points, of the form (u^+, T^+) vs $\ln y^+$, and evaluating the derivative at the center point; the end points had to be treated as special cases. Near the wall where the temperature and velocity gradients are the steepest, one would expect considerable difficulty in evaluating the derivatives accurately. Also, since both derivatives approach zero at the free stream, the relative uncertainty there approaches infinity. Consequently, the uncertainty of the derivatives is the smallest in the "middle" portion of the boundary layer. The turbulent Prandtl number calculations in the outer region are additionally hampered by the large uncertainty in both τ^+ and Q^+ .

Figure (6-5) shows the influence of pressure gradient with no transpiration on the turbulent Prandtl number. It must be emphasized that the data in the inner region is quite uncertain; however, the data does have the consistent trend of being greater than unity very near the wall, and decreasing with increasing y^+ . The pronounced dip in Run 110871 is thought to be due to numerical difficulties associated with evaluating $\partial u^+/\partial y^+$ and $\partial T^+/\partial y^+$. In the logarithmic region where the turbulent

Prandtl number data is the most certain, an adverse pressure gradient produces a decrease in turbulent Prandtl number.

Figures (6-6) and (6-7) show the effects of blowing on Pr_t for the $m = -0.15$ flows. Again, the data is consistently above unity close to the wall, but there does not appear to be a consistent trend with blowing, for either the constant F or B_h flows.

Figures (6-8) and (6-9) show the effects of suction on the turbulent Prandtl number. Again, it is high near the wall with no consistent trend with suction as one moves away from the wall.

In the log-region, Pr_t appears to be strongly dependent on the pressure gradient. The parameter $K = \frac{v}{u_\infty} \frac{du_\infty}{dx}$ is one means of characterizing the pressure gradient. This might suggest that Pr_t in the log-region could be correlated as a function of K . However, the Pr_t data in the log-region for a given set of boundary conditions was relatively independent of x while K was a strong function of x . Therefore, to correlate $(Pr_t)_\ell$ we need a pressure gradient parameter that is approximately constant for a given run. Since $|K|$ decreases with x while Re_θ increases with x , their product might not vary with x . It was found that the parameter $KRe_\theta/(H-1)$ correlated the $(Pr_t)_\ell$ data reasonably well. This correlation is shown in Figure 6-10. Also shown in Figure 6-10 is one data point for a strongly accelerated flow taken from the data of Kearney [7]. This data point is consistent with the trend of this study; deceleration produces a decrease in the turbulent Prandtl number in the log-region.

Figures 6-11 thru 6-15 present one turbulent Prandtl number profile in outer region coordinates for each of the runs of this study. Data for $y/\delta > 0.7 - 0.8$ is not presented because of the high degree of uncertainty. All of the data shows a decrease in Pr_t with increasing y/δ . Also, it appears that a limit of $Pr_t = 0.5$ at the outer edge of the boundary layer would be reasonable.

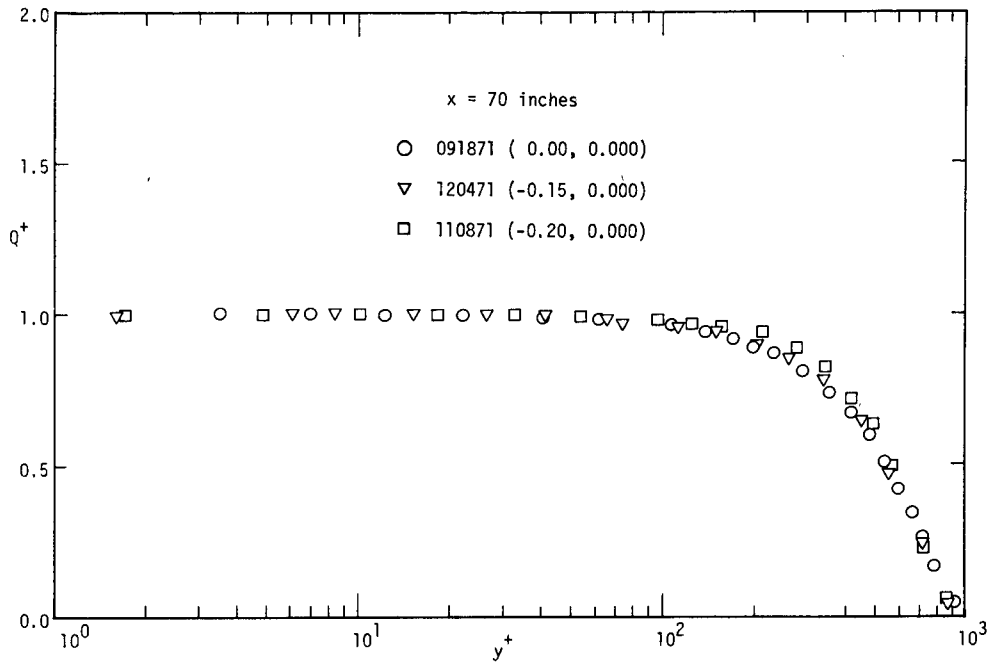


Figure 6-1 Influence of pressure gradient on heat flux profiles, $F = 0$

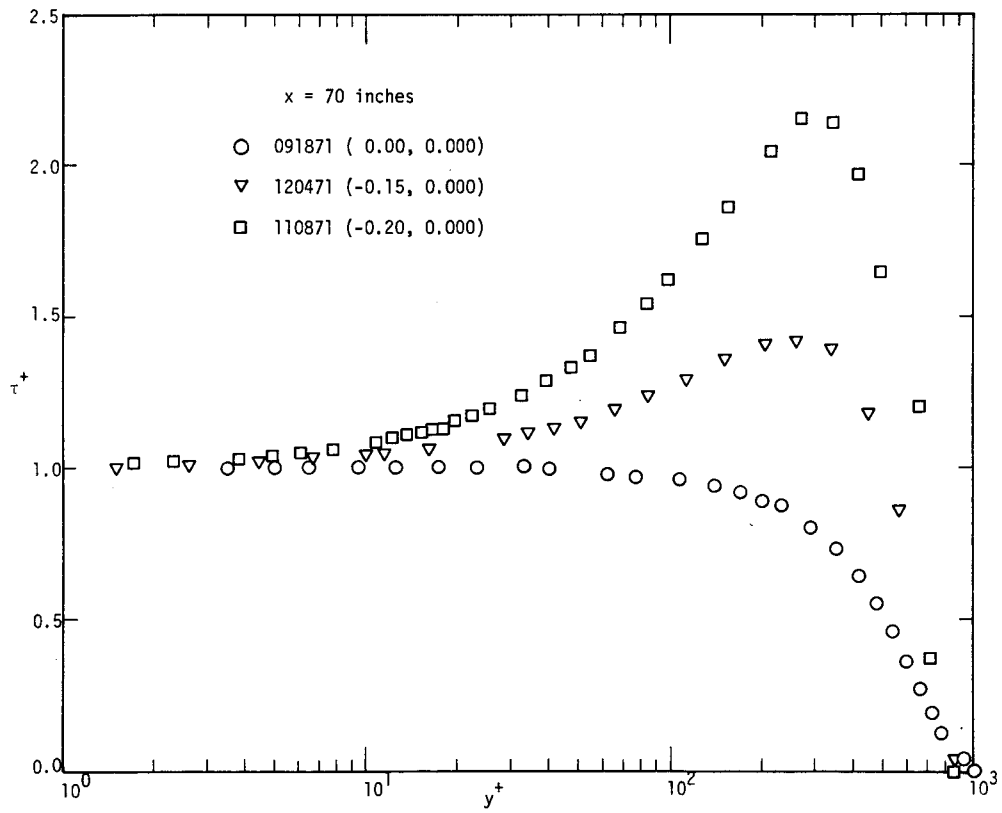


Figure 6-2 Influence of pressure gradient on shear stress profiles, $F = 0$

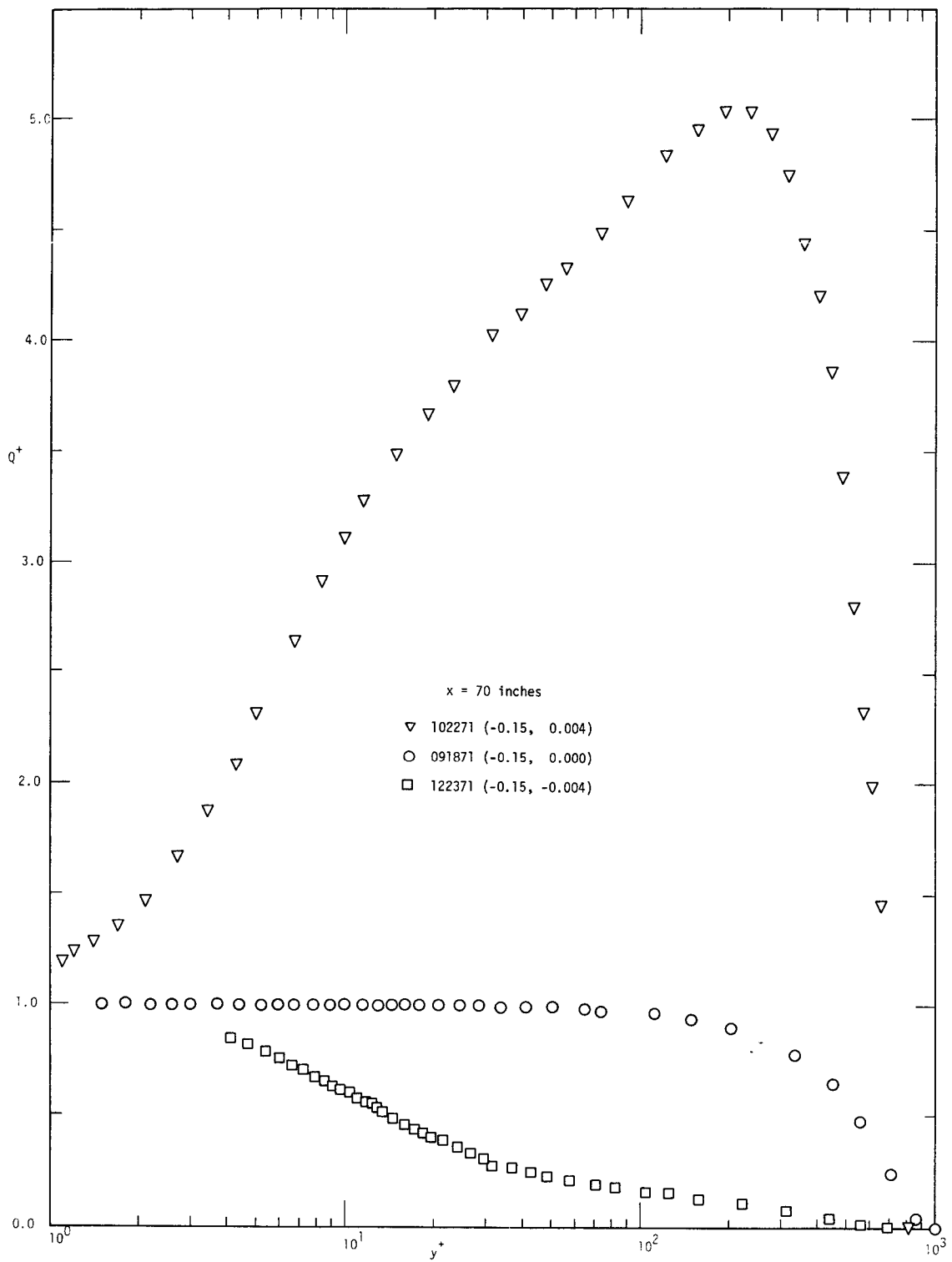


Figure 6-3 Influence of transpiration on heat flux profiles, $m = -0.15$

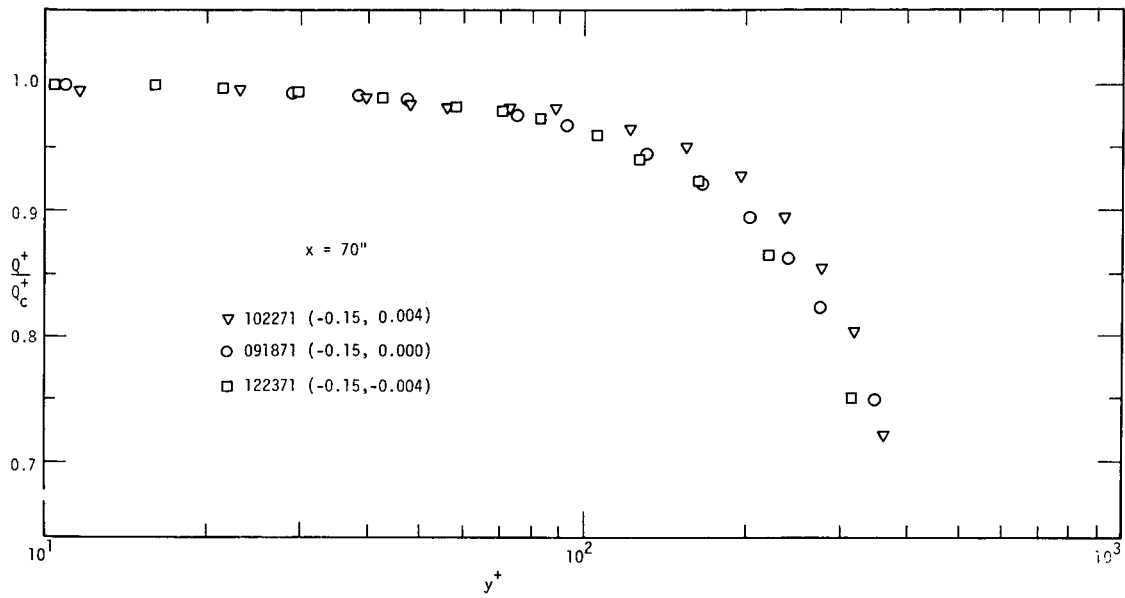


Figure 6-4 Validity of Couette flow assumption for computing heat flux profiles

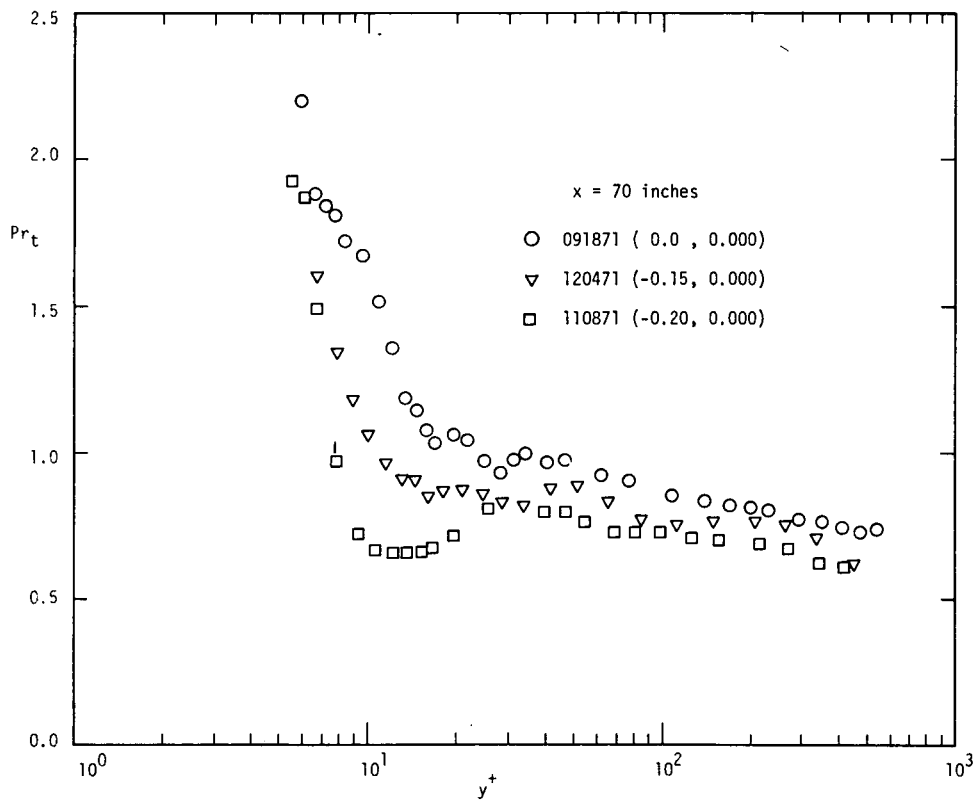


Figure 6-5 Influence of pressure gradient on turbulent Prandtl number profiles, $x = 70$ inches

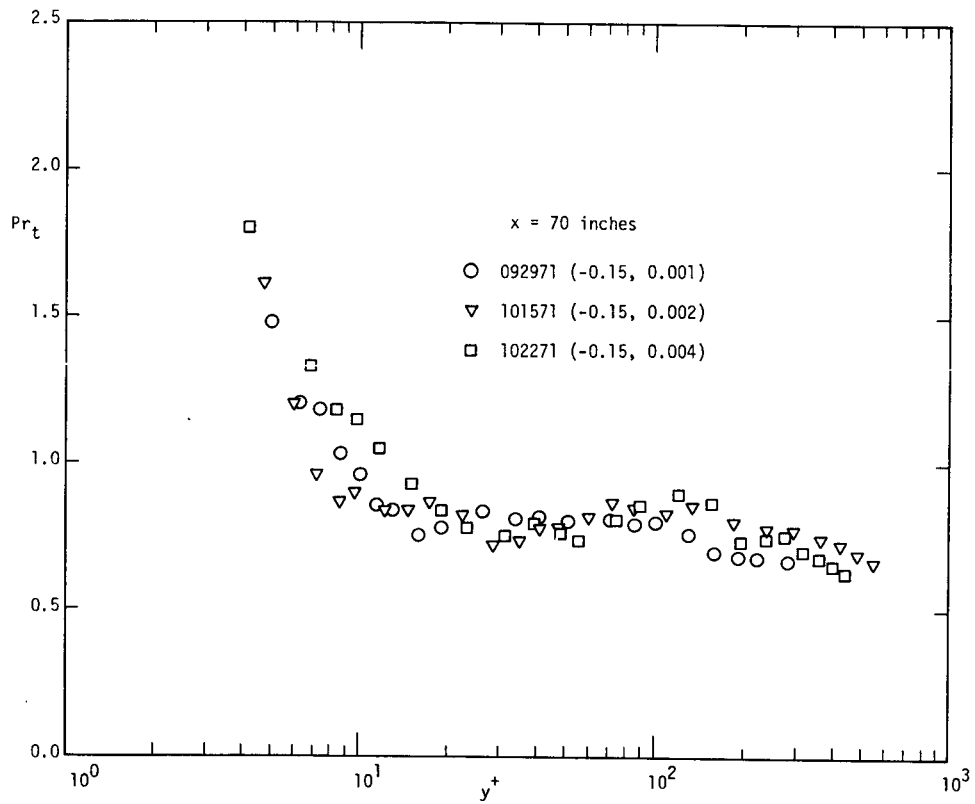


Figure 6-6 Influence of blowing on turbulent Prandtl number profiles, $x = 70$ inches

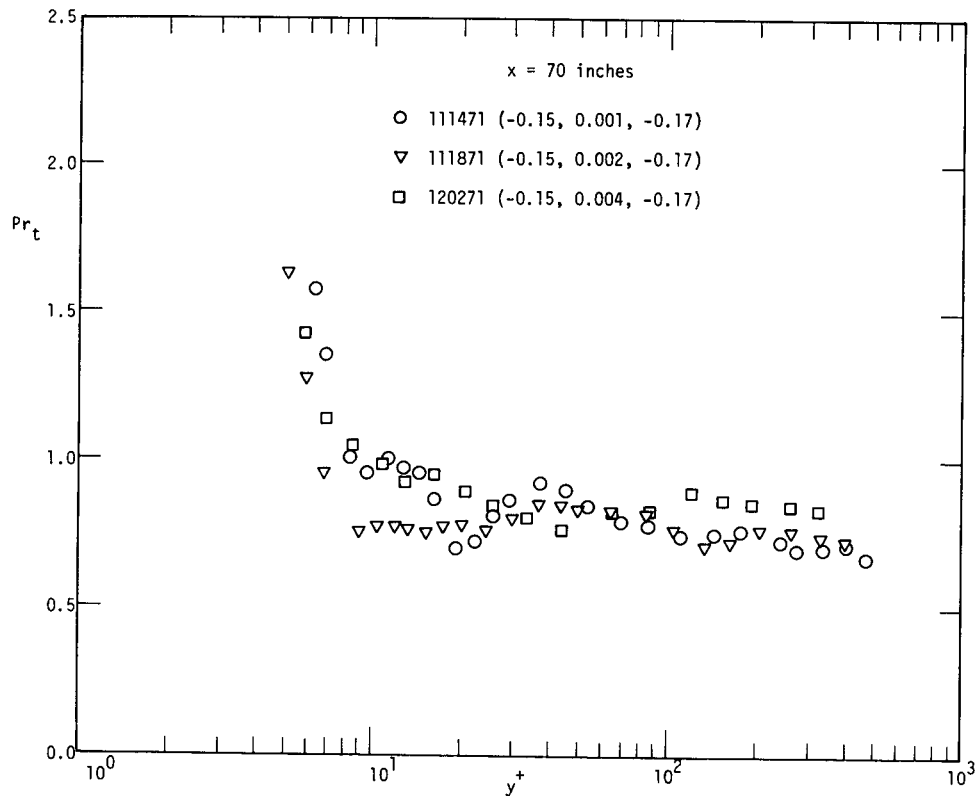


Figure 6-7 Influence of blowing on turbulent Prandtl number profiles, $x = 70$ inches



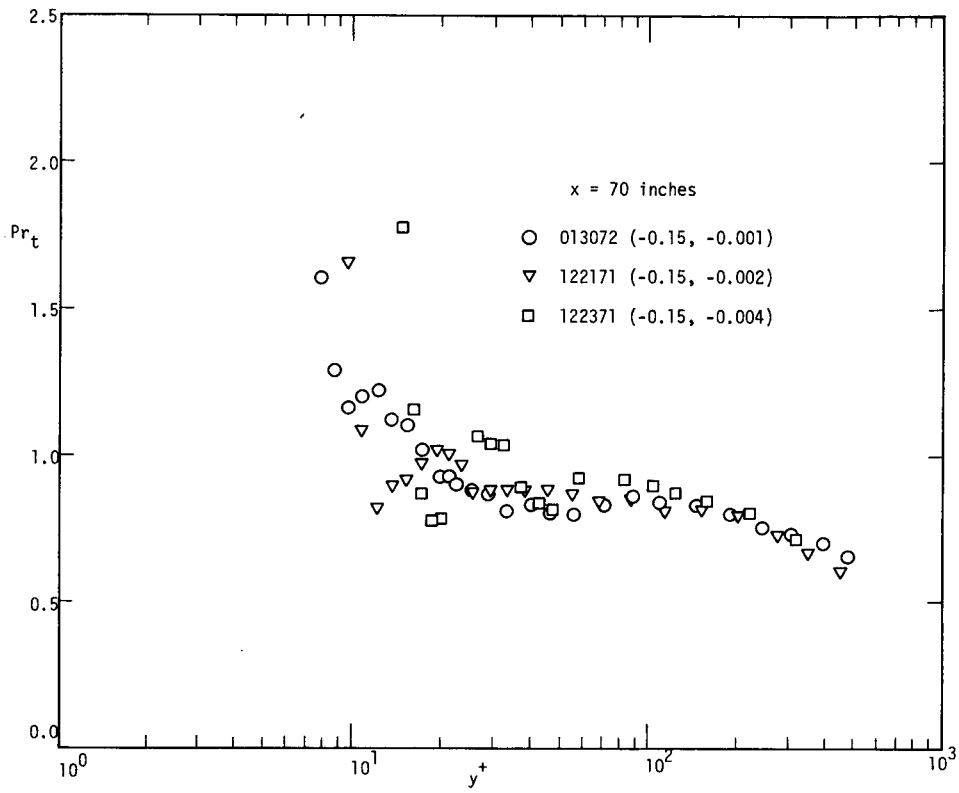


Figure 6-8 Influence of suction on turbulent Prandtl number profiles, $x = 70$ inches

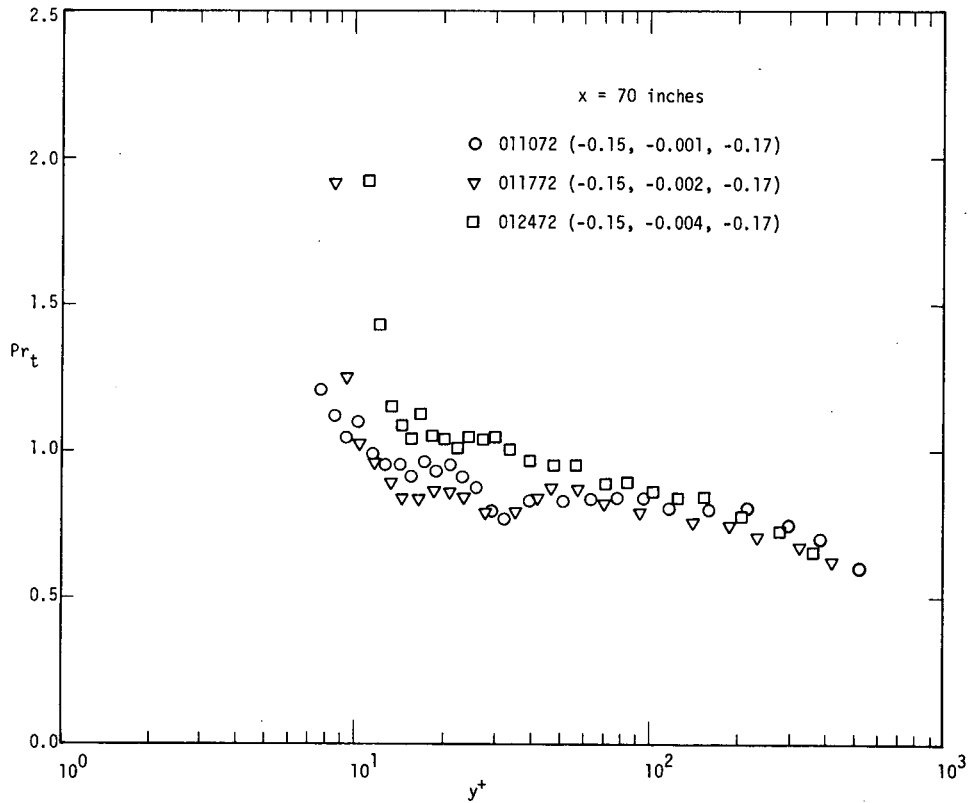


Figure 6-9 Influence of suction on turbulent Prandtl number profiles, $x = 70$ inches

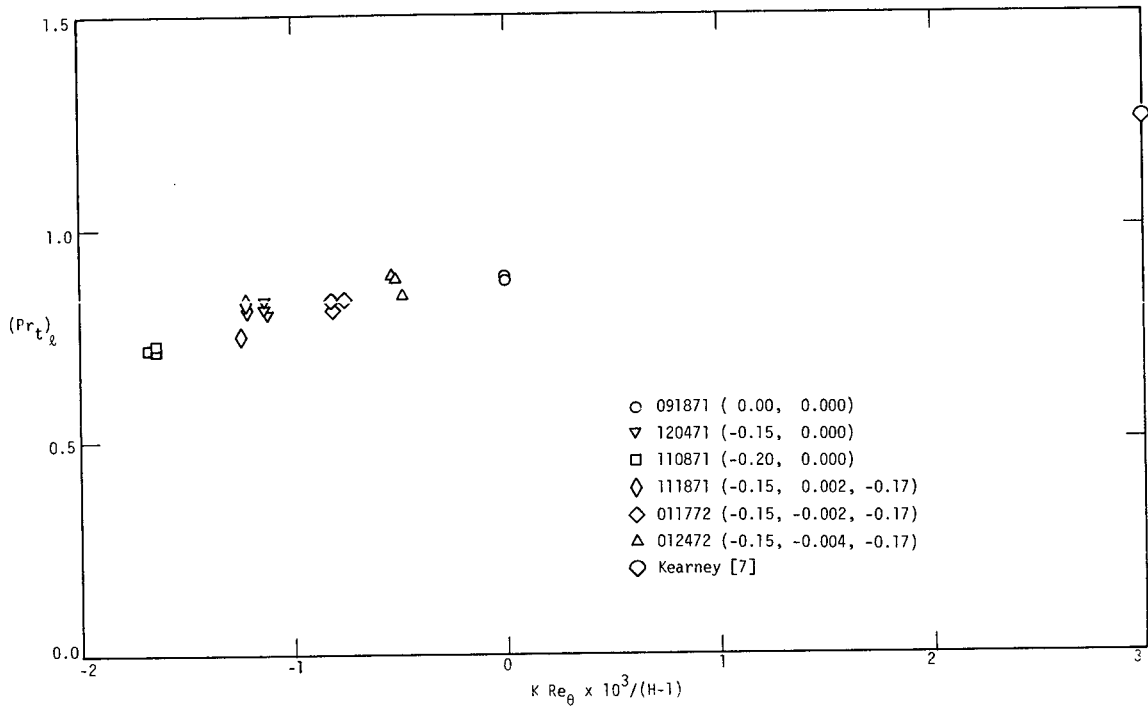


Figure 6-10 Variation of turbulent Prandtl number in log-region

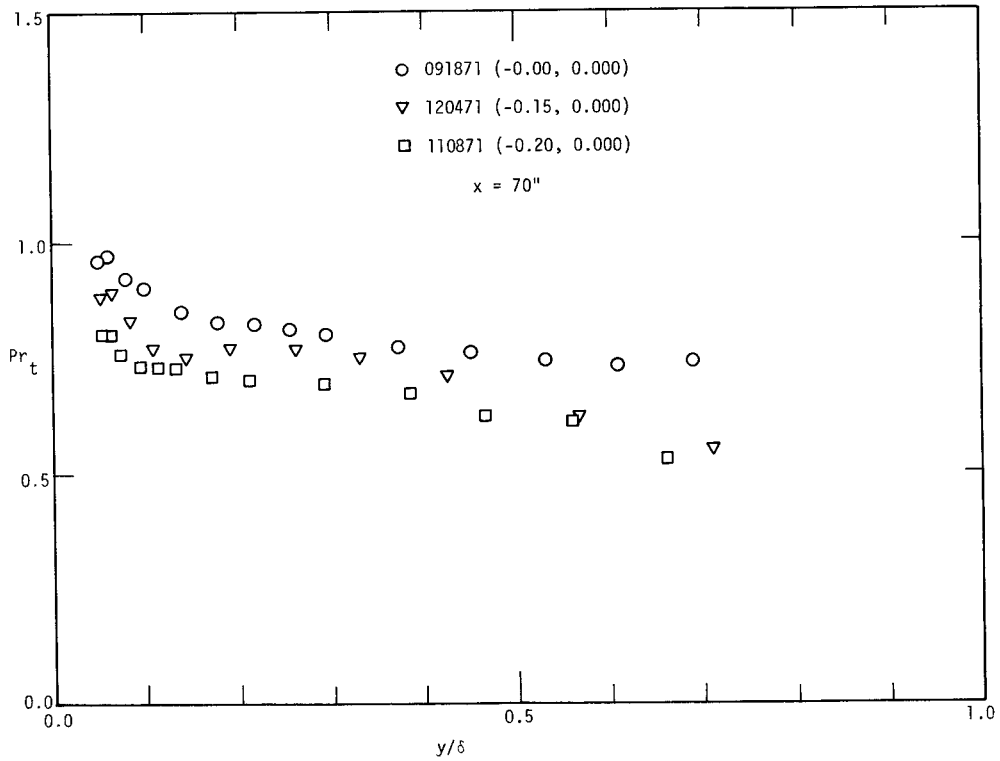


Figure 6-11 Influence of pressure gradient on turbulent Prandtl number profiles, $x = 70$ inches

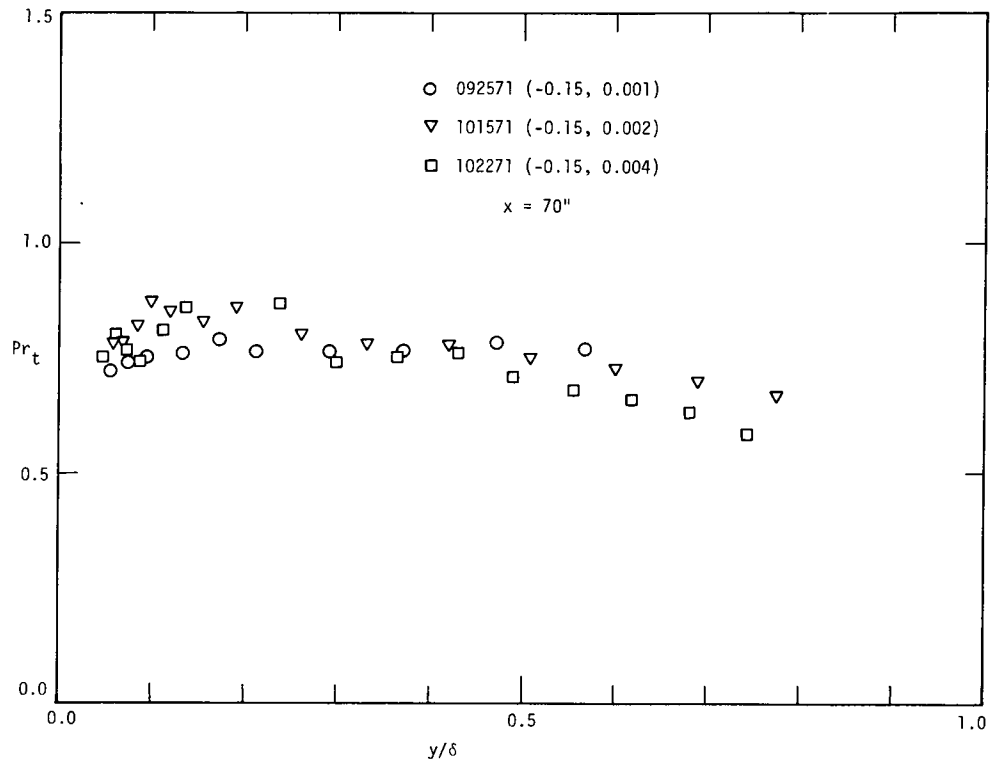


Figure 6-12 Influence of blowing on turbulent Prandtl number profiles, $x = 70$ inches

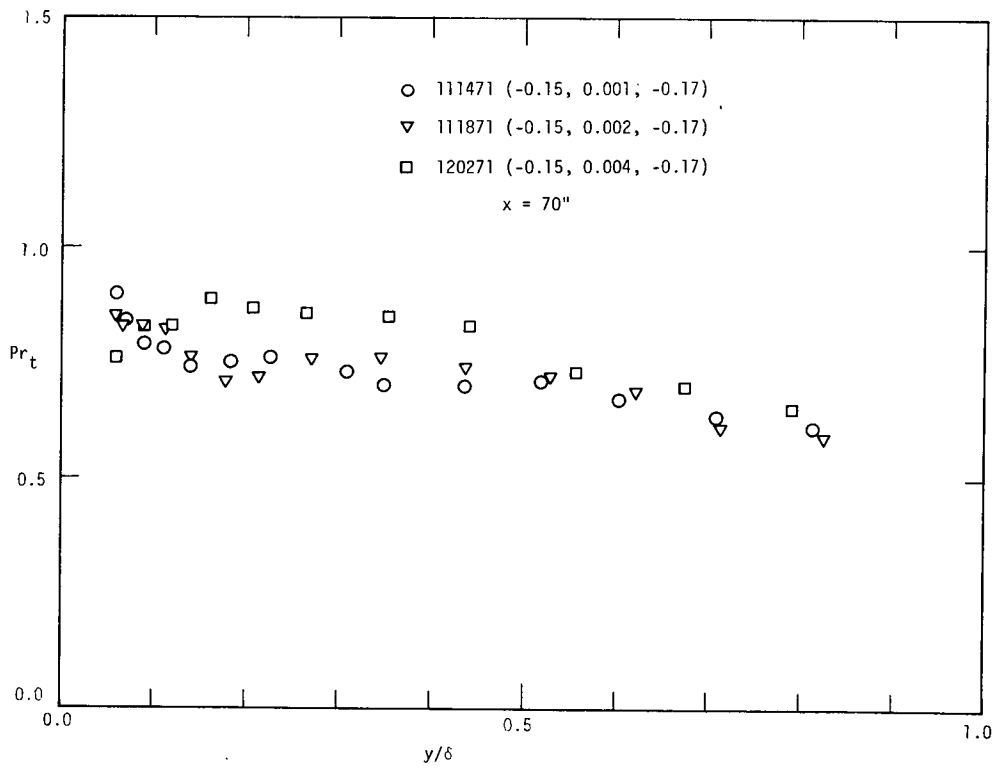


Figure 6-13 Influence of blowing on turbulent Prandtl number profiles, $x = 70$ inches

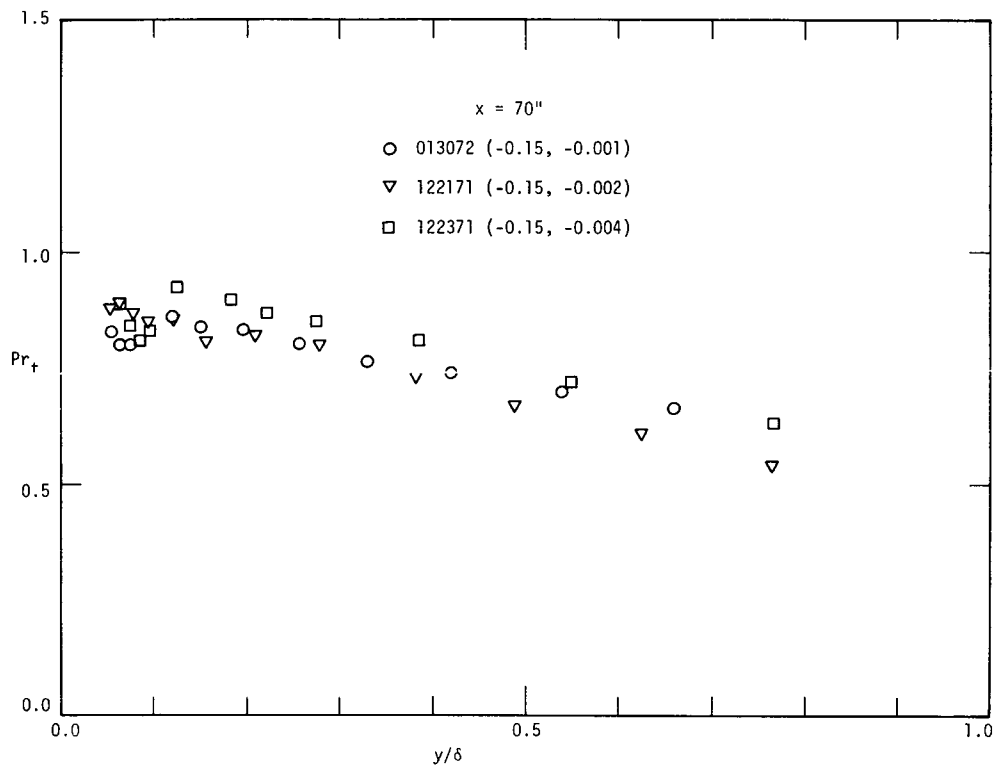


Figure 6-14 Influence of suction on turbulent Prandtl number profiles, $x = 70$ inches

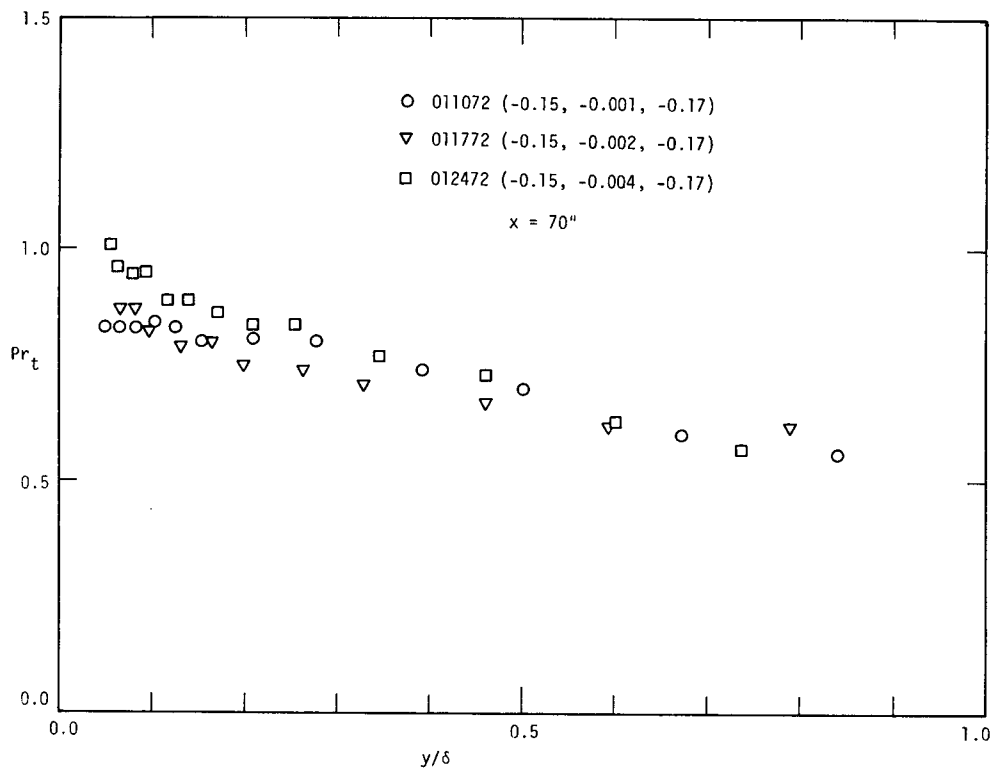


Figure 6-15 Influence of suction on turbulent Prandtl number profiles, $x = 70$ inches

CHAPTER 7

A TURBULENT PRANDTL NUMBER MODEL AND PREDICTION OF SELECTED RUNS

The turbulent Prandtl number has long been a useful concept in modeling turbulent heat transfer processes, even though the eddy diffusivity does not fully describe the events that occur in a turbulent boundary layer. Historically, the turbulent Prandtl number was first assumed to be unity. As more data became available, various analysts assumed that Pr_t was a constant but somewhat less than unity (for air). Beginning with Jenkins [21], a series of analysts have proposed turbulent Prandtl number models based on the idea that an "eddy" loses energy by molecular processes during its trajectory. Other examples of this type of eddy conduction model can be found in [22] - [24]. In the sections that follow, an analysis will be presented which is similar to that of Deissler's [22] for the turbulent Prandtl number variation in the inner region. In addition, an empirical correlation for Pr_t in the outer region will be shown, along with a comparison between experimental data and predictions using these models.

7.1 Turbulent Prandtl Number Model for Inner Region

The analysis that follows is quite similar to the analysis presented by Deissler [22]; consequently, only the more important points will be repeated here. Let us assume that an eddy originates at some distance y_1 from the wall and is convected upward with a characteristic velocity v . At this location y_1 , the eddy is at a temperature T_1 equal to the mean temperature of the surrounding fluid. During the trajectory of this eddy, it is continuously losing energy to the surrounding fluid by molecular conduction. (It should be noted that the momentum transfer problem has no analogous loss mechanism, as opposed to the model of Jenkins [21]). When the eddy has traveled a distance ℓ in the vertical direction, it breaks up and mixes with the surrounding fluid. The eddy temperature at this new location $y_2 = y_1 + \ell$ is T'_2 , which is dif-

ferent from the mean fluid temperature T_2 at y_2 . The energy transfer due to the turbulent mixing at the location y_2 is assumed to be given by

$$\dot{q}_t'' = \rho c_p v (T_2' - T_2) \quad (7-1)$$

Assuming that the mixing length ℓ is small, (7-1) can be written as

$$\dot{q}_t'' = - \rho c_p v \ell \left[\frac{T_2' - T_2}{T_1 - T_2} \right] \frac{\partial T}{\partial y} \quad (7-2)$$

The eddy diffusivity for heat transfer is defined through the relationship

$$\dot{q}_t'' = - \rho c_p \epsilon_h \frac{\partial T}{\partial y} \quad (7-3)$$

From (7-2) and (7-3), we obtain

$$\epsilon_h = v \ell \left[\frac{T_2' - T_2}{T_1 - T_2} \right] \quad (7-4)$$

But the product $v \ell$ should be proportional to the eddy viscosity ϵ_m . Consequently, the turbulent Prandtl number can be written as

$$Pr_t = \frac{\epsilon_m}{\epsilon_h} = C_1 \frac{T_1 - T_2}{T_2' - T_2} = C_1 \theta' \quad (7-5)$$

Equation (7-5) is the same as that derived by Deissler [22], except that Deissler set $C_1 = 1$. As we shall see later, the constant C_1 can be significantly different from unity.

With (7-5) as the basic model for the turbulent Prandtl number, the problem remaining is to evaluate the eddy temperature during its trajectory. Various investigators have proposed eddy conduction models of varying degrees of sophistication. Three of the models that are available in the literature are:

Deissler [22],

$$\theta' = \frac{\phi}{1 - e^{-\phi}} \quad (7-6)$$

Jenkins [21]*,

$$\theta' = \frac{\phi}{1 - \frac{90}{\pi^4} \sum_{n=1}^{\infty} \frac{1}{n^4} \exp\left(-\frac{n^2 \pi^2}{15} \phi\right)} \quad (7-7)$$

and, Lykoudis [23]

$$\theta' = \frac{\pi^2/6}{\sum_{n=1}^{\infty} \frac{1}{n^2} \exp\left(-\frac{n^2 \pi^2}{15} \phi\right)} \quad (7-8)$$

where the parameter ϕ is given by

$$\phi = \frac{C_2}{\frac{\epsilon_m}{\nu} Pr} \quad (7-9)$$

In the above analyses, the significant parameter is the turbulent Peclet number $Pe_t = Pr \epsilon_m / \nu$. However, it should be noted that Pe_t is independent of the molecular viscosity. Figure 7-1 presents a comparison of the three different eddy conduction models. The Deissler [22] and Jenkins [21] models are quite similar. Although the Lykoudis [23] model appears quite different, the yet unspecified constant C_2 for this model would be quite different from the C_2 for the other two models. All

*When (7-7) is used in conjunction with (7-5) for a Pr_t model, the result is quite different from that proposed originally t by Jenkins [21].

three models have a common asymptote of unity for large values of eddy viscosity ϵ_m .

The Deissler [22] model is essentially a lumped parameter analysis. Since it is the simplest of the three model presented here, it was adopted for this study. It is felt that any of the above three models would prove adequate for prediction purposes provided the constants were chosen in a consistent manner. The turbulent Prandtl number model used for the remainder of this study was*

$$Pr_t = C_1 \frac{\phi}{1 - e^{-\phi}}, \quad \phi = \frac{C_2}{\frac{\epsilon_m}{\nu} Pr} \quad (7-10)$$

Equation (7-10) has two free constants; in reality, C_1 and C_2 are probably not universal constants and must be empirically correlated for each class of data. For large values of ϵ_m , (7-10) approaches $Pr_t = C_1$. Therefore, C_1 should be approximately equal to the turbulent Prandtl number in the log-region. The constant C_2 controls the portion of the boundary layer where a rapid decrease in Pr_t occurs. The limiting case of $C_2 = 0$ would correspond to $Pr_t = C_1$ throughout the inner portion of the boundary layer.

The problem we are faced with now is how to evaluate C_1 and C_2 . Computational experiments showed that a computed temperature profile is much more sensitive to changes in C_1 than in C_2 . Therefore, based on these computational experiments, a nominal value of $C_2 = 0.5$ was chosen. Since C_1 is essentially the turbulent Prandtl number in the log-region, the data in Figure 6-10 could be taken as representing C_1 . However, due to the experimental uncertainty in the Pr_t calculations, it was decided to integrate the equations from the wall out to the log-

* (7-10) is essentially the same as a limiting case of the analysis presented by Tokuro [24]. However, the values of C_1 and C_2 for this study are quite different from those proposed by Tokuro.

region and vary the constant C_1 (with $C_2 = 0.5$) until the computed temperature matched the experimental temperature at a particular point. The y^+ location where the matching occurred varied with pressure gradient and transpiration but was always in the log-region. The computational procedure was to integrate (6-16) numerically using the computed heat flux profiles discussed in CHAPTER 6 and (7-10) for the turbulent Prandtl number model.

$$\frac{dT^+}{dy^+} = \frac{\frac{\mu_0}{\mu^+}(1 - E/2) Q^+}{\frac{\epsilon_m^+}{Pr_t} + \frac{1}{Pr}} \quad (7-11)$$

The eddy viscosity model for ϵ_m^+ was that proposed by Andersen [9]. The results of this series of computational experiments is shown in Figure 7-2, and are adequately represented by the empirical equation

$$C_1 = 0.8(\gamma + 2)^{0.17} \quad (7-12)$$

where γ is defined as

$$\gamma = K \times 10^3 Re_\theta / (H-1) \quad (7-13)$$

For the origin of γ , see Section 6.2. The data in Figure 7-2 is consistent with the data in Figure 6-10 and has less scatter.

7.2 Turbulent Prandtl Number Model for Outer Region

Rotta [25] proposed that the turbulent Prandtl number in the outer region be correlated by

$$Pr_t = 0.95 - 0.45(y/\delta)^2 \quad (7-14)$$

Equation (7-14) also fits the zero pressure gradient data of Simpson [26] quite well. Note that this equation has a limit of 0.5 at the outer edge of the boundary layer, which is consistent with the data in Figures 6-11 thru 6-15. Since we have already established that the turbulent Prandtl number in the log-region depends on parameter γ , (7-14) will

not be adequate for the data of this study. Using (7-14) as a guide, it is proposed that Pr_t in the outer region be modeled by

$$Pr_t = 0.5 + b_1[1 - (y/\delta)^2] \quad (7-15)$$

The constant b_1 was determined by requiring that (7-15) agree with (7-10) at some point in the boundary layer. The match point for these two expressions was at $y/\delta = \lambda/\kappa$, which is commonly used as the dividing point between the inner and outer part of a mixing length model for momentum transfer. The values of λ and κ were taken from Andersen [9]. Matching these two expressions yields

$$b_1 = \frac{C_1 - 0.5}{1 - \left(\frac{\lambda}{\kappa}\right)^2} \quad (7-16)$$

Since the computed turbulent Prandtl numbers in the outer region are quite uncertain, it is difficult to judge the validity of (7-15) using only the Pr_t data of CHAPTER 6. However, one check will be to use (7-15) with a finite-difference boundary layer prediction program. This will be discussed in subsequent sections.

7.3 Comparison of Predicted Stanton Numbers With Experimental Data

In order to verify the turbulent Prandtl number model proposed in Section 7.2, the model was used in conjunction with a version of the Patankar-Spalding [29] computational procedure for solving the boundary layer equations. The mean velocity field closure was accomplished with the model proposed by Andersen [9]. This mixing-length model is given by

$$\ell = \begin{cases} \kappa y [1 - \exp(-y/A)], & y \leq \lambda\delta/\kappa \\ \lambda\delta, & y > \lambda\delta/\kappa \end{cases} \quad (7-17)$$

The length scale, A , in this van Driest type model was obtained from

$$A = \frac{A_0}{\sqrt{\tau^+(3A)}} \quad (7-18)$$

The parameter λ showed a weak dependence on F and Re_θ ; for the details of this, see Andersen [9]. Four runs were selected as test cases. These runs cover a wide range of transpiration boundary conditions and for two of the pressure gradients of this study. In all cases, the experimental velocity and temperature profiles at $x = 2$ inches were used as the starting profiles.

Figure 7-3 presents a comparison of experimental Stanton numbers with predictions for the zero pressure gradient, no transpiration run. The experimental data presented for all of the Stanton number comparisons was the "best interpretation" of runs 1 and 2 (see Section 4.3). The agreement is excellent. Figure 7-4 presents the Stanton number comparison for the adverse pressure gradient $u_\infty \sim x^{-0.15}$ with no transpiration. The agreement is within 5%. Figures 7-5 and 7-6 present the Stanton number comparisons for the strongest suction and strongest blowing boundary conditions respectively, where B_h was held constant. The strong blowing run shows the largest discrepancy with the predicted values as much as 12% high. However, the predictions are within the experimental uncertainty.

Andersen [9] presented a comparison of experimental data with predictions for the hydrodynamics of some of the same flows presented here. He concluded that his mixing length model performed worst for the case of strongest blowing. Since the turbulent Prandtl number model proposed in this study depends on Andersen's [9] mixing length model, it is not possible to ascertain whether the relatively poor Stanton number predictions for strong blowing could be blamed on the mixing length model, turbulent Prandtl number model, or the experimental uncertainty in determining Stanton number.

7.4 Comparison of Predicted Temperature Profiles With Experimental Data

In this section, a predicted temperature profile will be compared with an experimental profile for each of the four runs discussed in Section 7.3. In all cases, the x-location for comparison was chosen to be 70 inches. This x-location was chosen because the flow should be in equilibrium this far downstream. Figure 7-7 presents the temperature profile comparison for the zero pressure gradient, no transpiration run. The agreement is quite good. Figures 7-7 - 7-10 present the temperature profile comparisons for the other three runs. Again, the agreement is quite good. In fact, the temperature profile agreement is better than the Stanton number agreement (except for the zero pressure gradient, no transpiration run). This raises the question of how the temperature profiles could agree better than the Stanton numbers. The particular computer program used computes the wall heat flux by evaluating the temperature gradient at the wall numerically. The Stanton number data might be improved by using an energy integral equation to evaluate the Stanton number from the predicted rate of growth of the boundary layer, but this has not been attempted.

7.5 Some Comments on a Heat Transfer Mixing Length Model

Meier [30] proposed that the turbulent heat transfer processes in the inner part of the boundary layer could be modeled using a heat transfer mixing-length. This proposed model takes the form

$$\epsilon_h^+ = \ell_h^{+2} \frac{\partial u^+}{\partial y^+} \quad (7-19)$$

where the non-dimensional heat transfer mixing length is given by

$$\ell_h^+ = \kappa_h y^+ [1 - \exp(-y^+/A_h^+)] \quad (7-20)$$

where κ_h is a heat transfer parameter analogous to the von Kármán constant κ and A_h^+ is a measure of the thermal boundary layer sublayer thickness. If one uses a momentum transfer mixing length model similar to (7-20), then the turbulent Prandtl number in the log-region (large y^+)

is given by

$$\text{Pr}_t = \left(\frac{\kappa}{\kappa_h} \right)^2, \quad y^+ \text{ large} \quad (7-21)$$

Meier [30] proposed that $(\kappa/\kappa_h)^2 = 0.86$ for air. It will be shown in this section that if $\kappa = 0.41$ (as used by Andersen [9] and many other investigators), then κ_h must be a function of pressure gradient (and possibly transpiration rate).

If one plots ℓ_h^+/y^+ as a function of y^+/A_h^+ , (7-20) indicates that the limit in the log-region should be κ_h . Figure 7-11 shows the influence of pressure gradient with no transpiration on the heat transfer mixing length ℓ_h^+ . This data clearly indicates that κ_h increases in an adverse pressure gradient. This is consistent with the fact that the turbulent Prandtl number in the log-region decreases in an adverse pressure gradient. The conclusion is that if one attempted to extend Meier's [30] model to heat transfer with adverse pressure gradient, one must correlate κ_h as a function of pressure gradient.

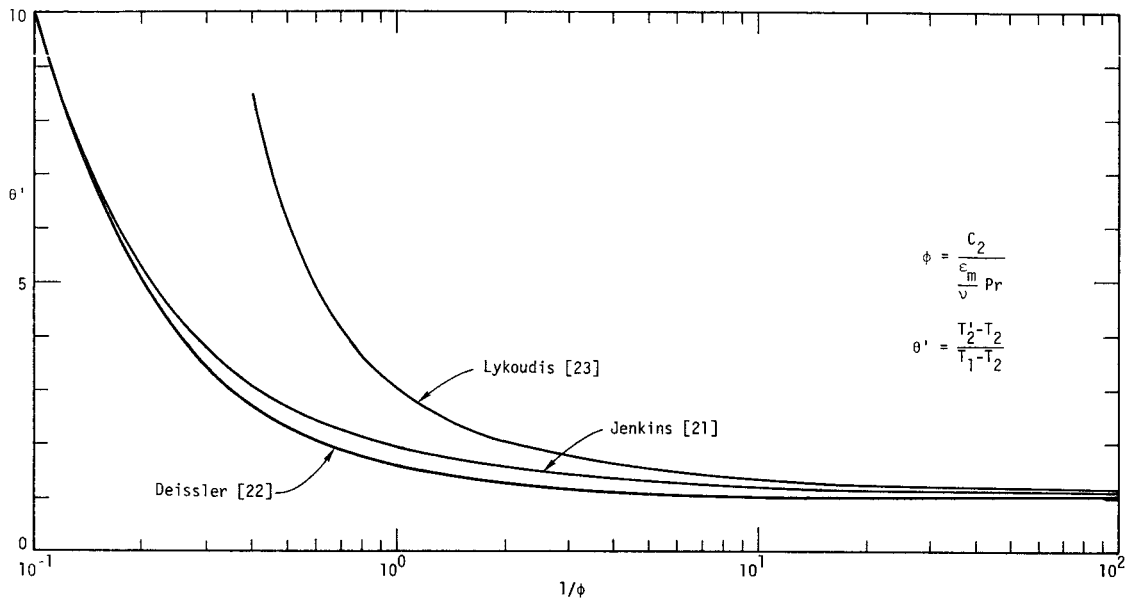


Figure 7-1 Comparison of different eddy heat transfer models

C2

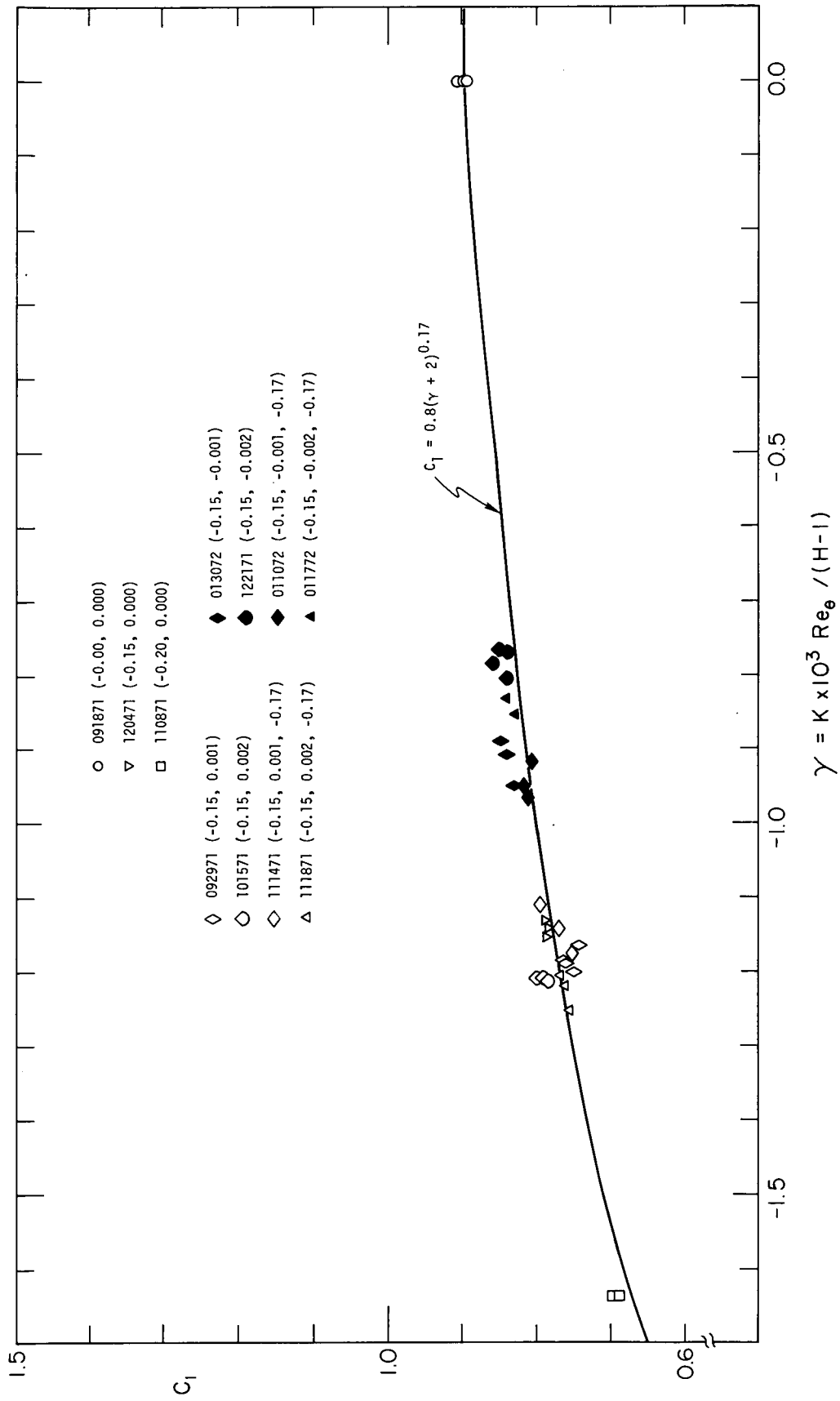


Figure 7-2 Variation of C_1 in the turbulent Prandtl number model

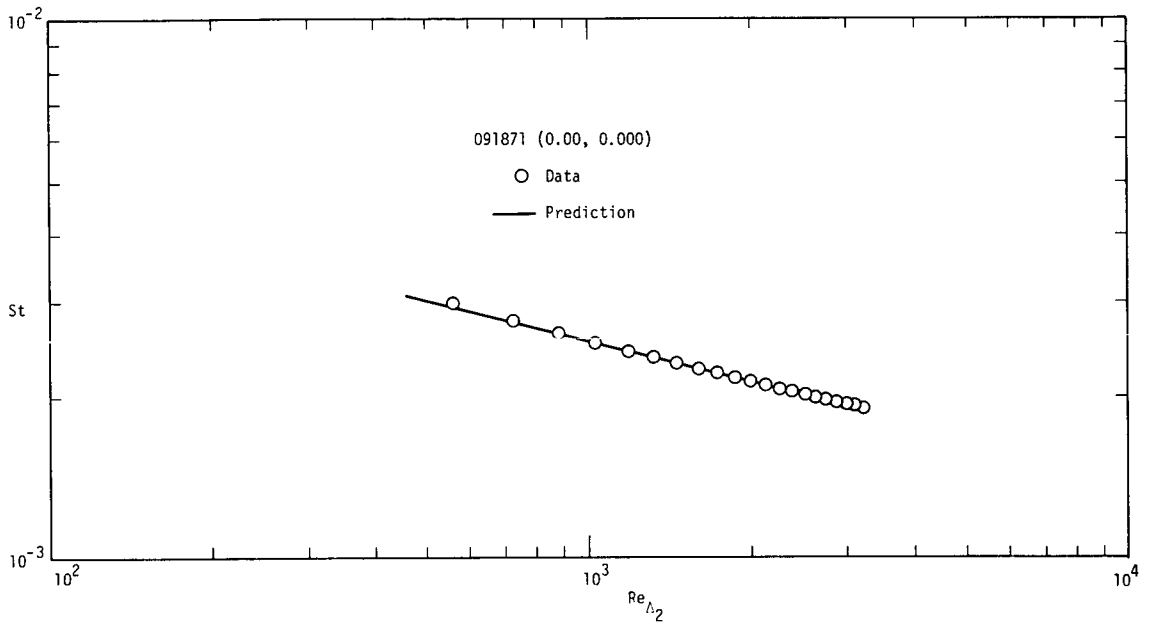


Figure 7-3 Comparison of predicted Stanton numbers with experimental data, run 091871

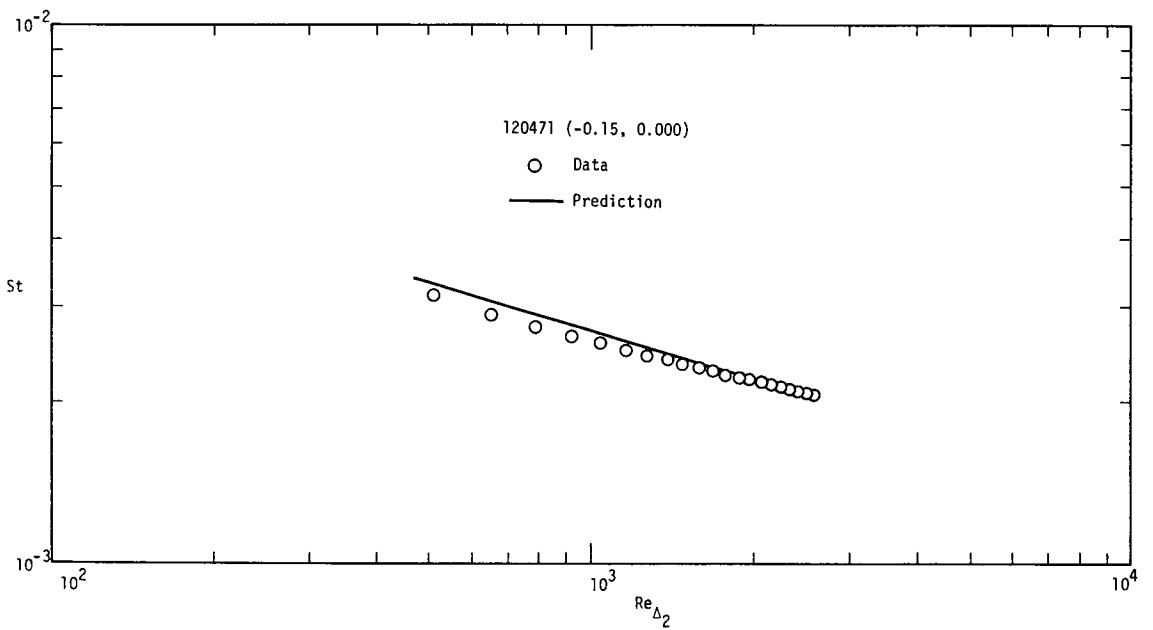


Figure 7-4 Comparison of predicted Stanton numbers with experimental data, run 120471

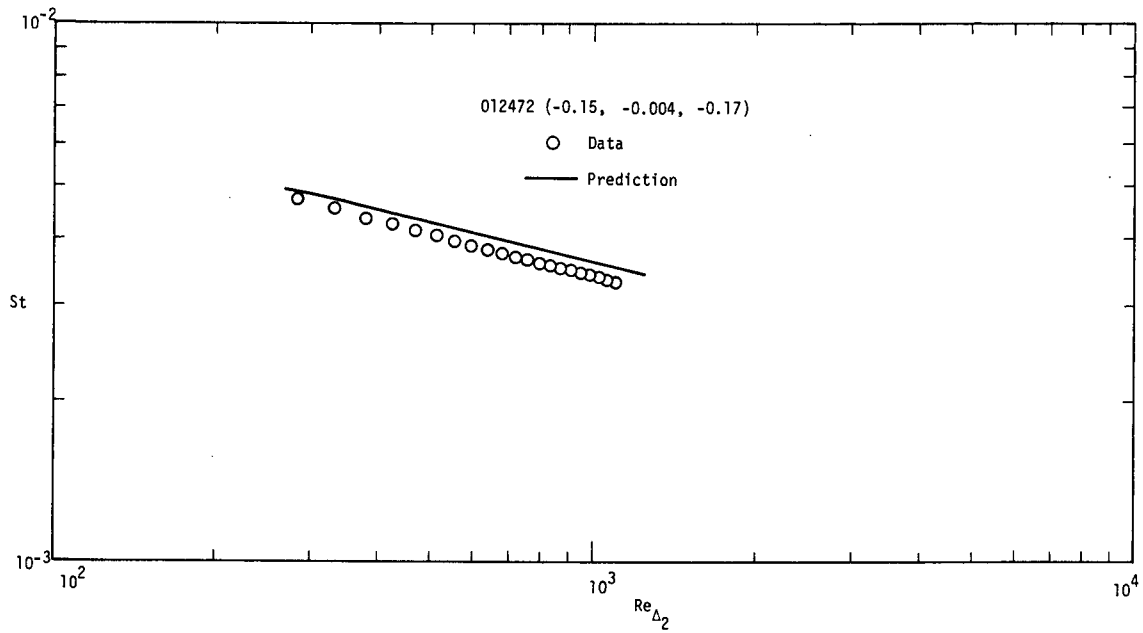


Figure 7-5 Comparison of predicted Stanton numbers with experimental data, run 012472

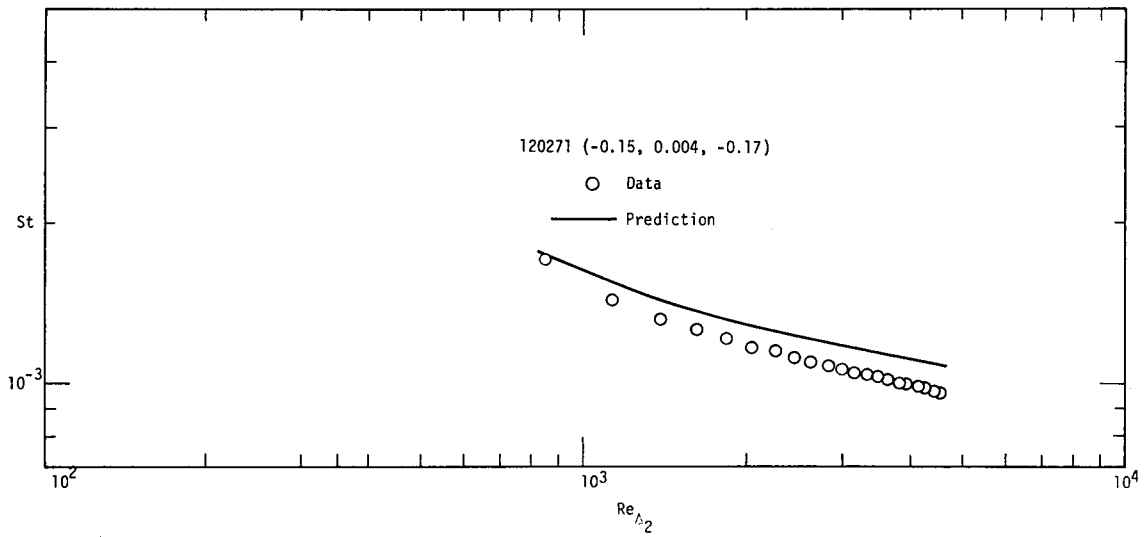


Figure 7-6 Comparison of predicted Stanton numbers with experimental data, run 120271

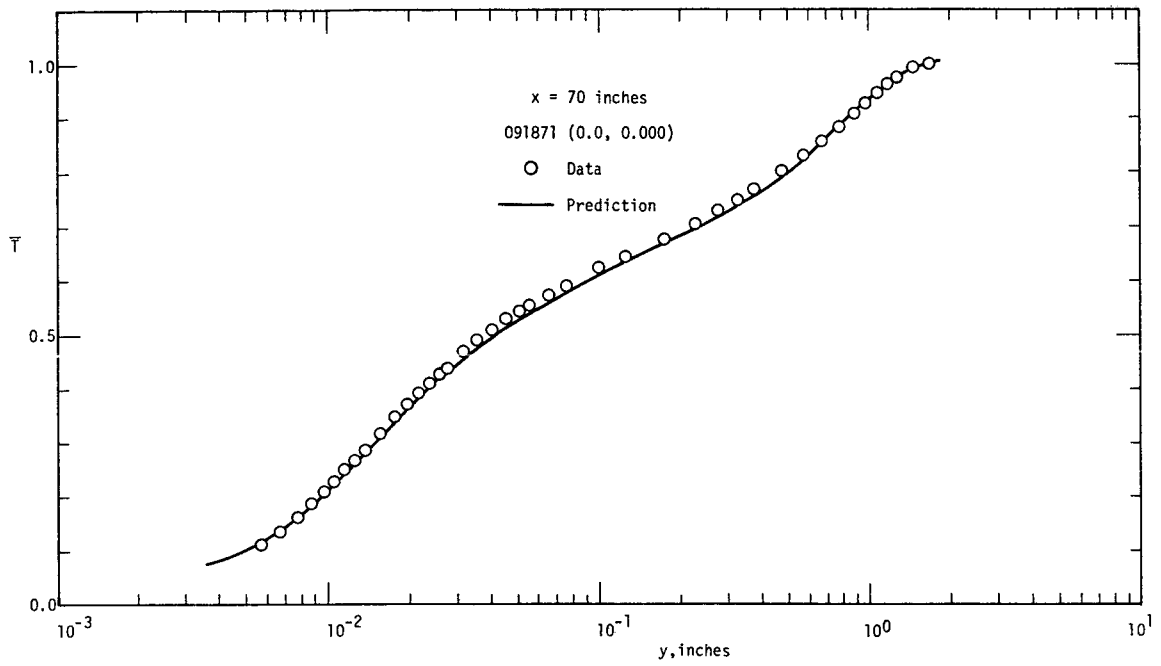


Figure 7-7 Comparison of predicted temperature profile with experimental data, run 091871

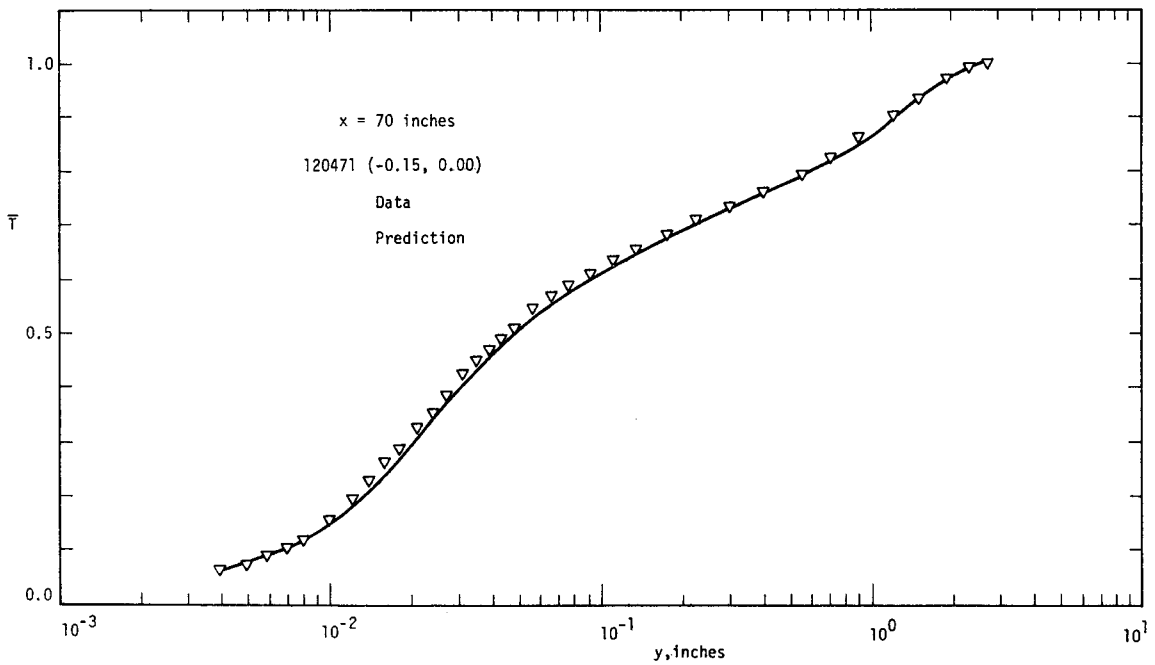


Figure 7-8 Comparison of predicted temperature profile with experimental data, run 120471

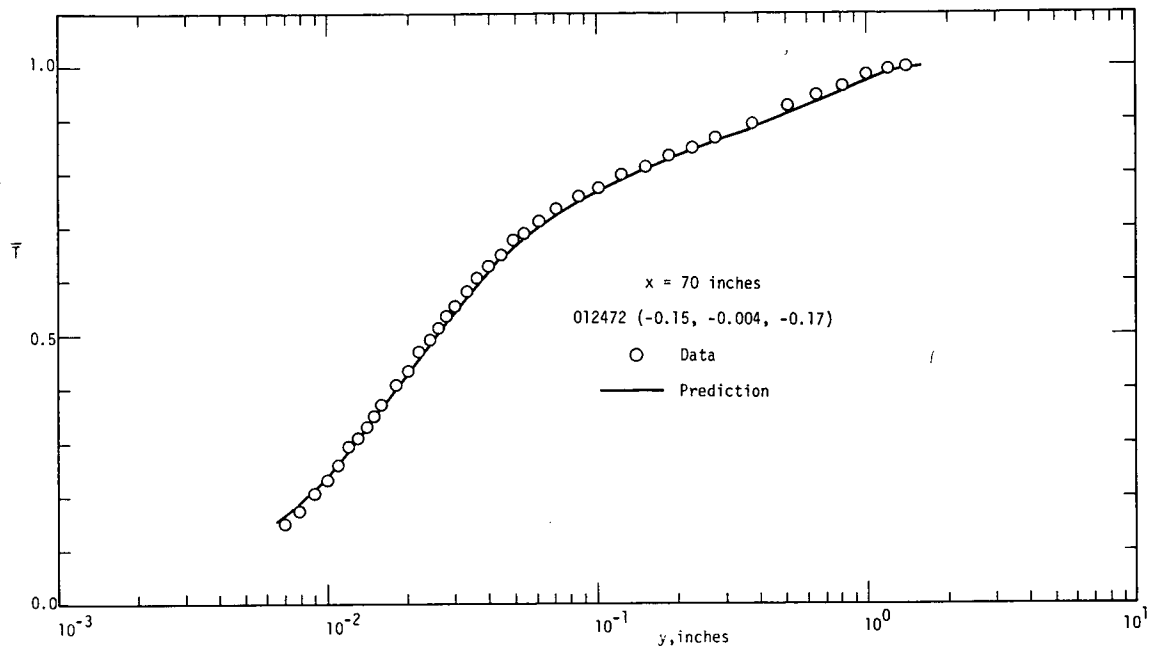


Figure 7-9 Comparison of predicted temperature profile with experimental data, run 012472

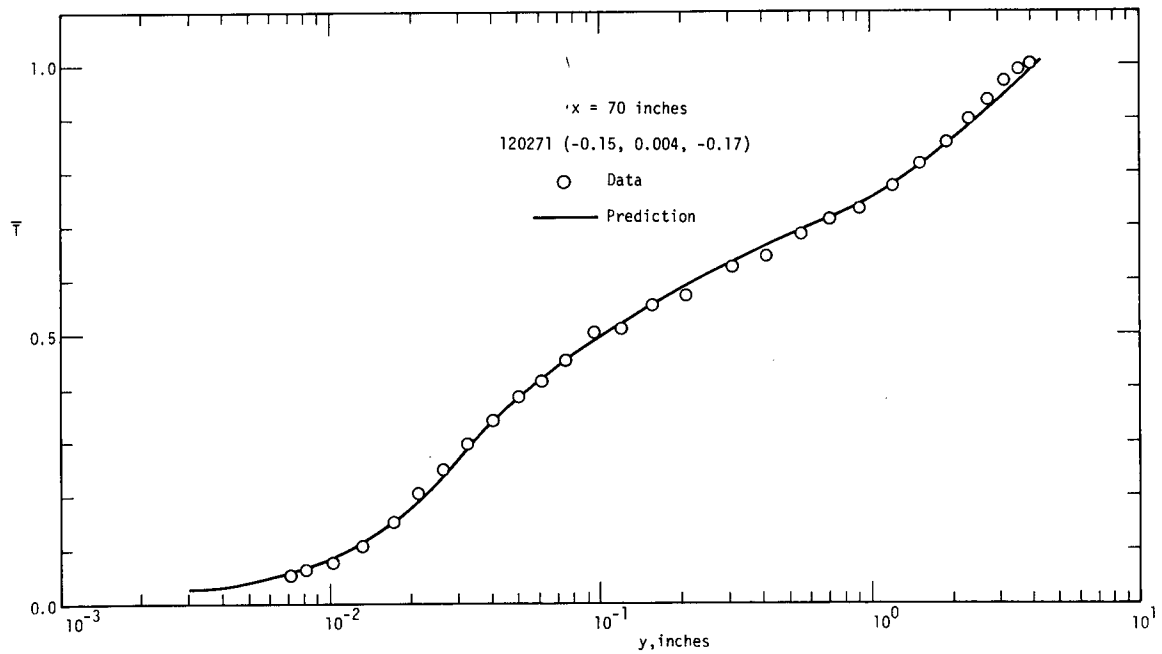


Figure 7-10 Comparison of predicted temperature profile with experimental data, run 120271

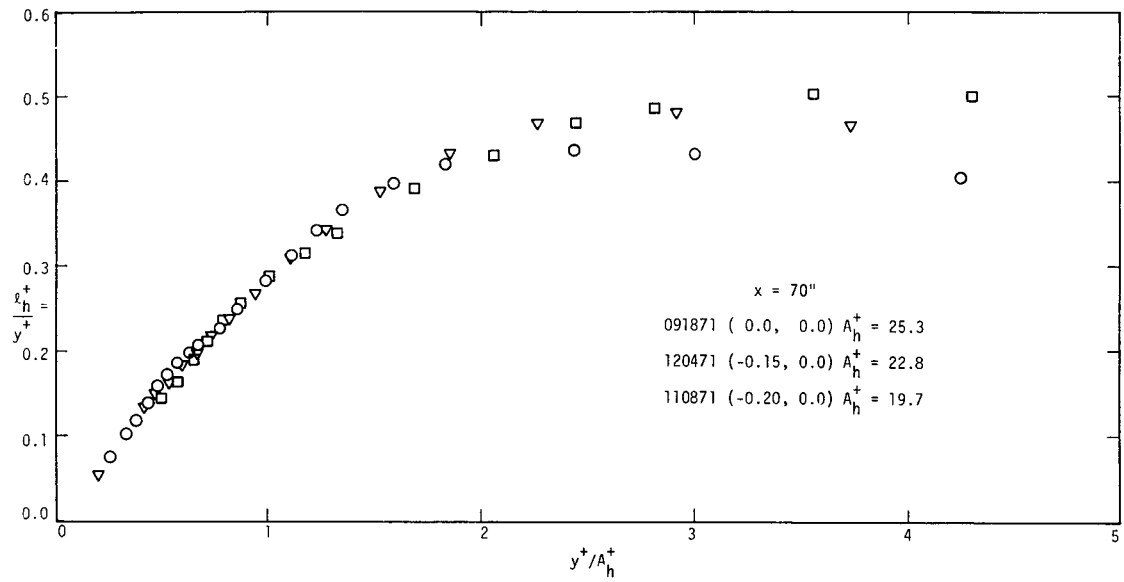


Figure 7-11 Influence of pressure gradient on heat transfer mixing length

CHAPTER 8

SUMMARY

The heat transfer behavior of the near equilibrium transpired turbulent boundary layer in an adverse pressure gradient has been studied experimentally using a total of 15 different combinations of pressure gradient and transpiration boundary conditions. Stanton numbers were measured by an energy balance technique while mean temperature profiles were measured by a 0.003 inch diameter Chromel/constantan thermocouple. The free stream velocity and transpiration boundary conditions of this study can be characterized by:

$$u_{\infty} \sim x^m, \quad m < 0 \quad (8-1)$$

and

$$F \sim F_1 x^{m_F}, \quad m_F = m_F(m) \quad (8-2)$$

The values of (m, F_1, m_F) are tabulated in Table 2-2. It was experimentally determined that for a given m and $m_F \neq 0$, the heat transfer parameter $B_h = F/St$ was a constant for a given run.

By comparing the adverse pressure gradient data of this study with the zero pressure gradient data of Moffat [2], it was concluded that mild adverse pressure gradients do not substantially alter the Stanton number-enthalpy thickness Reynolds number relationship (for a given transpiration rate). The extreme blowing and suction runs showed the greatest difference between zero pressure gradient and adverse pressure gradient. If the transpiration rate changes slowly as in this study, then the Stanton number for a given adverse pressure gradient (i.e. given m) is a function of B_h only. This functional relationship is of the form

$$\frac{St}{St_0} = f(B_h) \quad (8-3)$$

where St_0 is the Stanton number at the same value of m and Re_{Δ_2} but with $F = 0$.

Various investigators have reported that a law-of-the-wall exists for the velocity boundary layer with adverse pressure gradients and no transpiration. The data of this study indicates that an analogous law-of-the-wall for the thermal boundary layer does not exist.

The concept of an equilibrium thermal boundary layer was introduced in CHAPTER 2. It is characterized by outer layer similarity in terms of $I_{\infty}^+ - I^+$ as a function of y/Δ_3 where Δ_3 is an integral thickness of the thermal layer. A shape factor that characterizes this outer layer enthalpy defect similarity was introduced and is defined by

$$G_h = \frac{\int_0^{\infty} (I_{\infty}^+ - I^+)^2 dy}{\int_0^{\infty} (I_{\infty}^+ - I^+) dy} \quad (8-4)$$

For all of the flows studied, G_h was approximately constant for a given run except for the profiles close to the beginning of the test section. This was attributed to the fact that the momentum boundary layer originated upstream of the thermal boundary layer.

Shear stress, heat flux and turbulent Prandtl number profiles were computed from mean velocity and temperature profiles. It was concluded that the turbulent Prandtl number is greater than unity close to the wall and decreases continuously to approximately 0.5 at the free stream. Adverse pressure gradient has more of an effect on the turbulent Prandtl number than does transpiration. An adverse pressure gradient decreases the turbulent Prandtl number in the log-region.

A turbulent Prandtl number model was proposed and used in a finite difference computer program that solves the continuity, momentum, and energy equations. The inner region Pr_t model was

$$Pr_t = C_1 \frac{\phi}{1 - e^{-\phi}}, \quad \phi = \frac{0.5}{\frac{\epsilon_m}{\nu} Pr} \quad (8-5)$$

where

$$C_1 = 0.8(\gamma + 2)^{0.17}, \quad \gamma = K \times 10^3 \text{Re}_\theta / (H-1) \quad (8-6)$$

while the outer region model was

$$\text{Pr}_t = 0.5 + b_1 [1 - (y/\delta)^2] \quad (8-7)$$

with the constant b_1 being determined from continuity of (8-5) and (8-7). Four representative cases were predicted using the above turbulent Prandtl number model and a mixing-length momentum transfer model proposed by Andersen [9]. In all cases, the Stanton number predictions were within the experimental uncertainty of the data.

CHAPTER 9

TABULATION OF EXPERIMENTAL DATA

All the experimental Stanton numbers and mean temperature profiles of this study are tabulated in this chapter. The Stanton number data will be presented in Section 9.1 and the mean temperature profiles in Section 9.2. The order in which the runs are tabulated (in both sections) is given in Table 9.1.

Date	m	F_1	m_F
<u>F = 0</u>			
091871	0.00	0.000	0.00
120471	-0.15	0.000	0.00
110871	-0.20	0.000	0.00
<u>F > 0</u>			
092972	-0.15	0.001	0.00
101571	-0.15	0.002	0.00
102271	-0.15	0.004	0.00
111471	-0.15	0.001	-0.17
111871	-0.15	0.002	-0.17
120271	-0.15	0.004	-0.17
<u>F < 0</u>			
013072	-0.15	-0.001	0.00
122171	-0.15	-0.002	0.00
122371	-0.15	-0.004	0.00
011072	-0.15	-0.001	-0.17
011772	-0.15	-0.002	-0.17
012472	-0.15	-0.004	-0.17

Table 9-1: Order of data tabulation

9.1 Experimental Stanton Number Tabulation

As pointed out in Section 4.3, two different Stanton number runs were taken. Both runs are tabulated in this section under the heading Run 1 and Run 2. With the aid of the nomenclature below, the data tabulation should be self explanatory.

Special Nomenclature

<u>Symbol</u>	<u>Explanation</u>	<u>Units</u>
BH	= $F/STNA$ ($B_h = F/St$)	-
F	= $\dot{m}''/\rho_\infty u_\infty$	-
PBAR	barometric pressure	in Hg
PL	plate number	-
RE	Re_{Δ_2} , enthalpy thickness Reynolds number (see Eq. 3-20)	-
RHUM	relative humidity	-
SBH	= $F/STNO$ ($b_h = F/St_o$)	-
STN	experimental Stanton no.	-
STNA	average Stanton number (see Sec. 4.3 and Eq. 4-2)	-
STNE	Stanton number from energy integral equation	-
STNO	Stanton number for $m = -.15$, $F = 0$, $St_o = 0.0147 Re_{\Delta_2}^{-0.25}$	-
TAMB	ambient temperature	°F
TBASE	casting base temperature	°F
TCOV	wind tunnel cover (top) temperature	°F

<u>Symbol</u>	<u>Explanation</u>	<u>Units</u>
TGAS	free stream static temperature at $x = 10$ inches	°F
T0	plate temperature	°F
UINF	u_{∞} , free stream velocity	ft/sec
X	x-location	in

DATE = 092971 (-0.15, 9.001)

Table with columns PL, X, UINF, TO, F, STN, STNA, RE, STNE, STNA/STNO, 9H, S9H, STN, F, TO, UINF, X, PL. Includes sub-headers TAMB=75.5, TBASE=76.2, TGAS=72.0, TCOV=75.4, PBAR=29.79, RHUM=.47 and TAMB=64.7, TBASE=76.1, TGAS=72.0, TCOV=72.5, PBAR=29.79, RHUM=.52.

DATE = 101571 (-0.15, 9.002)

Table with columns PL, X, UINF, TO, F, STN, STNA, RE, STNE, STNA/STNO, 9H, S9H, STN, F, TO, UINF, X, PL. Includes sub-headers TAMB=71.0, TBASE=70.7, TGAS=67.8, TCOV=70.4, PBAR=29.81, RHUM=.47 and TAMB=70.4, TBASE=71.8, TGAS=68.3, TCOV=69.9, PBAR=29.81, RHUM=.50.

DATE = 112271 (-0.15, 9.004)

Table with columns PL, X, UINF, TO, F, STN, STNA, RE, STNE, STNA/STNO, 9H, S9H, STN, F, TO, UINF, X, PL. Includes sub-headers TAMB=71.2, TBASE=73.4, TGAS=69.2, TCOV=71.3, PBAR=30.06, RHUM=.57 and TAMB=70.3, TBASE=71.8, TGAS=68.9, TCOV=70.2, PBAR=30.06, RHUM=.58.

9.2 Mean Temperature Profile Tabulation

Special Nomenclature

<u>Symbol</u>	<u>Explanation</u>	<u>Units</u>
BETA	β	-
CF/2	$C_f/2$	-
DEL2	Δ_2	in
DEL3	Δ_3	in
DEL4	Δ_4	in
DELH	Δ	in
DELM	δ	in
GAM	$\gamma = - K \times 10^3 Re_\theta / (H-1)$	-
GH	G_h	-
H	H	-
-ID	$- I_d^+$	-
K(E06)	$K \times 10^6$	-
PLATE	plate number	-
Q+	Q^+	-
REH	Re_{Δ_2}	-
REM	Re_θ	-
STNA	St (see Section 9.1)	-
T	T	°F
T+	T^+	-
TAU+	τ^+	-

<u>Symbol</u>	<u>Explanation</u>	<u>Units</u>
T RUN	date of temperature run	-
U	u	ft/sec
U+	u^+	-
UINF	u_{∞}	ft/sec
V RUN	date of velocity run	-
X	x	in
Y	y	in
Y+	y^+	-

DATE = 091871 (0.00, 0.000)
T RUN = 91871-1 STNA = .00228 DELM = .189 REM = 170.0
V RUN = 120771-1 CF/2 = .00249 DELM = .287 REM = 935.0
PLATE = 1 UINF = 31.6 DEL2 = .0107 DEL3 = .257
X(IN) = 2.00 GH = 4.702 THETA = .0324 DEL4 = 1.208
K(E06) = .0014 GAM = .001 BETA = -.000 H = 1.563

DATE = 091871 (0.00, 0.000)
T RUN = 91871-1 STNA = .00229 DELM = .194 REM = 560.0
V RUN = 120771-1 CF/2 = .00222 DELM = .422 REM = 916.0
PLATE = 3 UINF = 31.9 DEL2 = .0393 DEL3 = .880
X(IN) = 10.00 GH = 5.145 THETA = .0314 DEL4 = 1.520
K(E06) = .0012 GAM = .002 BETA = -.001 H = 1.931

Table with columns I, Y+, U+, T+, V/DEL3, -I0, Y, T, TAU+, O+. Rows 1-36 showing data points for the first set of parameters.

Table with columns I, Y+, U+, T+, V/DEL3, -I0, Y, U, T, TAU+, O+. Rows 1-36 showing data points for the second set of parameters.

DATE = 091871 (0.00, 0.000)
T RUN = 91871-1 STNA = .00251 DELM = .626 REM = 1030.0
V RUN = 120771-1 CF/2 = .00202 DELM = .824 REM = 1204.0
PLATE = 6 UINF = 31.6 DEL2 = .0164 DEL3 = 1.726
X(IN) = 22.00 GH = 5.352 THETA = .0758 DEL4 = 9.242
K(E06) = .0009 GAM = .002 BETA = -.001 H = 1.534

DATE = 091871 (0.00, 0.000)
T RUN = 91871-1 STNA = .00229 DELM = .628 REM = 1450.0
V RUN = 120771-1 CF/2 = .00190 DELM = .745 REM = 1536.0
PLATE = 6 UINF = 31.6 DEL2 = .0164 DEL3 = 1.726
X(IN) = 34.00 GH = 5.528 THETA = .0964 DEL4 = 13.819
K(E06) = .0006 GAM = .002 BETA = -.001 H = 1.506

Table with columns I, Y+, U+, T+, V/DEL3, -I0, Y, T, TAU+, O+. Rows 1-45 showing data points for the third set of parameters.

Table with columns I, Y+, U+, T+, V/DEL3, -I0, Y, U, T, TAU+, O+. Rows 1-45 showing data points for the fourth set of parameters.

Reproduced from best available copy.

Table with columns: DATE = 091871 (0.00, 0.000), T RUN = 91871-1, STMA = .00216, DELM = 1.037, REM = 1670.0, V RUN = 120771-1, CF/2 = .00181, DELM = 1.889, REM = 162.0, PLATE = 12, UINF = 31.6, DEL2 = .1175, DEL3 = 3.68, X(IN) = 46.00, GM = 5.633, THETA = .1170, DEL4 = 16.388, K(EO6) = .0001, GAM = .001, BETA = -.0003, H = 1.505. Header: I Y+ U+ T+ V/D/EL3 -ID Y U T TAU+ Q+ I Y+ U+ T+ V/D/EL3 -ID Y U T TAU+ Q+. Rows 1-46.

Table with columns: DATE = 091871 (0.00, 0.000), T RUN = 91871-1, STMA = .00200, DELM = 1.417, REM = 2648.0, V RUN = 120771-1, CF/2 = .00166, DELM = 1.276, REM = 2481.0, PLATE = 18, UINF = 31.6, DEL2 = .1665, DEL3 = 4.715, X(IN) = 70.00, GM = 5.759, THETA = .1560, DEL4 = 27.114, K(EO6) = -.0009, GAM = -.0005, BETA = .002, H = 1.450. Header: I Y+ U+ T+ V/D/EL3 -ID Y U T TAU+ Q+ I Y+ U+ T+ V/D/EL3 -ID Y U T TAU+ Q+. Rows 1-46.

DATE = 091971 (0.00, 0.000)

T RUN = 91871-1 STNA = .00191 DELM = 1.003 REM = 3180.0
V RUN = 120771-1 CF/2 = .00161 DELM = 1.003 REM = 2971.0
PLATE = 23 UINF = 31.8 DEL2 = 2003 DEL3 =
X(TIN) = 90.00 GM = 5.749 THETA = .1871 DEL4 = 33.008
K(E06) = -.0020 GAM = -.012 BETA = .006 M = 1.470

Table with columns I, Y+, U+, T+, V/DEL3, -ID, Y, U, T. Rows 1-40 showing data points for date 091971.

DATE = 120471 (-0.15, 0.000)

T RUN = 120471-1 STNA = .00316 DELM = .449 REM = 511.0
V RUN = 71571-5 CF/2 = .00198 DELM = .515 REM = 985.0
PLATE = 3 UINF = 26.5 DEL2 = .0369 DEL3 = .912
X(TIN) = 10.00 GM = 4.492 THETA = .0711 DEL4 = 4.099
K(E06) = -.0670 GAM = -1.374 BETA = .061 M = 1.622

Table with columns I, Y+, U+, T+, V/DEL3, -ID, Y, U, T, TAU+, Q+. Rows 1-30 showing data points for date 120471.

Table with columns I, Y+, U+, T+, V/DEL3, -ID, Y, U, T, TAU+, Q+. Rows 31-40 showing data points for date 120471.

DATE = 120471 (-0.15, 0.000)

T RUN = 120471-1 STNA = .00444 DELM = .144 REM = 144.0
V RUN = 71571-5 CF/2 = .00271 DELM = .219 REM = 944.0
PLATE = 1 UINF = 29.4 DEL2 = .0094 DEL3 = .245
X(TIN) = 2.00 GM = 4.806 THETA = .0094 DEL4 = 1.178
K(E06) = -.4400 GAM = -.433 BETA = .146 M = 1.578

Table with columns I, Y+, U+, T+, V/DEL3, -ID, Y, U, T. Rows 1-40 showing data points for date 120471.

DATE = 120471 (-0.15, 0.000)

T RUN = 120471-1 STNA = .00264 DELM = .820 REM = 909.0
V RUN = 71571-5 CF/2 = .00169 DELM = .903 REM = 1545.0
PLATE = 6 UINF = 24.1 DEL2 = .0721 DEL3 = 1.947
X(TIN) = 22.00 GM = 4.452 THETA = .1226 DEL4 = 5.226
K(E06) = -.4950 GAM = -1.241 BETA = .720 M = 1.504

Table with columns I, Y+, U+, T+, V/DEL3, -ID, Y, U, T, TAU+, Q+. Rows 1-30 showing data points for date 120471.

Table with columns I, Y+, U+, T+, V/DEL3, -ID, Y, U, T, TAU+, Q+. Rows 31-40 showing data points for date 120471.

Table with columns I, Y+, U+, T+, V/DEL3, -ID, Y, U, T, TAU+, Q+. Rows 41-42 showing data points for date 120471.

DATE = 120471 (-0.15, 0.000)

T RUN = 120471-1 STNA = .00244 DELM = 1.168 REM = 1276.0
V RUN = 71571-5 CF/2 = .00153 DELM = 1.175 REM = 2008.0
PLATE = 9 UINF = 22.9 DEL2 = 1.068 DEL3 = 2.714
X(IN) = 34.00 GM = 4.361 THETA = .1691 DEL4 = 11.839
K(EO6) = -.3480 GAH = -1.200 BETA = .721 H = 1.582

Table with columns I, Y+, U+, T+, V/DEL3, -ID, Y, U, T, TAU+, Q+, I, Y+, U+, T+, V/DEL3, -ID, Y, U, T, TAU+, Q+. Rows 1-39.

DATE = 120471 (-0.15, 0.000)

T RUN = 120471-1 STNA = .00271 DELM = 1.532 REM = 1602.0
V RUN = 71571-5 CF/2 = .00145 DELM = 1.503 REM = 2460.0
PLATE = 12 UINF = 21.6 DEL2 = 1.404 DEL3 = 3.631
X(IN) = 46.00 GM = 4.373 THETA = -.2156 DEL4 = 15.878
K(EO6) = -.2740 GAH = -1.193 BETA = .714 H = 1.585

Table with columns I, Y+, U+, T+, V/DEL3, -ID, Y, U, T, TAU+, Q+, I, Y+, U+, T+, V/DEL3, -ID, Y, U, T, TAU+, Q+. Rows 1-39.

DATE = 120471 (-0.15, 0.000)

T RUN = 120471-1 STNA = .00222 DELM = 1.824 REM = 1872.0
V RUN = 71571-5 CF/2 = .00140 DELM = 1.737 REM = 2917.0
PLATE = 15 UINF = 21.1 DEL2 = 1.700 DEL3 = 4.410
X(IN) = 56.00 GM = 4.364 THETA = .2559 DEL4 = 19.245
K(EO6) = -.2280 GAH = -1.140 BETA = .724 H = 1.563

Table with columns I, Y+, U+, T+, V/DEL3, -ID, Y, U, T, TAU+, Q+, I, Y+, U+, T+, V/DEL3, -ID, Y, U, T, TAU+, Q+. Rows 1-39.

DATE = 120471 (-0.15, 0.000)

T RUN = 120471-1 STNA = .00215 DELM = 2.150 REM = 2165.0
V RUN = 71571-5 CF/2 = .00136 DELM = 2.121 REM = 3229.0
PLATE = 18 UINF = 20.5 DEL2 = 2.022 DEL3 = 5.297
X(IN) = 70.00 GM = 4.376 THETA = .3115 DEL4 = 23.180
K(EO6) = -.1960 GAH = -1.137 BETA = .735 H = 1.557

Table with columns I, Y+, U+, T+, V/DEL3, -ID, Y, U, T, TAU+, Q+, I, Y+, U+, T+, V/DEL3, -ID, Y, U, T, TAU+, Q+. Rows 1-39.

DATE = 110871 (-0.20, 0.000)

T RUN = 110871-1 STNA = .00218 DELM = 2.621 REM = 2055.0
V RUN = 110971-1 CF/2 = .00141 DELM = 2.527 REM = 3699.0
PLATE = 18 UINF = 15.2 DEL2 = 2.154 DEL3 = 5.325
X(IN) = 70.00 GH = 3.645 THETA = 3.966 DEL4 = 19.407
K(E06) = -.2820 GAM = -1.637 BETA = 1.527 H = 1.670

Table with 14 columns: I, Y+, U+, T+, V/DOL3, -IO, Y, U, T, TAU+, Q+, I, Y+, U+, T+, V/DOL3, -IO, Y, U, T, TAU+, Q+. Rows 1-40 showing various data points.

DATE = 110971 (-0.20, 0.000)

T RUN = 110871-1 STNA = .00218 DELM = 3.125 REM = 2289.0
V RUN = 110971-1 CF/2 = .00103 DELM = 2.979 REM = 4139.0
PLATE = 21 UINF = 17.7 DEL2 = .2516 DEL3 = 6.276
X(IN) = 52.00 GH = 3.645 THETA = 4.949 DEL4 = 21.542
K(E06) = -.2490 GAM = -1.665 BETA = 1.595 H = 1.619

Table with 14 columns: I, Y+, U+, T+, V/DOL3, -IO, Y, U, T, TAU+, Q+, I, Y+, U+, T+, V/DOL3, -IO, Y, U, T, TAU+, Q+. Rows 1-40 showing various data points.

DATE = 110971 (-0.20, 0.000)

T RUN = 110871-1 STNA = .00209 DELM = 2.459 REM = 2511.0
V RUN = 110971-1 CF/2 = .00101 DELM = 3.157 REM = 4533.0
PLATE = 23 UINF = 17.2 DEL2 = .2937 DEL3 = 6.979
X(IN) = 90.00 GH = 3.548 THETA = 5.122 DEL4 = 24.622
K(E06) = -.2420 GAM = -1.727 BETA = 1.722 H = 1.632

Table with 14 columns: I, Y+, U+, T+, V/DOL3, -IO, Y, U, T, TAU+, Q+, I, Y+, U+, T+, V/DOL3, -IO, Y, U, T, TAU+, Q+. Rows 1-40 showing various data points.

DATE = 092971 (-0.15, 0.001)

T RUN = 92971-1 STNA = .00420 DELM = .162 REM = 166.0
V RUN = 91771-2 CF/2 = .00249 DELM = .319 REM = 556.0
PLATE = 1 UINF = 29.7 DEL2 = .0311 DEL3 = .291
X(IN) = 2.00 GH = 4.800 THETA = .0372 DEL4 = 1.398
K(E06) = -.4670 GAM = -.416 BETA = .169 H = 1.624

Table with 14 columns: I, Y+, U+, T+, V/DOL3, -IO, Y, U, T, TAU+, Q+, I, Y+, U+, T+, V/DOL3, -IO, Y, U, T, TAU+, Q+. Rows 1-40 showing various data points.

DATE = 092971 (-0.15, 0.001)

T RUN = 92971-1 STNA = J0179 DELM = 2.150 REM = 2287.0
V RUN = 91771-2 CP/2 = J00096 DELM = 2.173 REM = 3510.0
PLATE = 15 UINF = 21.40 DEL2 = 2.122 DEL3 = 8.184
X(IN) = 58.00 GM = 4.430 THETA = J257 DEL4 = 29.191
K(EO6) = -2270 GAM = -1.191 BETA = 1.343 M = 1.669

Table with columns I, Y+, U+, T+, V/OEL3, -ID, Y, U, T, YAU+, Q+, and data rows 1-43.

DATE = 92971 (-0.15, 0.001)

T RUN = 92971-1 STNA = J0171 DELM = 2.557 REM = 2669.0
V RUN = 91771-2 CP/2 = J00096 DELM = 2.527 REM = 4014.0
PLATE = 19 UINF = 21.90 DEL2 = 2.258 DEL3 = 7.274
X(IN) = 70.00 GM = 4.421 THETA = J261 DEL4 = 29.067
K(EO6) = -1930 GAM = -1.167 BETA = 1.327 M = 1.664

Table with columns I, Y+, U+, T+, V/OEL3, -ID, Y, U, T, YAU+, Q+, and data rows 1-43.

DATE = 092971 (-0.15, 0.001)

T RUN = 92971-1 STNA = J0165 DELM = 2.882 REM = 2915.0
V RUN = 91771-2 CP/2 = J00096 DELM = 2.903 REM = 4541.0
PLATE = 21 UINF = 20.50 DEL2 = 2.205 DEL3 = 9.242
X(IN) = 92.00 GM = 4.442 THETA = J442 DEL4 = 39.912
K(EO6) = -1690 GAM = -1.188 BETA = 1.416 M = 1.646

Table with columns I, Y+, U+, T+, V/OEL3, -ID, Y, U, T, YAU+, Q+, and data rows 1-43.

DATE = 092971 (-0.15, 0.001)

T RUN = 92971-1 STNA = J0162 DELM = 3.265 REM = 3173.0
V RUN = 91771-2 CP/2 = J00096 DELM = 3.164 REM = 4875.0
PLATE = 23 UINF = 20.10 DEL2 = 2.312 DEL3 = 9.132
X(IN) = 98.00 GM = 4.446 THETA = J483 DEL4 = 44.254
K(EO6) = -1640 GAM = -1.243 BETA = 1.511 M = 1.643

Table with columns I, Y+, U+, T+, V/OEL3, -ID, Y, U, T, YAU+, Q+, and data rows 1-43.

Reproduced from best available copy.

DATE = 101571 (-0.15, 0.002)

T RUN = 101571-2 STNA = .00376 DELM = .163 REM = 181.0
V RUN = 101371-2 CFZ2 = .00229 DELM = .321 REM = 597.0
PLATE = 1 UINF = 29.7 DEL2 = .0120 DEL3 = .736
X(IN) = 2.00 GH = 5.165 THETA = .0387 DEL4 = 1.775
K(E06) = -.4540 GAM = -.421 BETA = .191 H = 1.633

Table with columns I, Y+, U+, T+, V/DEL3, -IO, Y, U, T. Rows 1-37 showing numerical data for the first set of parameters.

DATE = 101571 (-0.15, 0.002)

T RUN = 101571-2 STNA = .00231 DELM = .549 REM = 699.0
V RUN = 101371-2 CFZ2 = .00152 DELM = .577 REM = 1198.0
PLATE = 3 UINF = 26.9 DEL2 = .0510 DEL3 = 1.930
X(IN) = 10.00 GH = 5.668 THETA = .0874 DEL4 = 8.957
K(E06) = -.8550 GAM = -1.376 BETA = 1.100 H = 1.745

Table with columns I, Y+, U+, T+, V/DEL3, -IO, Y, U, T, TAU+, O+. Rows 1-37 showing numerical data for the second set of parameters.

DATE = 101571 (-0.15, 0.002)

T RUN = 101571-2 STNA = .00192 DELM = 1.244 REM = 1324.0
V RUN = 101371-2 CFZ2 = .00103 DELM = 1.034 REM = 2048.0
PLATE = 6 UINF = 28.4 DEL2 = .1083 DEL3 = 3.328
X(IN) = 22.00 GH = 5.955 THETA = .1645 DEL4 = 19.675
K(E06) = -.4770 GAM = -1.250 BETA = 1.940 H = 1.711

Table with columns I, Y+, U+, T+, V/DEL3, -IO, Y, U, T, TAU+, O+. Rows 1-37 showing numerical data for the third set of parameters.

DATE = 101571 (-0.15, 0.002)

T RUN = 101571-2 STNA = .00161 DELM = 1.512 REM = 1934.0
V RUN = 101371-2 CFZ2 = .00076 DELM = 1.503 REM = 2914.0
PLATE = 9 UINF = 23.1 DEL2 = .1557 DEL3 = 4.799
X(IN) = 34.00 GH = 5.411 THETA = .2305 DEL4 = 26.067
K(E06) = -.3420 GAM = -1.232 BETA = 2.015 H = 1.711

Table with columns I, Y+, U+, T+, V/DEL3, -IO, Y, U, T, TAU+, O+. Rows 1-37 showing numerical data for the fourth set of parameters.

DATE = 101571 (-0.15, 0.002)

T RUN = 101571-2 STNA = .00147 DELM = 2.008 REM = 234.0
V RUN = 101371-2 CF72 = .00074 DELM = 1.941 REM = 352.0
PLATE = 12 UINF = 22.2 DEL2 = 2.047 DEL3 = 6.450
X(IN) = 46.0 GM = 5.800 Y(MTA) = 3.120 DEL4 = 35.961
K(E06) = -26.00 GAM = -1.214 HETA = 2.174 M = 1.778

Table with columns I, Y+, U+, T+, V/DEL3, -ID, Y, U, T, TAU+, Q+, containing numerical data for various parameters.

Table with columns I, Y+, U+, T+, V/DEL3, -ID, Y, U, T, TAU+, Q+, containing numerical data for various parameters.

Table with columns I, Y+, U+, T+, V/DEL3, -ID, Y, U, T, TAU+, Q+, containing numerical data for various parameters.

Table with columns I, Y+, U+, T+, V/DEL3, -ID, Y, U, T, TAU+, Q+, containing numerical data for various parameters.

DATE = 101571 (-0.15, 0.002)

T RUN = 101571-2 STNA = .00130 DELM = 2.905 REM = 318.0
V RUN = 101371-2 CF72 = .00062 DELM = 2.824 REM = 423.0
PLATE = 18 UINF = 20.9 DEL2 = 2.290 DEL3 = 9.859
X(IN) = 70.0 GM = 5.601 Y(MTA) = 4.529 DEL4 = 59.218
K(E06) = -4.990 GAM = -1.210 HETA = 2.401 M = 1.754

Table with columns I, Y+, U+, T+, V/DEL3, -ID, Y, U, T, TAU+, Q+, containing numerical data for various parameters.

Table with columns I, Y+, U+, T+, V/DEL3, -ID, Y, U, T, TAU+, Q+, containing numerical data for various parameters.

Table with columns I, Y+, U+, T+, V/DEL3, -ID, Y, U, T, TAU+, Q+, containing numerical data for various parameters.

Table with columns I, Y+, U+, T+, V/DEL3, -ID, Y, U, T, TAU+, Q+, containing numerical data for various parameters.

DATE = 101571 (-0.15, 0.002)

T RUN = 101571-2 STNA = .00137 DELM = 2.475 REM = 276.0
V RUN = 101371-2 CF72 = .00084 DELM = 2.374 REM = 374.0
PLATE = 15 UINF = 21.4 DEL2 = 2.529 DEL3 = 3.122
X(IN) = 56.0 GM = 5.582 Y(MTA) = 3.120 DEL4 = 45.956
K(E06) = -2.220 GAM = -1.211 HETA = 2.251 M = 1.765

Table with columns I, Y+, U+, T+, V/DEL3, -ID, Y, U, T, TAU+, Q+, containing numerical data for various parameters.

Table with columns I, Y+, U+, T+, V/DEL3, -ID, Y, U, T, TAU+, Q+, containing numerical data for various parameters.

Table with columns I, Y+, U+, T+, V/DEL3, -ID, Y, U, T, TAU+, Q+, containing numerical data for various parameters.

Table with columns I, Y+, U+, T+, V/DEL3, -ID, Y, U, T, TAU+, Q+, containing numerical data for various parameters.

DATE = 101571 (-0.15, 0.002)

T RUN = 101571-2 STNA = .00124 DELM = 3.361 REM = 361.0
V RUN = 101371-2 CF72 = .00058 DELM = 3.259 REM = 54.90
PLATE = 21 UINF = 20.5 DEL2 = 3.362 DEL3 = 11.452
X(IN) = 82.0 GM = 5.627 Y(MTA) = 5.266 DEL4 = 64.452
K(E06) = -1.650 GAM = -1.247 HETA = 2.554 M = 1.774

Table with columns I, Y+, U+, T+, V/DEL3, -ID, Y, U, T, TAU+, Q+, containing numerical data for various parameters.

Table with columns I, Y+, U+, T+, V/DEL3, -ID, Y, U, T, TAU+, Q+, containing numerical data for various parameters.

Table with columns I, Y+, U+, T+, V/DEL3, -ID, Y, U, T, TAU+, Q+, containing numerical data for various parameters.

Table with columns I, Y+, U+, T+, V/DEL3, -ID, Y, U, T, TAU+, Q+, containing numerical data for various parameters.

DATE = 101571 (-0.15, 0.002)

T RUN = 101571-2 STNA = .00126 DELM = 3.806 REM = 3966.0
V RUN = 101371-2 CF/2 = .00357 DELM = 3.614 REM = 5904.0
PLATE = 23 UNF = 2.71 DEL2 = .3495 DEL3 = 12.919
X(IN) = 90.00 GM = 5.679 THETA = 5.337 DEL4 = 73.371
K(E06) = -1.590 GAM = -1.293 BETA = 2.449 H = 1.726

Table with columns I, Y+, U+, T+, V/DEL3, -ID, Y, U, T. Rows 1-40 showing data points for date 101571.

DATE = 102271 (-0.15, 0.006)

T RUN = 102271-1 STNA = .00280 DELM = .167 REM = 224.0
V RUN = 102171-1 CF/2 = .00194 DELM = .330 REM = 627.0
PLATE = 6 UNF = 29.6 DEL2 = .0148 DEL3 = .515
X(IN) = 22.00 GM = 6.419 THETA = .0414 DEL4 = 3.305
K(E06) = -4.950 GAM = -4.44 BETA = .251 H = 1.706

Table with columns I, Y+, U+, T+, V/DEL3, -ID, Y, U, T. Rows 1-40 showing data points for date 102271.

DATE = 102271 (-0.15, 0.004)

T RUN = 102271-1 STNA = .00165 DELM = .624 REM = 980.0
V RUN = 102171-1 CF/2 = .00073 DELM = .649 REM = 1440.0
PLATE = 3 UNF = 26.4 DEL2 = .0640 DEL3 = 2.075
X(IN) = 10.00 GM = 5.926 THETA = 1.048 DEL4 = 12.294
K(E06) = -0.890 GAM = -1.761 BETA = 2.961 H = 1.910

Table with columns I, Y+, U+, T+, V/DEL3, -ID, Y, U, T, TAU+, Q+. Rows 1-40 showing data points for date 102271.

DATE = 102271 (-0.15, 0.004)

T RUN = 102271-1 STNA = .00188 DELM = 1.257 REM = 1672.0
V RUN = 102171-1 CF/2 = .00042 DELM = 1.276 REM = 2700.0
PLATE = 6 UNF = 24.4 DEL2 = .1338 DEL3 = 5.261
X(IN) = 22.00 GM = 6.752 THETA = 2.160 DEL4 = 35.250
K(E06) = -4.700 GAM = -1.215 BETA = 5.155 H = 2.044

Table with columns I, Y+, U+, T+, V/DEL3, -ID, Y, U, T, TAU+, Q+. Rows 1-40 showing data points for date 102271.

DATE = 102271 (-0.15, 0.004)																				DATE = 102271 (-0.15, 0.004)																																		
T RUN	V RUN	PLATE	X(IN)	K(E06)	STNA	CF2	UINF	GM	GAM	DELTA	BETA	DELTA	DELTA	DELTA	DELTA	DELTA	DELTA	DELTA	DELTA	DELTA	I	Y	U	T	TAU	Q	T RUN	V RUN	PLATE	X(IN)	K(E06)	STNA	CF2	UINF	GM	GAM	DELTA	BETA	DELTA	DELTA	DELTA	DELTA	DELTA	DELTA	DELTA	DELTA	DELTA	DELTA	I	Y	U	T	TAU	Q
1	1	1	1	1	1	1	1	1	1	1	1	1	1	1	1	1	1	1	1	1	1	1	1	1	1	1	1	1	1	1	1	1	1	1	1	1	1	1	1	1	1	1	1	1										

DATE = 102271 (-0.15, 0.004)																				DATE = 102271 (-0.15, 0.004)																																		
T RUN	V RUN	PLATE	X(IN)	K(E06)	STNA	CF2	UINF	GM	GAM	DELTA	BETA	DELTA	DELTA	DELTA	DELTA	DELTA	DELTA	DELTA	DELTA	DELTA	I	Y	U	T	TAU	Q	T RUN	V RUN	PLATE	X(IN)	K(E06)	STNA	CF2	UINF	GM	GAM	DELTA	BETA	DELTA	DELTA	DELTA	DELTA	DELTA	DELTA	DELTA	DELTA	DELTA	DELTA	I	Y	U	T	TAU	Q
1	1	1	1	1	1	1	1	1	1	1	1	1	1	1	1	1	1	1	1	1	1	1	1	1	1	1	1	1	1	1	1	1	1	1	1	1	1	1	1	1	1	1	1	1										

DATE = 111471 (-0.15, 0.001, -0.17)

T RUN = 111471-1 STNA = .00211 DELM = 1.333 RHM = 1553.0
V RUN = 111571-1 OFI2 = .00118 DELM = 1.308 RHM = 2321.0
PLATE = 34.00 GM = 4.666 THETA = 1.959 DEL4 = 16.230
X(IN) = -3360 GAM = -1.209 BETA = 1.959 H = 1.645

Table with 11 columns: I, Y+, U+, T+, Y/DEL3, -I, Y, U, T, TAU+, Q+. Rows 1-41 showing numerical data for various parameters.

DATE = 111471 (-0.15, 0.001, -0.17)

T RUN = 111471-1 STNA = .00199 DELM = 1.766 RHM = 1937.0
V RUN = 111571-1 OFI2 = .00112 DELM = 1.696 RHM = 2173.0
PLATE = 34.00 GM = 4.666 THETA = 1.959 DEL4 = 16.230
X(IN) = -3360 GAM = -1.209 BETA = 1.959 H = 1.645

Table with 11 columns: I, Y+, U+, T+, Y/DEL3, -I, Y, U, T, TAU+, Q+. Rows 1-41 showing numerical data for various parameters.

DATE = 111471 (-0.15, 0.001, -0.17)

T RUN = 111471-1 STNA = .00190 DELM = 2.102 RHM = 2219.0
V RUN = 111571-1 OFI2 = .00108 DELM = 1.654 RHM = 3110.0
PLATE = 34.00 GM = 4.667 THETA = 1.959 DEL4 = 16.230
X(IN) = -3360 GAM = -1.143 BETA = 1.951 H = 1.631

Table with 11 columns: I, Y+, U+, T+, Y/DEL3, -I, Y, U, T, TAU+, Q+. Rows 1-41 showing numerical data for various parameters.

DATE = 111471 (-0.15, 0.001, -0.17)

T RUN = 111471-1 STNA = .00183 DELM = 2.439 RHM = 2528.0
V RUN = 111571-1 OFI2 = .00105 DELM = 1.616 RHM = 3210.0
PLATE = 34.00 GM = 4.670 THETA = 1.959 DEL4 = 16.230
X(IN) = -3360 GAM = -1.111 BETA = 1.960 H = 1.619

Table with 11 columns: I, Y+, U+, T+, Y/DEL3, -I, Y, U, T, TAU+, Q+. Rows 1-41 showing numerical data for various parameters.

DATE = 111471 (-0.15, 0.001, -0.17)
T RUN = 111471-1 STNA = .00178 DELM = 2.356 REM = 2995.0
V RUN = 111571-1 CF/2 = .00102 DELM = 2.687 REM = 4173.0
PLATE = 21 UINF = 20.3 DEL2 = .2772 DEL3 = 7.730
X(IN) = 92.00 GM = 4.699 THETA = 1.396 DEL4 = 36.327
K(EO6) = -15.60 GAM = -1.191 BETA = 1.937 M = 1.597

DATE = 111071 (-0.15, 0.002, -0.17)
T RUN = 111071-1 STNA = .00346 DELM = .168 REM = 187.0
V RUN = 111771-3 CF/2 = .00200 DELM = 2.944 REM = 592.0
PLATE = 1 UINF = 29.4 DEL2 = .0122 DEL3 = .373
X(IN) = 2.00 GM = 5.662 THETA = 0.0380 DEL4 = 2.110
K(EO6) = -4.520 GAM = -.405 BETA = .189 M = 1.649

Table with columns I, Y+, U+, T+, V/DEL3, -IO, Y, U, T. Contains data points for various runs from 1 to 40.

Table with columns I, Y+, U+, T+, V/DEL3, -IO, Y, U, T. Contains data points for various runs from 1 to 40.

DATE = 111971 (-0.15, 0.002, -0.17)
T RUN = 111971-1 STNA = .00232 DELM = .533 REM = 691.0
V RUN = 111771-3 CF/2 = .00150 DELM = .579 REM = 1196.0
PLATE = 3 UINF = 26.5 DEL2 = .0501 DEL3 = 1.529
X(IN) = 10.00 GM = 5.587 THETA = .0568 DEL4 = 5.543
K(EO6) = -.9470 GAM = -1.373 BETA = 1.114 M = 1.738

DATE = 111071 (-0.15, 0.002, -0.17)
T RUN = 111071-1 STNA = .00190 DELM = 1.043 REM = 1296.0
V RUN = 111771-3 CF/2 = .00108 DELM = 1.032 REM = 2035.0
PLATE = 6 UINF = 24.2 DEL2 = .1030 DEL3 = 3.140
X(IN) = 22.00 GM = 5.376 THETA = .1619 DEL4 = 16.991
K(EO6) = -4.720 GAM = -1.263 BETA = 1.467 M = 1.766

Table with columns I, Y+, U+, T+, V/DEL3, -IO, Y, U, T, TAU+, Q+. Contains data points for various runs from 1 to 44.

Table with columns I, Y+, U+, T+, V/DEL3, -IO, Y, U, T, TAU+, Q+. Contains data points for various runs from 1 to 44.

DATE = 111871 (-0.15, 0.002, -0.17) DATE = 111871 (-0.15, 0.002, -0.17)
T RUN = 111871-1 STNA = .00174 DELM = 1.503 REM = 1747.0
V RUN = 111771-3 CF/2 = .00087 DELM = 1.469 REM = 2679.0
PLATE = 15 UINF = 21.2 DEL2 = 1.948 DEL3 = 5.797
X(IN) = 34.00 GM = 5.107 THETA = 2.250 DEL4 = 22.279
K(E06) = -.3360 GAM = -1.213 META = 1.707 H = 1.742

Table with 13 columns: I, Y+, U+, T+, Y/DEL3, -ID, Y, U, T, TAU+, Q+, I, Y+, U+, T+, Y/DEL3, -ID, Y, U, T, TAU+, Q+. Contains two data blocks side-by-side, one for date 111871 and one for 111871.

DATE = 111871 (-0.15, 0.002, -0.17) DATE = 111871 (-0.15, 0.002, -0.17)
T RUN = 111871-1 STNA = .00158 DELM = 2.368 REM = 2614.0
V RUN = 111771-3 CF/2 = .00079 DELM = 2.305 REM = 3948.0
PLATE = 15 UINF = 21.2 DEL2 = 2.274 DEL3 = 7.051
X(IN) = 54.00 GM = 5.003 THETA = 1.695 DEL4 = 35.487
K(E06) = -.2160 GAM = -1.206 META = 1.757 H = 1.713

Table with 13 columns: I, Y+, U+, T+, Y/DEL3, -ID, Y, U, T, TAU+, Q+, I, Y+, U+, T+, Y/DEL3, -ID, Y, U, T, TAU+, Q+. Contains two data blocks side-by-side, one for date 111871 and one for 111871.

DATE = 111971 (-0.15, 0.002, -0.17)

T RUN = 111971-1 STNA = .00149 DELM = 3.213 REM = 3386.0
V RUN = 11171-3 CF/2 = .00074 DELM = 3.089 REM = 5066.0
PLATE = 21 UINF = 20.2 DEL2 = 3.222 DEL3 = 9.605
X(INI) = 82.00 GAM = 4.972 THETA = 4.421 DEL4 = 4.753
K(E06) = -1.650 GM = -1.254 BETA = 1.905 H = 1.683

Table with 13 columns: I, Y+, U+, T+, Y/DEL3, -TD, Y, U, T, TAU+, Q+. Rows 1-42 containing numerical data for DATE = 111971.

DATE = 111871 (-0.15, 0.002, -0.17)

T RUN = 111871-1 STNA = .00147 DELM = 3.500 REM = 3636.0
V RUN = 11171-3 CF/2 = .00073 DELM = 3.388 REM = 5416.0
PLATE = 23 UINF = 19.9 DEL2 = 3.358 DEL3 = 10.465
X(INI) = 90.00 GAM = 5.240 THETA = 5.240 DEL4 = 51.335
K(E06) = -1.650 GM = -1.348 BETA = 2.057 H = 1.677

Table with 13 columns: I, Y+, U+, T+, Y/DEL3, -TD, Y, U, T, TAU+, Q+. Rows 1-42 containing numerical data for DATE = 111871.

DATE = 120271 (-0.15, 0.004, -0.17)

T RUN = 120271-1 STNA = .00279 DELM = .183 REM = 215.0
V RUN = 112871-1 CF/2 = .00194 DELM = .336 REM = 645.0
PLATE = 1 UINF = .0140 DEL2 = .504
X(INI) = 2.00 GM = 5.472 THETA = .0421 DEL4 = 3.263
K(E06) = -1.460 GM = -4.403 BETA = .253 H = 1.712

Table with 13 columns: I, Y+, U+, T+, Y/DEL3, -TD, Y, U, T, TAU+, Q+. Rows 1-42 containing numerical data for DATE = 120271.

DATE = 120271 (-0.15, 0.004, -0.17)

T RUN = 120271-1 STNA = .00171 DELM = .619 REM = 949.0
V RUN = 112871-1 CF/2 = .00071 DELM = .655 REM = 1441.0
PLATE = 2 UINF = 26.7 DEL2 = .0611 DEL3 = 1.192
X(INI) = 10.00 GM = 5.949 THETA = 1.837 DEL4 = 10.499
K(E06) = -1.840 GM = -1.362 BETA = 2.931 H = 1.652

Table with 13 columns: I, Y+, U+, T+, Y/DEL3, -TD, Y, U, T, TAU+, Q+. Rows 1-42 containing numerical data for DATE = 120271.

DATE = 013072 (-0.15, -0.001)
T RUN = 13072-1 STNA = .00309 DELM = .704 REH = 772.0
V RUN = 121171-3 OFI2 = .00212 DELM = .758 REH = 1244.0
PLATE = 6 UINF = 2.5 DEL2 = .0608 DEL3 = 1.416
X(IN) = 22.00 GM = 4.167 THETA = .0977 DEL4 = 5.900
K(E06) = -.4610 GAM = -1.076 BETA = .422 H = 1.532

Table with 13 columns: I, Y+, U+, T+, Y/DEL3, -ID, Y, U, T, TAU+, Q+, and 14 rows of data points.

Table with 13 columns: I, Y+, U+, T+, Y/DEL3, -ID, Y, U, T, TAU+, Q+, and 14 rows of data points.

Table with 13 columns: I, Y+, U+, T+, Y/DEL3, -ID, Y, U, T, TAU+, Q+, and 14 rows of data points.

Table with 13 columns: I, Y+, U+, T+, Y/DEL3, -ID, Y, U, T, TAU+, Q+, and 14 rows of data points.

DATE = 013072 (-0.15, -0.001)
T RUN = 13072-1 STNA = .00276 DELM = 1.251 REH = 1283.0
V RUN = 121171-3 OFI2 = .00196 DELM = 1.244 REH = 1832.0
PLATE = 6 UINF = 2.5 DEL2 = .0608 DEL3 = 1.416

Table with 13 columns: I, Y+, U+, T+, Y/DEL3, -ID, Y, U, T, TAU+, Q+, and 14 rows of data points.

Table with 13 columns: I, Y+, U+, T+, Y/DEL3, -ID, Y, U, T, TAU+, Q+, and 14 rows of data points.

Table with 13 columns: I, Y+, U+, T+, Y/DEL3, -ID, Y, U, T, TAU+, Q+, and 14 rows of data points.

Table with 13 columns: I, Y+, U+, T+, Y/DEL3, -ID, Y, U, T, TAU+, Q+, and 14 rows of data points.

DATE = 013072 (-0.15, -0.001)
T RUN = 13072-1 STNA = .00269 DELM = 1.004 REH = 1091.0
V RUN = 121171-3 OFI2 = .00203 DELM = 1.093 REH = 1593.0
PLATE = 9 UINF = 2.3 DEL2 = .0676 DEL3 = 2.051
X(IN) = 34.00 GM = 4.097 THETA = .1251 DEL4 = 5.475
K(E06) = -.3260 GAM = -.905 BETA = .389 H = 1.513

Table with 13 columns: I, Y+, U+, T+, Y/DEL3, -ID, Y, U, T, TAU+, Q+, and 14 rows of data points.

Table with 13 columns: I, Y+, U+, T+, Y/DEL3, -ID, Y, U, T, TAU+, Q+, and 14 rows of data points.

Table with 13 columns: I, Y+, U+, T+, Y/DEL3, -ID, Y, U, T, TAU+, Q+, and 14 rows of data points.

Table with 13 columns: I, Y+, U+, T+, Y/DEL3, -ID, Y, U, T, TAU+, Q+, and 14 rows of data points.

DATE = 013072 (-0.15, -0.001)
T RUN = 13072-1 STNA = .00266 DELM = 1.531 REH = 1496.0
V RUN = 121171-3 OFI2 = .00191 DELM = 1.459 REH = 2080.0
PLATE = 15 UINF = 2.1 DEL2 = .1244 DEL3 = 3.199
X(IN) = 58.00 GM = 4.075 THETA = .1068 DEL4 = 13.028
K(E06) = -.2100 GAM = -.908 BETA = .357 H = 1.491

Table with 13 columns: I, Y+, U+, T+, Y/DEL3, -ID, Y, U, T, TAU+, Q+, and 14 rows of data points.

Table with 13 columns: I, Y+, U+, T+, Y/DEL3, -ID, Y, U, T, TAU+, Q+, and 14 rows of data points.

Table with 13 columns: I, Y+, U+, T+, Y/DEL3, -ID, Y, U, T, TAU+, Q+, and 14 rows of data points.

Table with 13 columns: I, Y+, U+, T+, Y/DEL3, -ID, Y, U, T, TAU+, Q+, and 14 rows of data points.

Table with columns: I, Y+, U+, T+, Y/OEL3, -IO, Y, U, T, TAU+, Q+. Includes parameters: DATE = 122171 (-0.15, -0.002), T RUN = 122171-1 STNA = .00403, DELM = .364, REM = 373.0, V RUN = 121671-3 CFZ2 = .00202, DELM = .494, REM = 721.0, PLATE = 3 UINF = 27.1, DEL2 = .0267, DEL3 = .597, X(IM) = 10.00, GM = 4.224, THETA = .0515, DEL4 = 2.477, K(E06) = -.8266, GAM = -1.134, BETA = .321, M = 1.525.

Table with columns: I, Y+, U+, T+, Y/OEL3, -IO, Y, U, T, TAU+, Q+. Includes parameters: DATE = 122171 (-0.15, -0.002), T RUN = 122171-1 STNA = .00359, DELM = .645, REM = 522.0, V RUN = 121671-3 CFZ2 = .00264, DELM = .677, REM = 1134.0, PLATE = 6 UINF = 24.5, DEL2 = .0492, DEL3 = 1.053, X(IM) = 22.00, GM = 3.938, THETA = .0417, DEL4 = 4.266, K(E06) = -.6570, GAM = -.945, BETA = .272, M = 1.900.

Table with columns: I, Y+, U+, T+, Y/OEL3, -IO, Y, U, T, TAU+, Q+. Includes parameters: DATE = 122171 (-0.15, -0.002), T RUN = 122171-1 STNA = .00338, DELM = .569, REM = 542.0, V RUN = 121671-3 CFZ2 = .00256, DELM = .596, REM = 1232.0, PLATE = 9 UINF = 22.0, DEL2 = .0710, DEL3 = 1.543, X(IM) = 34.00, GM = 3.867, THETA = 1.039, DEL4 = 5.908, K(E06) = -.3250, GAM = -.873, BETA = .238, M = 1.458.

Table with columns: I, Y+, U+, T+, Y/OEL3, -IO, Y, U, T, TAU+, Q+. Includes parameters: DATE = 122171 (-0.15, -0.002), T RUN = 122171-1 STNA = .00325, DELM = 1.079, REM = 1022.0, V RUN = 121671-3 CFZ2 = .00255, DELM = 1.070, REM = 1444.0, PLATE = 12 UINF = 21.2, DEL2 = .0492, DEL3 = 1.958, X(IM) = 46.00, GM = 3.790, THETA = 1.257, DEL4 = 4.422, K(E06) = -.2530, GAM = -.804, BETA = .222, M = 1.454.

DATE = 122171 (-0.15, -0.002)
T RUN = 122171-1 STNA = .00314 DELH = 1.279 REM = 1175.0
V RUN = 121671-3 CF/2 = .00246 DELM = 1.250 REM = 1590.0
PLATE = 15 UNF = 21.5 DEL2 = 1.056 DEL3 = 2.322
X(IN) = 50.00 GH = 3.801 THETA = 14.28 DEL4 = 9.927
K(E06) = -.2100 GAM = -.785 BETA = .207 H = 1.425

DATE = 122171 (-0.15, -0.002)
T RUN = 122171-1 STNA = .00308 DELH = 1.442 REM = 1330.0
V RUN = 121671-3 CF/2 = .00242 DELM = 1.450 REM = 1747.0
PLATE = 10 UNF = 21.0 DEL2 = 1.223 DEL3 = 2.676
X(IN) = 70.00 GH = 3.706 THETA = 14.66 DEL4 = 9.918
K(E06) = -.1820 GAM = -.767 BETA = .200 H = 1.415

Table with 10 columns: I, Y+, U+, T+, Y/DEL3, -ID, Y, U, T, TAU+, Q+. Rows 1-39.

Table with 10 columns: I, Y+, U+, T+, Y/DEL3, -ID, Y, U, T, TAU+, Q+. Rows 1-39.

DATE = 122171 (-0.15, -0.002)
T RUN = 122171-1 STNA = .00702 DELH = 1.699 REM = 1444.0
V RUN = 121671-3 CF/2 = .00240 DELM = 1.666 REM = 1933.0
PLATE = 21 UNF = 20.6 DEL2 = 1.126 DEL3 = 3.008
X(IN) = 82.00 GH = 3.698 THETA = 14.00 DEL4 = 11.327
K(E06) = -.1660 GAM = -.766 BETA = .199 H = 1.414

DATE = 122171 (-0.15, -0.002)
T RUN = 122171-1 STNA = .00298 DELH = 1.824 REM = 1554.0
V RUN = 121671-3 CF/2 = .00228 DELM = 1.736 REM = 2002.0
PLATE = 23 UNF = 20.2 DEL2 = 1.448 DEL3 = 3.285
X(IN) = 90.00 GH = 3.686 THETA = 14.917 DEL4 = 12.105
K(E06) = -.1660 GAM = -.766 BETA = .212 H = 1.398

Table with 10 columns: I, Y+, U+, T+, Y/DEL3, -ID, Y, U, T, TAU+, Q+. Rows 1-39.

Table with 10 columns: I, Y+, U+, T+, Y/DEL3, -ID, Y, U, T, TAU+, Q+. Rows 1-39.

DATE = 122371 (-0.15, -0.00)
T RUN = 122371-1 STNA = .00441 DELW = .592 REW = 521.0
V RUN = 122371-2 CF/2 = .00379 DELM = .761 REM = 757.0
PLATE = 12 UINF = 22.0 DEL2 = .0493 DEL3 = .804
X(IN) = 46.00 GM = 3.649 THETA = .0659 DEL4 = 3.225
K(E06) = -2630 GAM = -.525 BETA = .076 H = 1.379

DATE = 122371 (-0.15, -0.00)
T RUN = 122371-1 STNA = .00432 DELW = .805 REW = 570.0
V RUN = 122371-2 CF/2 = .00377 DELM = .832 REM = 768.0
PLATE = 15 UINF = 21.4 DEL2 = .0511 DEL3 = .995
X(IN) = 58.00 GM = 3.608 THETA = .0688 DEL4 = 3.599
K(E06) = -2180 GAM = -.446 BETA = .085 H = 1.376

Table with columns I, Y+, U+, T+, Y/DEL3, -10, Y, U, T, TAU+, Q+. Contains numerical data for rows 1 through 40.

Table with columns I, Y+, U+, T+, Y/DEL3, -10, Y, U, T, TAU+, Q+. Contains numerical data for rows 1 through 40.

DATE = 122371 (-0.15, -0.00)
T RUN = 122371-1 STNA = .00426 DELW = .657 REW = 522.0
V RUN = 122371-2 CF/2 = .00379 DELM = .761 REM = 757.0
PLATE = 18 UINF = 20.8 DEL2 = .0572 DEL3 = 1.096
X(IN) = 70.00 GM = 3.542 THETA = .0726 DEL4 = 3.992
K(E06) = -1070 GAM = -.422 BETA = .057 H = 1.350

DATE = 122371 (-0.15, -0.00)
T RUN = 122371-1 STNA = .00426 DELW = .969 REW = 645.0
V RUN = 122371-2 CF/2 = .00377 DELM = .987 REM = 812.0
PLATE = 21 UINF = 20.4 DEL2 = .0616 DEL3 = 1.177
X(IN) = 82.00 GM = 3.516 THETA = .0763 DEL4 = 4.139
K(E06) = -1640 GAM = -.373 BETA = .052 H = 1.357

Table with columns I, Y+, U+, T+, Y/DEL3, -10, Y, U, T, TAU+, Q+. Contains numerical data for rows 1 through 40.

Table with columns I, Y+, U+, T+, Y/DEL3, -10, Y, U, T, TAU+, Q+. Contains numerical data for rows 1 through 40.

DATE = 011072 (-0.15, -0.001, -0.17)

T RUN = 11072-1 STNA = .00279 DELH = 1.044 REM = 1107.0
V RUN = 10372-1 CF/2 = .00191 DELM = 1.011 REM = 1029.0
PLATE = 9 UINF = 23.0 DEL2 = .0917 DEL3 = 2.166
X(IN) = 34.00 GH = 4.167 THETA = 1.346 DEL4 = 9.010
K(E06) = -.3250 GAM = -1.007 BETA = .429 H = 1.524

T RUN = 11072-1 STNA = .00264 DELH = 1.303 REM = 1359.0
V RUN = 10372-1 CF/2 = .00182 DELM = 1.280 REM = 1971.0
PLATE = 12 UINF = 22.0 DEL2 = .1174 DEL3 = 2.827
X(IN) = 46.00 GH = 4.193 THETA = 1.703 DEL4 = 11.893
K(E06) = -.2560 GAM = -.966 BETA = .430 H = 1.522

Table with 11 columns: I, Y+, U+, T+, Y/DEL3, -IO, Y, U, T, TAU+, Q+. Rows 1-40.

Table with 12 columns: I, Y+, U+, T+, Y/DEL3, -IO, Y, U, T, TAU+, Q+. Rows 1-40.

DATE = 011072 (-0.15, -0.001, -0.17)

T RUN = 11072-1 STNA = .00253 DELH = 1.551 REM = 1546.0
V RUN = 10372-1 CF/2 = .00176 DELM = 1.524 REM = 2256.0
PLATE = 15 UINF = 21.4 DEL2 = .1411 DEL3 = 3.437
X(IN) = 56.00 GH = 4.178 THETA = 2.007 DEL4 = 14.877
K(E06) = -.2120 GAM = -.951 BETA = .421 H = 1.503

T RUN = 11072-1 STNA = .00245 DELH = 1.935 REM = 1934.0
V RUN = 10372-1 CF/2 = .00171 DELM = 1.784 REM = 2540.0
PLATE = 18 UINF = 20.9 DEL2 = .1674 DEL3 = 4.129
X(IN) = 70.00 GH = 4.182 THETA = 2.219 DEL4 = 17.186
K(E06) = -.1800 GAM = -.916 BETA = .415 H = 1.498

Table with 11 columns: I, Y+, U+, T+, Y/DEL3, -IO, Y, U, T, TAU+, Q+. Rows 1-40.

Table with 12 columns: I, Y+, U+, T+, Y/DEL3, -IO, Y, U, T, TAU+, Q+. Rows 1-40.

DATE = 011772 (-0.15, -0.002, -0.17)

T RUN = 11772-1 STNA = .00338 DELH = .697 REM = 574.0
V RUN = 122971-1 CF/2 = .00244 DELM = .683 REM = 1473.0
PLATE = 6 UINF = 24.4 DEL2 = .0930 DEL3 = 1.189
X(TIN) = 22.00 GM = 4.960 THETA = .0844 DEL4 = 4.831
K(EO6) = -4.600 GAM = -.982 BETA = .389 H = 1.902

Table with columns I, Y+, U+, T+, V/OEL3, -TO, Y, U, T, TAU+, Q+, and 11 data rows.

DATE = 011772 (-0.15, -0.002, -0.17)

T RUN = 11772-1 STNA = .00315 DELH = .889 REM = 901.0
V RUN = 122971-1 CF/2 = .00231 DELM = .884 REM = 1330.0
PLATE = 9 UINF = 23.0 DEL2 = .0791 DEL3 = 1.689
X(TIN) = 34.00 GM = 4.006 THETA = .1109 DEL4 = 6.767
K(EO6) = -3.280 GAM = -.912 BETA = .288 H = 1.679

Table with columns I, Y+, U+, T+, V/OEL3, -TO, Y, U, T, TAU+, Q+, and 11 data rows.

DATE = 011772 (-0.15, -0.002, -0.17)

T RUN = 11772-1 STNA = .00300 DELH = 1.176 REM = 1108.0
V RUN = 122971-1 CF/2 = .00221 DELM = 1.120 REM = 1575.0
PLATE = 12 UINF = 22.1 DEL2 = .0961 DEL3 = 2.143
X(TIN) = 46.00 GM = 3.956 THETA = .1366 DEL4 = 9.637
K(EO6) = -2.570 GAM = -.852 BETA = .280 H = 1.479

Table with columns I, Y+, U+, T+, V/OEL3, -TO, Y, U, T, TAU+, Q+, and 11 data rows.

DATE = 011772 (-0.15, -0.002, -0.17)

T RUN = 11772-1 STNA = .00289 DELH = 1.352 REM = 1294.0
V RUN = 122971-1 CF/2 = .00215 DELM = 1.330 REM = 1776.0
PLATE = 15 UINF = 21.0 DEL2 = .1161 DEL3 = 2.676
X(TIN) = 65.00 GM = 3.916 THETA = .1564 DEL4 = 10.124
K(EO6) = -2.210 GAM = -.832 BETA = .264 H = 1.450

Table with columns I, Y+, U+, T+, V/OEL3, -TO, Y, U, T, TAU+, Q+, and 11 data rows.

DATE = 011772 (-0.15, -0.002, -0.17)

T RUN = 11772-1 STNA = .00281 DELM = 1.683 REM = 1689.0
V RUN = 122971-1 CF/2 = .00205 DELM = 1.520 REM = 1996.0
PLATE = 18 UNIF = 20.9 DEL2 = 1.165 DEL3 = 3.117
X(1M) = 70.00 GH = 3.883 THETA = .1835 DEL4 = 12.108
K(E06) = -.1790 GAM = -.797 BETA = .282 H = 1.449

Table with columns I, Y+, U+, T+, V/DEL3, -TO, Y, U, T, TAU+, Q+, and 11 rows of data.

DATE = 011772 (-0.15, -0.002, -0.17)

T RUN = 11772-1 STNA = .00274 DELM = 1.759 REM = 1631.0
V RUN = 122971-1 CF/2 = .00205 DELM = 1.520 REM = 1996.0
PLATE = 21 UNIF = 20.4 DEL2 = 1.532 DEL3 = 3.521
X(1M) = 92.00 GH = 3.562 THETA = .2066 DEL4 = 13.598
K(E06) = -.1598 GAM = -.771 BETA = .296 H = 1.442

Table with columns I, Y+, U+, T+, V/DEL3, -TO, Y, U, T, TAU+, Q+, and 20 rows of data.

DATE = 011772 (-0.15, -0.002, -0.17)

T RUN = 11772-1 STNA = .00270 DELM = 1.921 REM = 1793.0
V RUN = 122971-1 CF/2 = .00201 DELM = 1.949 REM = 2294.0
PLATE = 23 UNIF = 20.1 DEL2 = .1762 DEL3 = 3.904
X(1M) = 90.00 GH = 3.926 THETA = .2166 DEL4 = 15.248
K(E06) = -.1490 GAM = -.786 BETA = .260 H = 1.436

Table with columns I, Y+, U+, T+, V/DEL3, -TO, Y, U, T, TAU+, Q+, and 20 rows of data.

DATE = 012472 (-0.15, -0.004, -0.17)

T RUN = 12472-1 STNA = .01690 DELM = .154 REM = 127.0
V RUN = 122771-3 CF/2 = .00369 DELM = .225 REM = 471.0
PLATE = 1 UNIF = 29.3 DEL2 = .0052 DEL3 = .149
X(1M) = 2.00 GH = 3.441 THETA = .0166 DEL4 = .509
K(E06) = -.4450 GAM = -.435 BETA = .299 H = 1.422

Table with columns I, Y+, U+, T+, V/DEL3, -TO, Y, U, T, TAU+, Q+, and 20 rows of data.

DATE = 012472 (-0.15, -0.004, -0.17)

T RUN = 12472-1 STNA = .00472 DELM = .308 REM = 282.0
V RUN = 122771-3 CF/2 = .00369 DELM = .308 REM = 564.0
PLATE = 3 UINF = 26.8 DEL2 = .020 DEL3 = 4.26
X(IN) = 10.00 GM = 4.301 THETA = .0403 DEL4 = 1.831
K(E06) = -.93E0 GAN = -1.004 BETA = .191 H = 1.473

T RUN = 12472-1 STNA = .00423 DELM = .486 REM = 423.0
V RUN = 122771-3 CF/2 = .00340 DELM = .463 REM = 720.0
PLATE = 3 UINF = 24.3 DEL2 = .0331 DEL3 = .694
X(IN) = 22.00 GM = 4.020 THETA = .0564 DEL4 = 2.789
K(E06) = -.4650 GAN = -.763 BETA = .146 H = 1.479

Table with columns I, Y+, U+, T+, V/DEL3, -TO, Y, U, T, TAU+, Q+, I, Y+, U+, T+, V/DEL3, -TO, Y, U, T, TAU+, Q+. Rows 1-40 showing data for two different runs.

DATE = 012472 (-0.15, -0.004, -0.17)

T RUN = 12472-1 STNA = .00394 DELM = .674 REM = 553.0
V RUN = 122771-3 CF/2 = .00322 DELM = .720 REM = 942.0
PLATE = 3 UINF = 23.4 DEL2 = .0449 DEL3 = .959
X(IN) = 34.00 GM = 4.024 THETA = .0659 DEL4 = 3.858
K(E06) = -.3310 GAN = -.679 BETA = .121 H = 1.411

DATE = 012472 (-0.15, -0.004, -0.17)

T RUN = 12472-1 STNA = .00375 DELM = .811 REM = 563.0
V RUN = 122771-3 CF/2 = .00310 DELM = .801 REM = 983.0
PLATE = 3 UINF = 22.0 DEL2 = .0593 DEL3 = 1.251
X(IN) = 45.00 GM = 3.818 THETA = .0841 DEL4 = 4.798
K(E06) = -.2570 GAN = -.896 BETA = .119 H = 1.424

Table with columns I, Y+, U+, T+, V/DEL3, -TO, Y, U, T, TAU+, Q+, I, Y+, U+, T+, V/DEL3, -TO, Y, U, T, TAU+, Q+. Rows 1-40 showing data for two different runs.

References

1. Simpson, R. L., Kays, W. M., and Moffat, R. J., "The Turbulent Boundary Layer on a Porous Plate: An Experimental Study of the Fluid Dynamics with Injection and Suction," Report No. HMT-2, Thermosciences Division, Dept. of Mech. Engrg., Stanford Univ., (1967).
2. Moffat, R. J., and Kays, W. M., "The Turbulent Boundary Layer on a Porous Plate: Experimental Heat Transfer with Uniform Blowing and Suction," Report No. HMT-1, Thermosciences Division, Dept. of Mech. Engrg., Stanford Univ., (1967).
3. Whitten, D. G., Kays, W. M., and Moffat, R. J., "The Turbulent Boundary Layer on a Porous Plate: Experimental Heat Transfer with Variable Suction, Blowing, and Surface Temperature," Report No. HMT-3, Thermosciences Division, Dept. of Mech. Engrg., Stanford Univ., (1967).
4. Julien, H. L., Kays, W. M., and Moffat, R. J., "The Turbulent Boundary Layer on a Porous Plate: Experimental Study of the Effects of a Favorable Pressure Gradient," Report No. HMT-4, Thermosciences Division, Dept. of Mech. Engrg., Stanford Univ., (1969).
5. Loyd, R. J., Moffat, R. J., and Kays, W. M., "The Turbulent Boundary Layer on a Porous Plate: An Experimental Study of the Fluid Dynamics with Strong Favorable Pressure Gradients and Blowing," Report No. HMT-13, Thermosciences Division, Dept. of Mech. Engrg., Stanford Univ., (1970).
6. Thielbahr, W. H., Kays, W. M., and Moffat, R. J., "The Turbulent Boundary Layer: Experimental Heat Transfer with Blowing, Suction, and Favorable Pressure Gradient," Report No. HMT-5, Thermosciences Division, Dept. of Mech. Engrg., Stanford Univ., (1969).
7. Kearney, D. W., Moffat, R. J., and Kays, W. M., "The Turbulent Boundary Layer: Experimental Heat Transfer with Strong Favorable Pressure Gradients and Blowing," Report No. HMT-12, Thermosciences Division, Dept. of Mech. Engrg., Stanford Univ., (1970).
8. Kays, W. M., "Heat Transfer to the Transpired Turbulent Boundary Layer," Report No. HMT-14, Thermosciences Division, Dept. of Mech. Engrg., Stanford Univ., (1971).
9. Andersen, P. S., Kays, W. M., and Moffat, R. J., "The Turbulent Boundary Layer on a Porous Plate: An Experimental Study of the Fluid Mechanics for Adverse Free-Stream Pressure Gradients," Report No. HMT-15, Thermosciences Division, Dept. of Mech. Engrg., Stanford Univ., (1972).
10. McLean, J. D., "The Transpired Turbulent Boundary Layer in an Adverse Pressure Gradient," Ph.D. Thesis, Department of Aerospace and Mechanical Sciences, Princeton Univ., (1970).

11. Stevenson, T. N., "A Law of the Wall for Turbulent Boundary Layers with Suction or Injection," The College of Aeronautics, Cranfield, Aero Report No. 166, (1963).
12. Perry, A. E., Bell, J. B., and Joubert, P. N., "Velocity and Temperature Profiles in Adverse Pressure Gradient Turbulent Boundary Layers," *J. Fluid Mechanics*, 25(2), 299 (1966).
13. Hatton, A. P., and Eustace, V. A., "Heat Transfer Measurements Through the Incompressible Turbulent Boundary Layer with Accelerating and Decelerating Flows," *Proceedings, 1966 International Heat Transfer Conference*, V2, p. 34-40.
14. Clauser, F. H., "Turbulent Boundary Layers in Adverse Pressure Gradients," *J. of Aero Sci.*, 21, 91, (1954).
15. Bradshaw, P., "The Turbulence Structure of Equilibrium Boundary Layers," *J. Fluid Mech.*, Vol. 29, Part 4, pp. 625-645, (1967).
16. Kays, W. M., Convective Heat and Mass Transfer, McGraw-Hill, New York, (1966).
17. Keenan, J. H., Keyes, F. G., Hill, P. G., and Moore, J. G., Steam Tables, John Wiley, New York, (1969).
18. Schlichting, H., Boundary Layer Theory, McGraw-Hill, New York, (1966).
19. Moffat, R. J., and Kays, W. M., "The Turbulent Boundary Layer on a Porous Plate: Experimental Heat Transfer with Uniform Blowing and Suction," *Int. J. Heat Mass Transfer*, 1968, 11 (10), 1547-1566.
20. Reynolds, W. C., Kays, W. M., and Kline, S. J., "Heat Transfer in the Turbulent Incompressible Boundary Layer," *NASA Memos* 12-1, 2, 3, and 4-58W, (1958).
21. Jenkins, R., "Variation of the Eddy Conductivity with Prandtl Modulus and Its Use in Prediction of Turbulent Heat Transfer Coefficients," *Heat Transfer and Fluid Mechanics Institute*, Stanford Univ. Press, Stanford, Calif., p. 147, 1952.
22. Deissler, R. G., "Analysis of Fully Developed Turbulent Heat Transfer at Low Peclet Numbers in Smooth Tubes with Application to Liquid Metals," *NACA RM ES2F05*, Aug. 11, 1952.
23. Lykoudis, P. S., and Touloukian, Y. S., "Heat Transfer in Liquid Metals," *ASME Paper No. 57-HT-16*.
24. Tokuro, M., and Tadahisa, S., "The Ratio of the Eddy Diffusivities for Heat and Momentum and Its Effect on Liquid Metal Heat Transfer Coefficients," *Proceedings, 1961 International Heat Transfer Conference*, Paper No. 78.

25. Rotta, J. C., "Temperaturverteilungen in der Turbulenten Grenzschicht an der Ebenen Platte," *Int. J. Heat Mass Transfer*, 7, 215-228, (1964).
26. Simpson, R. L., Whitten, D. G., and Moffat, R. J., "An Experimental Study of the Turbulent Prandtl Number of Air with Injection and Suction," *Int. J. Heat Mass Transfer*, 13, 125-143, (1970).
27. Seban, R. A., and Doughty, D. L., "Heat Transfer to Turbulent Boundary Layers with Variable Free-Stream Velocity," *Trans. ASME*, 78, 217, (1956).
28. Moretti, P. M., and Kays, W. M., "Heat Transfer Through an Incompressible Turbulent Boundary Layer with Varying Free-Stream Velocity and Varying Surface Temperature," Stanford University, Mech. Engrg. Dept. Rep. No. PG-1, (1964).
29. Spalding, D. B., and Patankar, S. V., Heat and Mass Transfer in Boundary Layers, Morgan-Grampian, London, (1967).
30. Meier, H. U., and Rotta, J. C., "Experimental and Theoretical Investigations of Temperature Distributions in Supersonic Boundary Layers," AIAA Paper No. 70-744, 1970.
31. Blom, J., "An Experimental Determination of the Turbulent Prandtl Number in a Developing Temperature Boundary Layer," Ph.D. Thesis, Technische Hogeschool, Eindhoven, The Netherlands, 1970 (in English).
32. Johnson, D. S., "Velocity and Temperature Fluctuation Measurements in a Turbulent Boundary Layer Downstream of a Stepwise Discontinuity in Wall Temperature," *J. Appl. Mech.*, Vol. 26, 325-336, (1959).
33. Kline, S. J., and McClintock, F. A., "Describing Uncertainties in Single Sample Experiments," *Mechanical Engineering*, p. 3., January, 1953.

APPENDIX A

ANALYSIS OF TEMPERATURE DISTRIBUTION IN BOUNDARY LAYER TEMPERATURE PROBE

When any temperature sensing instrument is immersed in a fluid, the indicated temperature will differ from the true undisturbed fluid temperature. If one assumes that the temperature sensing instrument does not appreciably alter the temperature field at the location of the sensor, then the most common causes of error are radiation, velocity, and conduction losses. This analysis is aimed at estimating the conduction losses.

A thermocouple probe was used in this study and will be idealized as two butt welded cylinders in cross flow, as shown in Figure A-1. Each end of the probe is assumed to be maintained at temperature T_0 , and the local gas temperature is named T_∞ . Since the thermal properties of the two thermoelectric materials are different, the analysis will be divided into two regions. The applicable differential equation and boundary conditions for the two regions are as follows:

Region 1	Region 2	
$\frac{d^2\theta_1}{dx^2} - m_1^2\theta_1 = 0$	$\frac{d^2\theta_2}{dx^2} - m_2^2\theta_2 = 0$	
$\theta_1(-L/2) = \theta_0$	$\theta_2(L/2) = \theta_0$	(A-1)
$\theta_1(0) = \theta_2(0)$	$k_1 \left. \frac{d\theta_1}{dx} \right _{x=0} = k_2 \left. \frac{d\theta_2}{dx} \right _{x=0}$	

where $\theta = T - T_\infty$ and the fin parameters are given by

$$m_{1,2} = 2 \sqrt{Nu_D k_f / k_{1,2} / D} \quad (A-2)$$

The solution to (A-1) is

$$\frac{\theta_1(x)}{\theta_0} = A_3 \cosh(m_1 x) + \beta A_4 \sinh(m_1 x) \quad (A-3)$$

$$\frac{\theta_2(x)}{\theta_0} = A_3 \cosh(m_2 x) + A_4 \sinh(m_2 x)$$

where

$$A_3 = \frac{\beta \sinh(p_1) + \sinh(p_2)}{\beta \cosh(p_2) \sinh(p_1) + \cosh(p_1) \sinh(p_2)} \quad (A-4)$$

$$A_4 = \frac{\cosh(p_1) - \cosh(p_2)}{\beta \cosh(p_2) \sinh(p_1) + \cosh(p_1) \sinh(p_2)}$$

$$p_{1,2} = m_{1,2} L/2, \quad \beta = \sqrt{k_2/k_1}$$

In order to compute the temperature distribution in the probe, the Nusselt number based on the wire diameter must be known. From Kreith [A-1], the Nusselt number for a cylinder in cross flow in air can be correlated by

$$Nu_D = C(Re_D)^n \quad (A-5)$$

The thermal conductivity of the two thermoelectric elements must also be known. Two of the more common thermocouple pairs are Chromel/constantan and iron/constantan. From Benedict [A-2], the following thermal conductivity data was obtained:

iron	:	0.0096	Btu/ft-sec- ⁰ F
constantan:		0.0038	"
Chromel	:	0.0031	"

Using the above data, the non-dimensional temperature distribution was computed for $D = 0.003$ inches, $L = 0.5$ inches, and an assumed velocity of 2 ft/sec. This velocity represents a lower bound on the velocity encountered in any of the experiments; hence, it represents the most severe test of the probe design. The computed results for the two different thermocouple types are shown in Figure (A-2). Since the thermal conductivities of the Chromel/constantan pair are more nearly equal than the iron/constantan pair, the Chromel/constantan probe has a more symmetrical temperature distribution. Also, the Chromel/constantan probe has a much smaller difference between the probe center temperature and the local gas temperature. Consequently, the Chromel/constantan probe was judged superior to the iron/constantan probe.

In order to estimate the actual temperature error, one must know both T_0 and T_∞ . Since we do not know either of these two temperatures, let us assume that $T_0 - T_\infty = 10^\circ\text{F}$. From the data in Figure (A-2), the resulting thermocouple error would be $\Delta T = (10)(0.005) = 0.05^\circ\text{F}$. This error is within the accuracy of the digital voltmeter used to measure the thermocouple output voltage. Hence, the Chromel/constantan probe should have negligible conduction errors at all conditions.

REFERENCES

- A-1. Kreith, F., Principles of Heat Transfer, International Textbook, Scranton (1958).
- A-2. Benedict, R. P., "Fundamentals of Temperature, Pressure, and Flow Measurements," Wiley, New York (1969).

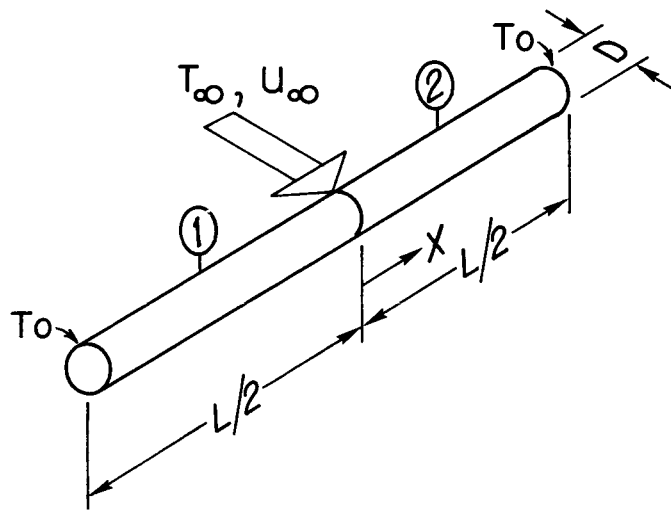


Figure A-1 Schematic of temperature probe

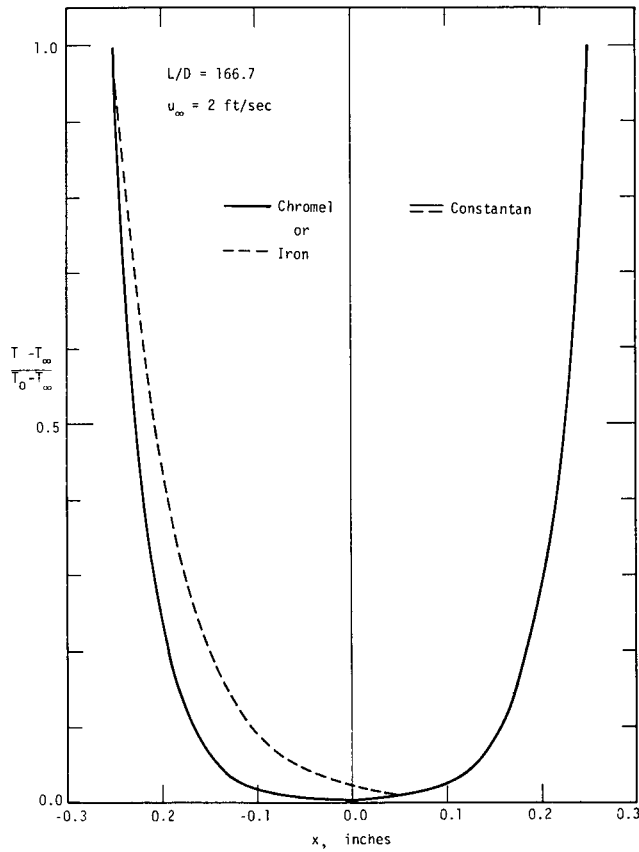


Figure A-2 Comparison of temperature distribution in Chromel/constantan probe with iron/constantan probe